

Deciphering the chromatin binding mechanisms of human HP1 variants at the single-molecule level

THÈSE N° 8757 (2018)

PRÉSENTÉE LE 28 SEPTEMBRE 2018

À LA FACULTÉ DES SCIENCES DE BASE

LABORATOIRE DE CHIMIE BIOPHYSIQUE DES MACROMOLÉCULES

PROGRAMME DOCTORAL EN CHIMIE ET GÉNIE CHIMIQUE

ÉCOLE POLYTECHNIQUE FÉDÉRALE DE LAUSANNE

POUR L'OBTENTION DU GRADE DE DOCTEUR ÈS SCIENCES

PAR

Louise Catherine BRYAN

acceptée sur proposition du jury:

Dr A.-S. Chauvin, présidente du jury

Prof. B. Fierz, directeur de thèse

Dr N. Vastenhouw, rapporteuse

Prof. B. Schuler, rapporteur

Prof. D. Suter, rapporteur



ÉCOLE POLYTECHNIQUE
FÉDÉRALE DE LAUSANNE

Suisse
2018

Abstract

In eukaryotic cells, DNA is tightly packed in the form of chromatin. The basic structure of chromatin is a nucleosome composed of 147 bp DNA wrapped around eight histone proteins; two copies of H2A, H2B, H3 and H4. These histone proteins are decorated with patterns of post-translational modifications leading to either a direct change in chromatin structure or to the recruitment of effector proteins.

Heterochromatin protein 1 (HP1) is an effector protein, that binds with low micromolar affinity to trimethylated lysine 9 on histone H3 (H3K9me3). It has been shown that HP1 localizes to specific domains where its binding is highly dynamic, however it is not well understood how HP1 is efficiently recruited to heterochromatin sites enacting stable gene silencing. The aim of this project was therefore to develop a single molecule method in total internal fluorescence microscopy (TIRFM) to study the dynamic binding of HP1 towards chemically synthesized chromatin fibers. This would enable us to understand how HP1, which has low affinity towards H3K9me3, is able to increase its affinity and localization to chromatin. Initially, three models were studied; 1) The co-existence of many low-affinity binding sites in chromatin fibers allows rapid re-binding of HP1 α after dissociation. 2) Stable and long-lived complexes are the result of HP1 α oligomerization on the chromatin fiber. 3) Multivalent binding interactions of dimeric HP1 α increases binding affinity towards chromatin. We found that HP1 α residence time on chromatin depends on the density of H3K9me3, where the dissociated protein can rapidly rebind to a neighbouring site. Multivalency by HP1 α dimerization leads to longer retention and accelerates the association rate and HP1 α does not form oligomers but competes for free H3K9me3 sites.

Following on from these results we aimed to improve our understanding of how HP1 dynamically samples the chromatin landscape, by studying the influence of chromatin states over HP1 α binding, as well as finding out the binding differences between the HP1 isoforms (HP1 α , β and γ) and the influence of a phosphorylation mark on HP1 α . We found that HP1 α exhibits the longest residence times and fastest binding rates owing to DNA interaction as well as H3K9me3 binding, confirmed by *in vivo* fluorescence recovery after photobleaching (FRAP) experiments. Interestingly, phosphorylated HP1 α increases retention through strengthening of multivalency while reducing DNA binding. From the smTIRF results, a kinetic model was

developed to dissect the detailed mechanism of HP1-chromatin binding, revealing a multivalent interaction network provided by multiple weak protein and DNA interactions.

The final part of this thesis was focused towards improving our single molecule TIRF set up by developing a multiplexed read-out of nucleosomes. This will provide a way to measure the interaction of a chromatin binding protein towards a library of nucleosomes in one single molecule experiment. The technique relies on the nucleosomal DNA containing a short ssDNA site where the complementary labeled DNA piece can hybridize dynamically.

The work presented in this thesis, was based on using a single molecule microscopy technique to shed light on the recruitment of an effector protein to chromatin and on the development of a new technique to further investigate more complicated chromatin-binding proteins.

Keywords : chromatin, post-translational modifications, heterochromatin protein 1, multivalent chromatin effectors, single molecule microscopy

Résumé

Dans les cellules eukaryotiques, l'ADN est compacté sous forme de chromatine dont la structure de base est le nucléosome. Les nucléosomes sont composés de 147 pb d'ADN enroulés autour de huit histones ; deux copies de H2A, H2B, H3 et H4. Les histones sont décorées par des motifs de modifications post-traductionnelles (PTM) donnant lieu soit à des changements structuraux de la chromatine soit au recrutement de protéines effectrices.

L'hétérochromatine protéine 1 (HP1) est une protéine effectrice qui se lie avec une faible affinité de l'ordre du micromolaire aux histones H3 triméthylée au niveau de la lysine 9 (H3K9me3). Il a été démontré que l'HP1 est localisée dans des régions stables tout en restant très dynamique. Cependant, il n'est pas encore bien compris comment l'HP1 est recrutée de manière efficace à ces sites d'hétérochromatine. Le but de ce projet était donc de développer une méthode de microscopie à molécule unique pour étudier la liaison dynamique de l'HP1 vers des fibres de chromatine synthétisées chimiquement et de comprendre comment l'HP1, ayant une faible affinité pour H3K9me3, est capable d'augmenter son affinité et sa localisation sur la chromatine. Initialement, trois modèles ont été étudiés ; 1) La coexistence de nombreux sites de liaison permet une reliaison rapide de l'HP1 α après dissociation. 2) Les complexes stables avec des temps longs de rétention sont le résultat d'une oligomérisation de l'HP1 α . 3) Les interactions multivalentes de l'HP1 α dimérique augmentent l'affinité pour la chromatine. Nous avons trouvé que le temps de résidence de l'HP1 α sur la chromatine dépend de la densité de H3K9me3, ainsi la protéine dissociée peut rapidement se relier avec un site voisin. La multivalence par dimérisation de l'HP1 α conduit à une plus longue rétention et accélère son association. Une compétition pour les sites H3K9me3 libres a été observée démontrant que l'HP1 ne forme pas d'oligomère.

Nous avons ensuite voulu améliorer notre compréhension du mécanisme de recrutement de l'HP1. Nous avons donc étudié l'influence de la structure de la chromatine sur l'interaction de l'HP1 α , les différents modes de liaison des isoformes de cette protéine et d'une PTM sur l'HP1 α . Nous avons constaté que l'HP1 α présente les temps de résidence les plus longs et les constantes d'association les plus rapides en raison de son interaction avec l'ADN complémentaire à celle avec H3K9me3. L'HP1 α phosphorylée augmente sa rétention en renforçant la multivalence tout en réduisant la liaison avec l'ADN. A partir de ces résultats, un modèle cinétique a été développé pour disséquer le mécanisme des interactions HP1-

chromatine, révélant un réseau d'interaction multivalent créé par l'interaction avec les protéines et l'ADN.

La dernière partie de cette thèse était axée sur l'amélioration de notre système à molécule unique en développant une lecture multiplexée des nucléosomes. Cela fournira un moyen de mesurer l'interaction d'une protéine vers une librairie de nucléosomes. La technique repose sur un court morceau d'ADN à simple brin ajouté à l'ADN du nucléosome où son morceau complémentaire peut s'hybrider de manière dynamique.

Le travail présenté dans cette thèse est basé sur une technique de microscopie à molécule unique afin de déterminer les mécanismes de recrutement d'une protéine effectrice par la chromatine. Par la suite, cette technique a été améliorée dans le but d'étudier des protéines plus complexes.

Mots-clés : chromatine, modification post-traductionnelles, hétérochromatine protéine 1, effecteurs multivalents, microscopie à molécule unique

Acknowledgements

First of all, I would like to thank to my thesis supervisor, Prof. Beat Fierz for giving me the opportunity to carry out my PhD in his lab. This has been a great opportunity for me to learn so many techniques and to work on challenging projects. His door was always open for discussion and his motivation and enthusiasm for science is inspirational.

I wish to thank the jury committee; Dr. MER. Anne-Sophie Chauvin, Prof. David Suter, Dr. Nadine Vastenhouw and Prof. Benjamin Schuler for taking the time to review this thesis and attend my private defence.

I would like to thank all the lab members of LCBM:

I thank Carolin Lechner for all her support, help and friendship, to Sinan Kilic who taught me many things when I started in the lab and my bench neighbour, Andreas Bachmann who I worked with closely on the HP1 project. I also wish to thank former and current lab members for always being available whenever I needed help and for making LCBM a nice environment to work in; Aurore Delachat, Ninad Agash, Maeva Tobler, Maxime Miverlaz, Nora Guidotti, Iuliia Boichenko, Anne-Marinette Cao, Karthik Maddi, Harsh Nagpal, Ruud Hovius, Eduard Ebberink and Jade Chevalley

I also wish to thank all my collaborators who have helped me throughout this thesis; Horst Pick for his help with cell culture, Arne Seitz and Thierry Laroche for taking the time to teach me confocal microscopy, Daniel Weilandt for the computational modelling, Pascal Odermatt for AFM imaging of chromatin fibers, and Sandrine Georgeon for HP1 phosphorylation assays.

I also thank Marie Munoz for her kind attentions and help at all times. I am also grateful to Marie Jirousek, Jacques Gremaud, Yoann Dind.

Last but not least, I wish to thank my family; my parents for their constant support, my sister for her positive attitude and to my husband who has stood by my side at all times.

Table of Content

Abstract	I
Résumé	III
Acknowledgements	V
List of Figures	IX
List of Tables.....	XII
Abbreviations	XIII
1. Introduction	1
1.1. Chromatin structure.....	1
1.1.1. The nucleosome core structure	1
1.1.2. Hierarchical chromatin organization.....	2
1.2. Post translational modifications	4
1.2.1. Histone modifications	5
1.2.2. Cis-effect of histone PTMs	6
1.2.3. Trans-effect of histone PTMs	6
1.3. Heterochromatin and Euchromatin	8
1.3.1. Heterochromatin Protein 1	9
1.4. Protein engineering.....	10
1.4.1. Cysteine chemistry.....	11
1.4.2. Enzymatic reactions	13
1.4.3. Native chemical ligation	14
1.4.4. Expressed protein ligation.....	16
1.4.5. Amber suppression.....	19
1.5. Fluorescence Microscopy	19
1.5.1. Principles of fluorescence	20
1.5.2. Fluorescent molecules.....	23
1.5.3. Wide-field microscopy.....	23
1.5.4. Single molecule total internal reflection fluorescence microscopy	25
2. Aims of the thesis	27
3. HP1-chromatin binding at the single molecule level	29
3.1. Background and overview.....	29
3.2. Results & Discussion.....	31
3.2.1. Preparation of HP1 and chromatin.....	31

Table of content

3.2.2. Single molecule microscopy	35
3.2.3. HP1 α binding to 12x 177a H3K9me3 chromatin	39
3.3. Conclusion.....	42
4. Investigating the influence of chromatin structure and HP1 subtypes on HP1 recruitment	45
4.1. Background and overview.....	45
4.2. Results & Discussion.....	46
4.2.1. The influence of chromatin structure on HP1 binding.....	46
4.2.2. Dynamic interactions of HP1 isoforms to H3K9me3 chromatin.....	56
4.2.3. Dynamic interactions of phosphorylated HP1 α to H3K9me3 chromatin	61
4.2.4. <i>In vivo</i> dynamic binding of HP1	65
4.2.5. Kinetic modelling of HP1-chromatin interaction network	66
4.3. Conclusion.....	69
5. Single molecule multiplexed detection of nucleosomes	73
5.1. Background and overview.....	73
5.1.1. General experiment.....	75
5.2. Results and discussion.....	76
5.2.1. Development of the decoding system	76
5.2.2. Multilayer multiplexing	78
5.3. Conclusion and Outlook.....	83
6. Materials and methods.....	89
6.1. Chemicals	89
6.2. Instrumentation.....	90
6.3. Chromatin reconstitution.....	91
6.4. Effector protein preparation	95
6.4. In vitro assays.....	98
6.5. Single molecule microscopy	99
6.6. Live cell and FRAP measurements	102
6.7. Atomic Force microscopy	103
References	105
<i>Curriculum Vitae</i>	123

List of Figures

Figure 1. Structure of the nucleosome	1
Figure 2. Primary and secondary structures of chromatin	3
Figure 3. Histone post translational modifications.....	5
Figure 4. Examples of multivalent proteins	8
Figure 5. Structure of Heterochromatin protein 1	9
Figure 6. Protein labeling	11
Figure 7. Cysteine chemistry to produce histone PTMs	12
Figure 8. Dha tag for histone PTM synthesis.....	13
Figure 9. Sfp-catalyzed ybbR tag modification	14
Figure 10. Native chemical ligation	15
Figure 11. Cysteine desulfurization to alanine.....	16
Figure 12. Mechanism of intein cis-splicing.....	17
Figure 13. Expressed protein ligation	18
Figure 14. Affinity capture and protein modification by EPL	18
Figure 15. Jablonski diagram	20
Figure 16. Absorption and emission spectrum of fluorescent molecules	21
Figure 17. Oxygen scavaging system for fluorescence microscopy	22
Figure 18. Influence of the incidence angle of the laser beam in TIRFM	25
Figure 19. Wide-field vs total internal reflection fluorescence.....	26
Figure 20. Schematic representation of the three models explaining the retention of HP1 towards H3K9me3-modified chromatin.....	30
Figure 21. Synthesis of H3K9me3	31
Figure 22. H3K9me3 histone octamer refolding.....	32
Figure 23. Preparation of 12x 177bp labeled chromatin DNA	33
Figure 24. Reconstituted chromatin with different degrees of H3K9me3 octamers.....	33
Figure 25. Labeling strategy for the CGC peptide	34
Figure 26. HP1 α labeling	35
Figure 27. Preparation of microscopy glass coverslips.....	36
Figure 28. Different methods to passivate glass coverslips	37
Figure 29. Single molecule colocalization of HP1 to chromatin	38
Figure 30. HP1 α binding to H3K9me3 chromatin	40

List of Figures

Figure 31. Constrained dimeric HP1 α binding to H3K9me3 chromatin	42
Figure 32. Preparation of 12x 197bp labeled chromatin DNA	46
Figure 33. Preparation of H4Ks16ac	47
Figure 34. H3K9me3 & H4Ks16ac octamer reconstitution and chromatin refolding	48
Figure 35. HP1 binding to H3K9me3 & H4Ks16ac chromatin	49
Figure 36. Purification of Histone H1.1	50
Figure 37. Purification and labeling of H1.1-A532	51
Figure 38. Reconstitution of chromatin with H1.1.....	51
Figure 39. AFM imaging of chromatin fibers.....	52
Figure 40. Characterizing H1.1 residence on chromatin fibers.....	53
Figure 41. HP1 binding to condensed chromatin.....	54
Figure 42. Purification and labeling of HP1 β and HP1 γ	56
Figure 43. Electrophoretic mobility shift assay of HP1 α , HP1 β and HP1 γ	57
Figure 44 Purification and EMSA of the HP1 α hinge mutant	57
Figure 45. Microscale Thermophoresis.....	58
Figure 46. Microscale thermophoresis of HP1 α , β and γ binding to H3K9me3 peptide	59
Figure 47. HP1 α , HP1 β and HP1 γ binding to H3K9me3	60
Figure 48. HP1 α binding to H3K9me3-chromatin with increasing salt concentrations	61
Figure 49. Phosphorylation of HP1 α	62
Figure 50. Phosphorylated HP1 binding to H3K9me3-chromatin	63
Figure 51. In vivo dynamics of HP1 α (wild-type), HP1 α (AAAA-mutant) and HP1 α (hinge-mutant) using FRAP.....	65
Figure 52. Kinetic model of HP1 α binding.....	67
Figure 53. Kinetic modeling using stochastic simulations of HP1 binding to chromatin.....	68
Figure 54. Global sensitivity analysis of HP1 binding to chromatin	69
Figure 55. General strategy for single molecule multiplexing.....	73
Figure 56. Example of a single molecule decoding experiment	75
Figure 57. General single molecule multiplexing strategy	76
Figure 58 Chromatograms from RP-HPLC analysis of final purified oligonucleotides.....	77
Figure 59. Binding dynamics of decoders.....	78
Figure 60. USER enzyme digestion test.....	80
Figure 61. Microfluidics set-up.....	81
Figure 62. Two-layer multiplexing	82
Figure 63. Schematic representation of nucleosome DNA for Cas9 binding experiments.....	84

List of Figures

Figure 64. Preparation of H3K _s 56ac	85
Figure 65. Preparation of H2A.Z	86
Figure 66. In vitro Cas9 cleavage assay of free DNA and WT nucleosomes	86
Figure 67. Cas9 labeling.....	87

List of Tables

Table 1. Kinetic parameters of HP1 α interaction dynamics to chromatin	44
Table 2. Kinetic parameters of HP1 α interaction dynamics to condensed or open chromatin.	55
Table 3. Kinetic parameters of HP1 α , HP1 β and HP1 γ interaction dynamics.....	64
Table 4. Sequences of the 9 decoders.	76
Table 5. Sequences of primers with Uracils.....	79

Abbreviations

Ac	Acetyl
AFM	Atomic force microscopy
AIEX	Anion exchange chromatography
APTES	(3-Aminopropyl)triethoxysilane
ATP	Adenosine triphosphate
BME	2-Mercaptoethanol
bp	Base pair
BPTF	Bromodomain PHD finger transcription factor
BSA	Bovine serum albumin
Cas9	CRISPR associated protein 9
CD	Chromodomain
Ci	Curie
CK2	Casein kinase II
CoA	Coenzyme A
CSD	Chromo shadow domain
Dha	Dehydroalanine
DMEM	Dulbecco's modified eagle medium
DNA	Desoxyribonucleic acid
dNTP	Deoxyribonucleic acid triphosphate
DTT	Dithiothreitol
<i>E. Coli</i>	<i>Escherischia Coli</i>
EDTA	Ethylenediaminetetraacetic acid
EM	Electron microscopy
EMCCD	Electron multiplying charge-coupled device
EMSA	Electromobility shift assay
EPL	Expressed protein ligation
ESI-MS	Electrospray ionization mass spectrometry
Fmoc	Fluorenyl methoxy carbonyl
FPLC	Fast protein liquid chromatography
FRAP	Fluorescence recovery after photobleaching
FRET	Fluorescence resonance energy transfer

Abbreviations

GdmCl	Guanidine hydrochloride
H2A, H2B, H3, H4	Canonical Histone proteins
H2A.X, H2A.Z, CEMPA, H3.3	Non-canonical Histone proteins
H1, H5	Linker Histones
HBTU	N,N,N',N'-Tetramethyl-O-(1H-benzotriazol-1-yl)uronium hexafluorophosphate
HEPES	4-(2-hydroxyethyl)-1-piperazineethanesulfonic acid
Hi-C	High resolution chromosome conformational capture
HP1	Heterochromatin protein 1
IPTG	Isopropyl β -D-1-thiogalactopyranoside
LB	Luria-Bertani
Me	Methyl
MESNA	2-Mercaptoethanesulfonic acid sodium
MMTV	Mouse mammary tumor virus
MPAA	Mercaptophenylacetic acid
MS	Mass spectrometry
MST	Microscale thermophoresis
NA	Neutravidin
NaNO ₂	Sodium nitrite
NCL	Native chemical ligation
NHS	N-hydroxysuccinimide
Ni-NTA	Nickel nitrilotriacetic acid
NPS	Nucleosome positioning site
<i>Npu</i>	<i>Nostoc punctiforme</i>
NRL	Nucleosomes repeat length
NVA	N-vinyl acetamide
PAGE	Polyacrylamide gel electrophoresis
PBS	Phosphate-buffered saline
PCR	Polymerase chain reaction
PEG	Polyethylene glycol
Ph	Phosphate
PHD	Plant homeodomain

Abbreviations

PMSF	Phenylmethanesulfonyl fluoride
PRC	Polycomb repressive complex
PSF	Point spread function
PAINT	Points accumulation in nanoscale topography
PTM	Post translational modification
RNA	Ribonucleic acid
RP-HPLC	Reverse phase high pressure liquid chromatography
S ₀	Ground electronic state
S ₁	First excited state
SDS	Sodium dodecyl sulphate
SEC	Size exclusion chromatography
SHL	Super helix location
SPPS	Solid phase peptide synthesis
SUMO	Small ubiquitin-related modifier
Suv39h1/2	Histone-lysine N-methyltransferase
T ₁	First excited triplet state
TBE	Tris-boric acid-EDTA
TAD	Topologically associated domain
TAF1	Transcription initiation factor TFIID 1
TCEP	Tris(2-carboxyethyl)phosphine
TEAA	Triethylamine acetic acid
TFA	Trifluoroacetic acid
TFP	Tetrafluorophenyl
Thz	Thiazolidine
TIRFM	Total internal reflection fluorescence microscopy
Trolox	6-hydroxy-2,5,7,8-tetramethylchromane-2-carboxylic acid
USER	Uracil-specific excision reagent
VA-044	2,2'-Azobis[2-(2-imidazolin-2-yl)propane]dihydrochloride

1. Introduction

1.1. Chromatin structure

The genetic material of eukaryotic cells is stored in the form of chromatin, a DNA-protein complex that not only allows 2 meters of DNA to be tightly packed into the nucleus but also provides a tight regulation for gene expression¹. The basic structure of chromatin, known as the nucleosome, was first observed on electron microscopy (EM) analyses in the 1970s²⁻⁴, where ‘beads on a string’ structures were observed. It was around 20 years later that the first crystallographic structure at the angstrom resolution was solved by Luger *et al.* in 1997 (*Figure 1*)⁵.

1.1.1. The nucleosome core structure

The nucleosome core particle is disk-shaped with a diameter of 10 nm and a height of 2 nm and is composed of 147 base pairs of DNA (1.7 turns) wrapped around eight histone proteins; two copies of H2A, H2B, H3 and H4 (*Figure 1*)⁵.

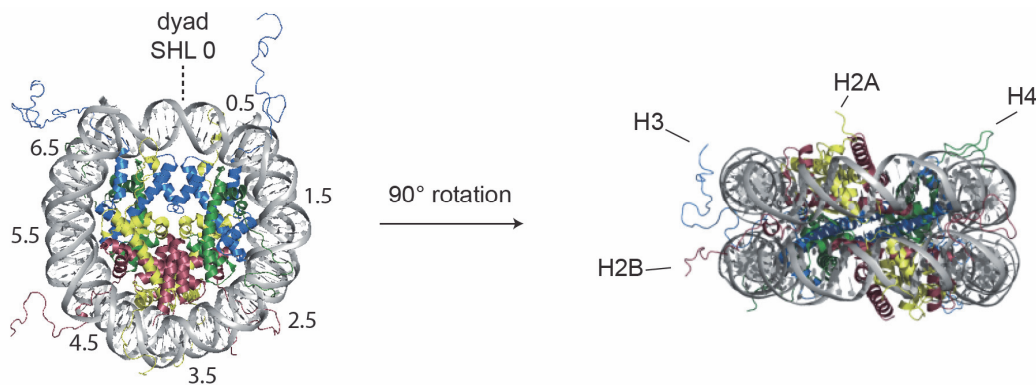


Figure 1. Structure of the nucleosome. 147 bp of DNA wrap around eight histone proteins; 2 copies of H2A in yellow, 2 copies of H2B in red, 2 copies of H3 in blue and 2 copies of H4 in green (PDB: 1KX5). Numbers around the nucleosome indicate the superhelical locations, SHL 0 is located at the nucleosome dyad.

It was observed from the crystal structure (*Figure 1*)⁵, that DNA wraps around the histone octamer in a left-handed superhelix with a single base-pair on the dyad axis defining the pseudo-2-fold symmetry axis. 7 superhelical locations (SHL) are observed along each side of the dyad axis which is defined as SHL 0 (*Figure 1*). The nucleosome core particle is stabilized by the interaction between the histone proteins and electrostatic interactions or hydrogen bonds between the proteins and the minor groove of DNA⁶. The four different histone proteins are

positively charged and contain a histone fold composed of three alpha helices; one main central alpha helix ($\alpha 2$) between two shorter helices ($\alpha 1$ and $\alpha 3$) linked by two loops (L1 and L2) that fold towards the interior creating a histone fold motif⁵. Histones possess positively charged, unstructured N-terminal tails, however, H2A also has a flexible tail at the C-terminus, providing 10 tails that protrude out of the nucleosome and a platform for the decoration of a number of post translational modifications (PTMs). The N-terminal tails of H4 and H2A protrude from the surface of the nucleosome whereas those of H3 and H2B protrude from between the DNA gyres⁷. Each histone binds to a complementary histone (histone H2A pairs with H2B and histone H3 pairs with H4) at the histone fold in an antiparallel manner creating a crescent-shape, where the external surface, composed of the L1 and L2 loops and the $\alpha 1$ helix, provide a strong positive charge creating an important platform for DNA interaction. The internal concave surface is composed of the $\alpha 3$ and $\alpha 2$ helices^{5,8,9}. H2A and H3 are canonical histones, but can be replaced by variants such as H2A.X, H2A.Z, H2A-Bbd, macro-H2A, H3.3 or CEMP-A¹⁰.

1.1.2. Hierarchical chromatin organization

Nucleosomes are linked to each other by short DNA segments called linker DNA that can vary in length (10-80 bp)¹¹ and create a ‘beads on a string’ structure of 10 nm in diameter (*Figure 2A*), also known as the **primary structure** of chromatin^{3,12}. Chromatin can be further compacted by contacts made between individual nucleosomes mediated by the highly basic tails of histone proteins that protrude out of nucleosomes to interact with the acidic patch of the neighbouring nucleosome^{13,14}. Nucleosomes may also be compacted by non-histone proteins that multivalently bridge nucleosomes¹⁵ or salts that neutralize the negatively charged DNA¹⁶. In physiological salt, (100-150 mM NaCl or 2-5 mM Mg^{2+}) chromatin fibers strongly condense *in vitro*¹⁶. Nucleosome packing is also achieved and stabilized by insertion of histone H1 binding at the entry/exit site of DNA, forming 30 nm chromatin fibers¹⁷, also known as the **secondary structure** (*Figure 2B*).

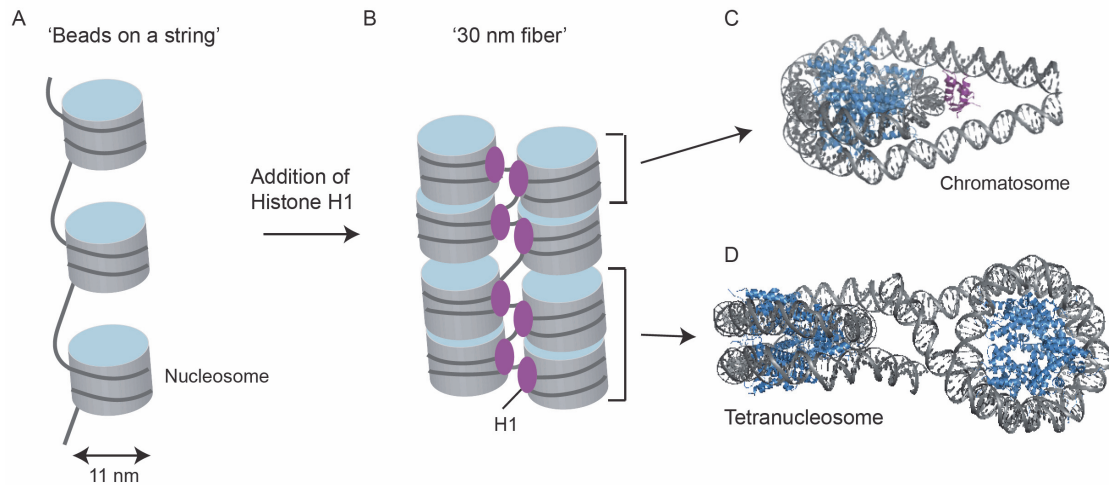


Figure 2. Primary and secondary structure of chromatin. A) The primary structure resembles a 'beads on a string' structure. B) Chromatin is further compacted into a 30 nm fiber structure by the addition of Histone H1. C) Crystal structure of the nucleosome with the globular domain of histone H1 (PDB: 5NL0). D) Tetranucleosome two-start helix crystal structure (PDB: 1ZBB).

Two main models of the 30 nm fiber (Figure 2B) have been extrapolated from cryo-EM or X-ray crystallography experiments; the one-start solenoid structure¹⁷ and the two-start zig-zag structure^{18–20}. Determining the structure of native chromatin fibers has been complicated since it is not homogeneous enough to be observed in high-resolution images, therefore structural studies were mostly performed on chromatin reconstituted *in vitro*, containing well defined interspersed nucleosomes with a highly defined controlled architecture. Owing to the compact structure of chromatin, its structure has been difficult to determine. Cryo-EM images of chromatin fibers with the addition of histone H5 (chicken linker histone) and different linker DNA lengths were interpreted to form a one-start interdigitated solenoid structure¹⁷. However, chromatin fibers stabilized by disulphide cross-links displayed a 2-start zig-zag structure¹⁸. X-ray crystallography of tetranucleosomes (Figure 2D) also confirmed a 2-start zig-zag structure with two stacks of nucleosomes connected by straight linker DNA¹⁹, however tetranucleosomes are too short to form solenoids. More recently a cryo-EM structure of 12-mer chromatin fibers with the addition of H1 displayed a two-start zigzag with 3 tetranucleosomal structural units²⁰, where binding of H1 at the dyad and entering/exiting DNA (Figure 2C) was shown to alter and constrain the angle of the linker DNA^{20,21}. Interestingly, EM-assisted nucleosome interaction capture (EMANIC), consisting in crosslinking internucleosomal contacts of condensed chromatin and then imaging in transmission EM the decondensed chromatin, showed that the two different conformations could be observed²², possibly displaying the dynamic behaviour of chromatin interchanging between the two conformations under different conditions. More recently ChromEMT (chromEM tomography), combining electron microscopy tomography

and a labeling method to enhance the contrast of DNA, was used to observe the 3D packing of human cells *in situ*. Higher-order fibers in human interphase and mitotic cells were not observed, however chromatin displayed a flexible and disordered 5 to 24 nm granular chain²³. Dynamics of reconstituted trinucleosomes and dodecanucleosomes were also studied^{24,25}, both experiments showed a two start dynamic tetranucleosome structure. smFRET revealed that nucleosomes can rapidly interchange between two tetranucleosomes by passing through an open conformation in the hundreds of millisecond timescale²⁴.

Finally, chromatin in the nucleus can form **higher order structures** from intermolecular interactions between secondary structures²⁶. Transcriptional enhancers interact with target genes by the formation of chromatin loops, providing spatial proximity of enhancers to promoters. Chromatin loops are constrained within larger loops called insulated neighbourhoods by the transcription factor CTCF and co-occupation of the cohesion protein complexes. Clustered neighbourhoods form sub-megabase scale domains contributing to topologically associated domains (TADs)²⁷. High resolution chromosome conformation capture (Hi-C) have shown that regions within the same TAD tend to interact more than with regions outside their TAD. TAD boundaries are enriched with CTCF and cohesin. Chromatin compaction changes throughout the cell cycle have been investigated by Hi-C^{28,29}; In the G1 phase, TADs are insulated from one another, by occupying distinct nuclear compartments. In the S phase, where DNA replication takes places, the TADs are still present, however less insulated. In the M phase, chromatin is highly compacted with very short-range contacts between different TADs.

Several studies have shown that disruptions in TAD boundaries resulted in pathogenic phenotypes, leading to a loss of insulated neighbourhood boundaries and enhancer-promoter contacts that would otherwise not be present in the same neighbourhood^{30,31}. These results display the importance of the complex 3D structure of chromatin in the cell nucleus.

1.2. Post translational modifications

Epigenetic mechanisms involve inheritable changes in gene expression and phenotype without changing the DNA sequence. Epigenetic processes include nuclear organisation of the genome, 3D positioning of interphase chromosomes as well as the presence of histone PTMs, DNA methylation and non-coding-RNAs³². These processes are interconnected and histone PTMs present a central importance in understanding epigenetic mechanisms.

1.2.1. Histone modifications

All four histone proteins contain a globular domain and tails that protrude out of the nucleosome. These tails display various post translational modification (PTMs) (Figure 3A) covalently attached by transferase enzymes, known as ‘writer’ proteins. These PTMs vary from small modifications such as methylation, acetylation, phosphorylation to larger proteins such as ubiquitin or SUMO (Figure 3B)³³. Recently, many other PTMs have been discovered such as crotonylation, butanylation, citrullination and glycosylation to name a few³⁴.

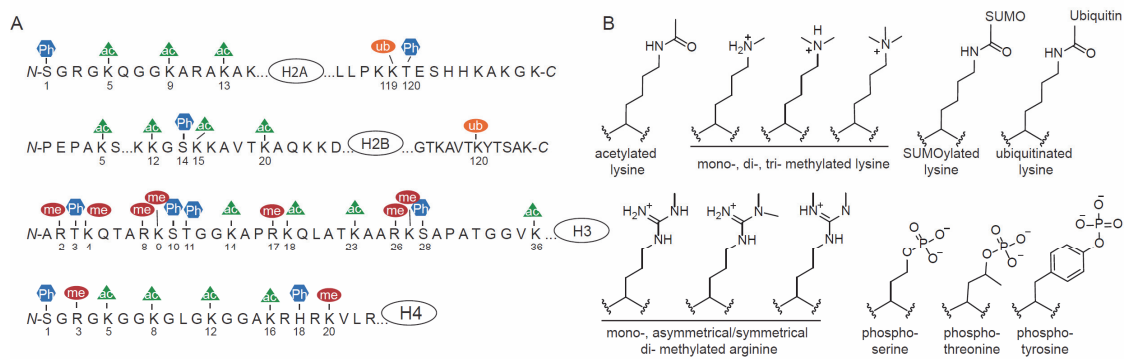


Figure 3. Histone post translational modifications. A) Common histone post-translational modifications on H2A, H2B, H3 and H4. Ac: acetylation, ph: phosphorylation, ub: ubiquitination, me: methylation. B) Examples of common post translational modifications, acetylation on lysine, mono-, di- or tri- methylation on lysine, monomethylation or asymmetric/symmetric dimethylation on arginine, SUMOylation on lysine, ubiquitination on lysine, phosphorylation on serine, threonine and tyrosine.

The large variety of different post translational modifications and the different available sites on histones lead to a huge variety of combinations with different biological outputs. This has been described as the **histone code hypothesis**^{33,35}. The combination of PTMs is carefully regulated; histone PTMs are deposited by ‘writer’ effector proteins and removed by ‘eraser’ histone modifying enzymes. The combination of PTMs is read out and interpreted by ‘reader’ domains. Understanding the underlying mechanisms of the histone code is important since misregulation of the specific patterns caused by deregulation of effector proteins have been shown to lead to deregulated gene expression and perturbation of cellular identity playing a major contribution to cancer^{36,37}.

Histone post translational modifications alter DNA accessibility and chromatin structure by two distinct mechanisms^{38,39}; by **directly** disrupting DNA-histone or histone-histone contacts (cis-effect) or by **recruiting non-histone proteins** (trans-effect).

1.2.2. Cis-effect of histone PTMs

Certain PTMs affect the structure of chromatin owing to a modification in the charge of the amino acid, for example acetylation neutralizes the positive charge on lysine or phosphorylation introduces negative charges (*Figure 3B*). For example, H4K16ac is thought to prevent the interaction of the H4 tail to the acidic patch of the neighbouring nucleosome and leads to decompaction of chromatin fibers⁴⁰. Another acetylation, positioned at K56 on histone H3, found at the entry exit site of DNA, leads to the removal of the positive charge on lysine 56. The interaction between H3K56 and DNA is thereby lost and leads to unwrapping of DNA⁴¹. The histone phosphoryl mark (*Figure 3B*) is far less studied than the acetyl mark, however studies have shown that H3T118ph, located at the dyad axis region, increases accessibility to DNA at the dyad axis but not at the DNA entry/exit site and leads to a dramatic increase in the remodelling factor SWI/SNF activity compared to wild type nucleosomes⁴². Addition of larger PTMs such as ubiquitin, a 76 amino acid protein, increases steric bulk to the amino acid. For example ubiquitination of H2B at K120 prevents nucleosome compaction to provide accessibility to DNA^{43,44}.

An important consideration to make from these examples is that PTMs have an influence on DNA wrapping⁴⁵. Nucleosomes are not static and do not have the DNA completely wrapped around the histones as depicted by the crystal structure model, they are in fact highly dynamic providing a controlled route for remodelling factors and polymerases to interact with DNA²⁵. The main effect of DNA wrapping around histone proteins is that it sterically prevents proteins from binding to DNA. Depending on the location of the PTM, dynamic changes in the nucleosome include unwrapping and rewrapping of DNA, sliding of the octamers on the DNA, assembly and disassembly of the nucleosomes and formation or disruption of interactions between histones or histones and DNA⁴⁵.

1.2.3. Trans-effect of histone PTMs

PTMs also provide an indirect biological effect by recruiting effector proteins. Methylation is recognized by chromo domains, tudor domains, malignant brain tumor (MBT) domains and the plant homeodomain (PHD) finger. Acetylation of lysine is recognized by bromodomains and phosphorylation is recognized by a domain within 14-3-3 proteins³⁹. Effector domains individually interact to histone PTMs with low affinity, usually with a dissociation constant in the micromolar range⁴⁶. However, chromatin-binding proteins are

generally either composed of several binding domains that provide multiple interactions to the nucleosome or they can oligomerize to form higher order complexes such as dimers³⁹. This multivalent binding results in higher affinity towards chromatin, whilst remaining highly dynamic compared to tight monovalent-interacting proteins⁴⁷ and may in turn be more readily competed. The binding affinity of one domain towards its specific PTM is given by *Equation 1*.

$$\Delta G_i = \Delta H_i - T\Delta S_i \quad (1)$$

Affinity enhancement of multivalent proteins is provided by the addition of the enthalpy for each binding module with an entropy corresponding to one binding module owing to the constrained structure of the protein³⁹ (*Equation 2*).

$$\Delta G_{2i \text{ complex}} = 2\Delta H_i - T\Delta S_{\text{complex}=i} \quad (2)$$

Additional interactions of multivalent proteins to histone PTMs on chromatin fibers lead to an increased local concentration and to an increase in the association rate. These interactions include specific (methylated DNA) and unspecific DNA interactions and areas that do not contain PTMs such as the acidic patch on octamers.

Many effector proteins have been shown to bind in a multivalent way. An example of multivalency through dimerization is Heterochromatin Protein 1 (HP1) implicated in the formation of heterochromatin. HP1 contains a chromodomain that binds with low affinity to methylated K9 on histone H3 (*Figure 4A*). It also contains a chromo shadow domain that enables two monomers to dimerize and increase its overall affinity to H3K9me3 containing chromatin. Since the main focus of my thesis was to decipher HP1 dynamics binding to H3K9me3-chromatin, a separate sub-chapter is dedicated to this effector protein later on (*see Chapter 1.3.1*).

Other multivalent effector proteins bind to several modifications on the same histone tail. TAF1 (TATA-binding protein-associated factor 1), a subunit of the TFIID basal transcription factor contains a tandem bromodomain constrained in a conformation where both domains are oriented in the same direction, suggesting that they can bind to two acetylated lysines 25 Å apart⁴⁸ (*Figure 4B*). A single domain binds with a low affinity of 100-350 μM, whereas the tandem bromodomain increases the binding affinity to 1-20 μM^{48,49}.

Multivalent protein can also bind to modifications on two different histone tails. BPTF (Bromodomain PHD finger transcription factor), a component of the remodelling factor

(NURF) complex. As the name suggests, it contains both a bromodomain and a PHD finger that bind to both H4K16ac and H3K4me3 respectively, with increased affinity compared to individual binding⁵⁰ (Figure 4C).

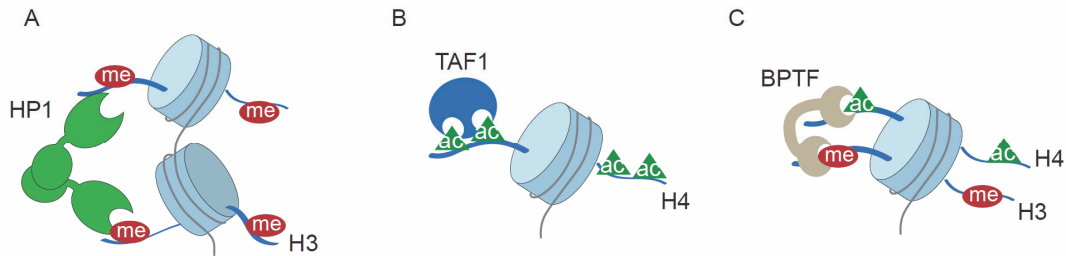


Figure 4. Examples of multivalent proteins. A) HP1 dimerizes through the chromo shadow domain providing higher affinity to H3K9me3-chromatin compared to the monomer. B) TAF1 is composed of two bromodomains that each bind to acetylated marks on the same histone H4 tail. C) BPTF is composed of a bromodomain and a PHD finger that bind to marks on two different histone tails; H3K4me3 and H4K16ac.

1.3. Heterochromatin and Euchromatin

As mentioned previously, PTMs either disrupt directly DNA-histone or histone-histone contacts or recruit effector proteins. However, PTMs combinations are tightly regulated and localized in defined areas, generating the establishment of chromatin environments.

Historically, genomic DNA in eukaryotes has been divided into two distinct forms; **euchromatin** and **heterochromatin**. Euchromatin is defined as being transcriptionally active, loosely packaged with gene rich regions together with high levels of acetylation and low levels of methylated H3K4, H3K36 and H3K79 whereas heterochromatin remains condensed throughout the cell-cycle and is gene poor with low levels of acetylation, high levels of methylated H3K9, H3K27 and H4K20 with the presence of Histone H1, HP1 or Polycomb repressive complexes^{35,51}. Interestingly exceptions have been found, where H3K27me (silent chromatin) and H3K4me (active chromatin) were present on same nucleosomes in mouse embryonic stem cells⁵². These are known as bivalent domains, that contain both activating and repressive modifications. In this way, genes are expressed in low levels and maintain the cell's pluripotency, but are poised for rapid activation.

Transition between heterochromatin and euchromatin is influenced by DNA methylation, non-coding RNAs or incorporation of histone variants. Histone modifications are also involved in various mechanisms for the transcription of a gene, DNA repair or replication and chromosome

condensation. One of the central factors for the establishment and maintenance of heterochromatin is the presence of HP1.

1.3.1. Heterochromatin Protein 1

Heterochromatin protein 1 (HP1) is a well-known structural effector which binds to H3K9me2/3 and is involved in chromatin compaction, gene repression, telomere maintenance and DNA repair^{53–56}. HP1 is evolutionarily highly conserved, and has orthologues in various organisms, ranging from *S. pombe* (Swi6), *Drosophila* (HP1a, HP1b and HP1c), *Xenopus* (XHP1 α and XHP1 γ) to mammals in which three isoforms; HP1 α , HP1 β and HP1 γ have been identified^{55,57}. These isoforms are similar in terms of amino acid sequence, structural organization, but differ in nuclear localization. HP1 α and HP1 β are primarily associated with heterochromatin, whereas HP1 γ also localizes to euchromatin⁵⁸. Mice experiments where the three isoforms were individually knocked-out showed different phenotypes manifesting their distinct mechanisms; HP1 α knockout displays no phenotype, whereas HP1 β knockout is associated with genome instability and defects in neurological development⁵⁹ and HP1 γ expressed in low levels displayed defects in spermatogenesis⁶⁰.

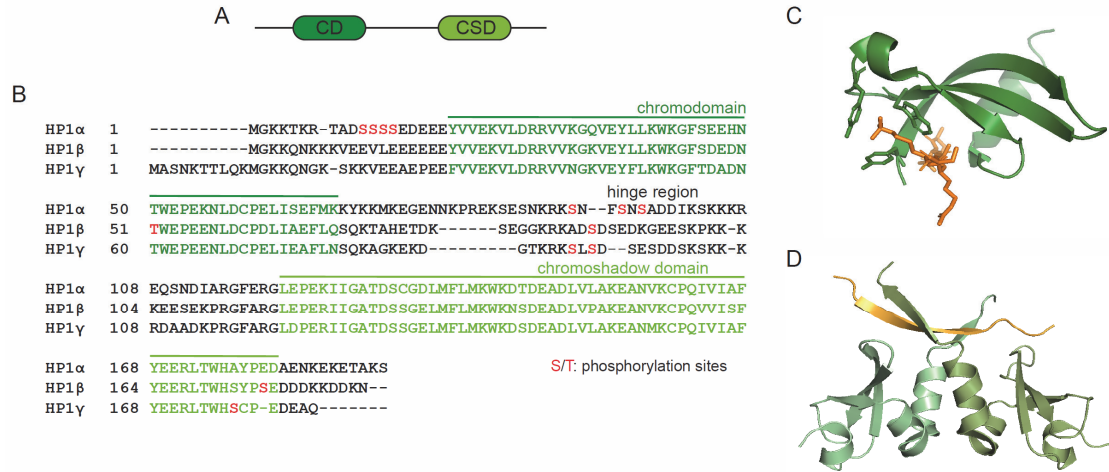


Figure 5. Structure of Heterochromatin protein 1. A) Schematic representation of HP1 where the chromodomain is linked to the chromo shadow domain by the hinge region. B) Sequence alignment of the three HP1 isoforms. C) Crystal structure of the chromodomain in complex with a H3K9me3 peptide (PDB: 1KNE) D) Crystal structure of the dimerized chromo shadow domain (PDB: 3Q6S).

HP1 proteins are composed of three main parts; the N-terminal chromodomain (CD), the chromo shadow domain (CSD) and a hinge region which connects the two domains (Figure 5A-D). The CD binds to H3K9me2/3 with a dissociation constant of $\sim 1-10 \mu\text{M}$ ^{38,61–63}, whereas the CSD is implicated in protein homo- or heterodimerization^{63,64} and mediates interaction with

other proteins displaying a PxVxL or PxVxI motif^{65,66}. Dimeric HP1 can bind multivalently to chromatin by engaging two H3K9me3 sites, thereby cross-bridging nucleosomes^{67,68} and reducing access for transcriptional machinery^{69,70}. The flexible hinge region (HR), enriched in positively charged amino acids, binds non-specifically to DNA and RNA⁷¹.

Similar to histones, HP1 proteins are decorated with PTMs such as methylation, phosphorylation (*Figure 5B*) or SUMOylation^{72–74}. For example, HP1 γ phosphorylation at Serine 83 is found exclusively at euchromatin, has impaired silencing activity and serves as marker for transcription elongation⁷⁵. Phosphorylation on the four serines at the N-terminal of HP1 α prevent its unspecific binding to DNA⁷⁴. PTMs on HP1 proteins most probably influence their targeting to different regions of the nucleus, however many of these have yet to be studied.

Time-lapse microscopy revealed that HP1 localizes to domains, which are relatively immobile and stable overtime⁷⁶. Fluorescence recovery after photobleaching (FRAP), where the fluorescence recovery of HP1-GFP is measured after bleaching a small area, revealed that in euchromatin HP1 binding is transient with a complete recovery time of 5 s, in heterochromatin HP1 interaction is longer with a recovery time within 60 s⁷⁶. HP1 is highly dynamic in localized domains^{76–78}, suggesting that the continuous exchange of HP1 is important for their maintenance. HP1 is present at low micromolar concentrations at heterochromatin and requires the presence of both H3K9me3 and H3K9me3 methyltransferases (Suv39h1/2), which bind to the CSD of HP1, for enrichment at these foci⁷⁷. The propagation of heterochromatin is probably ensured once an initiating site has been established. This propagation would involve a ‘self-sustaining’ loop, in which HP1 binds to H3K9me3 histones which leads to the recruitment of more H3K9 histone methyltransferases, from interaction with the CSD^{56,77}. Another regulatory path has also been observed, where HP1 recruitment to heterochromatin is disrupted. When S10 on histone H3 is phosphorylated by Aurora kinase during M phase, the affinity of HP1 to H3K9me3 is greatly reduced, implying a regulatory switch for HP1-H3K9me3 interaction⁷⁹.

HP1 is a well-studied effector protein, however one main question remains unanswered and will be addressed in this thesis: How does HP1 manage to mediate the formation of stable heterochromatin domains despite its highly dynamic interaction to H3K9me3 sites?

1.4. Protein engineering

A large amount of research is carried out to decipher the implication of effector proteins binding to individual or combinations of PTMs. In order to study specific PTMs *in vitro* for

biochemical, structural or biophysical experiments, synthetic chromatin is reconstituted and effector proteins are recombinantly expressed and purified. Nucleosomes extracted from cells cannot be used since they would contain many different histone modifications with no way of controlling their presence. To this end, a bottom-up technique has been developed to homogeneously produce synthetic chromatin containing PTMs of choice.

Different methods have been developed to produce histone proteins with specific PTMs or to provide labeled proteins. These methods include; cysteine chemistry, native chemical ligation, expressed protein ligation, enzymatic reactions or genetic code expansion methods.

1.4.1. Cysteine chemistry

Cysteines provide an important handle for site specific reactions for labeling proteins or inserting post translational modifications. Cysteines are found in low abundance in proteins, therefore a site specific mutation can be done to insert single cysteines, to which various reactions may subsequently be performed.

A variety of dyes are conjugated to maleimides (*Figure 6A*) or iodoacetamides (*Figure 6B*), these electrophiles react readily with the nucleophilic cysteines to provide labeled proteins⁸⁰. Reactions with iodoacetamides are slower and less specific whereas maleimides are potentially reversible with competitive thiols of maleimides or hydrolysis that can lead to subsequent decomposition of protein conjugates.

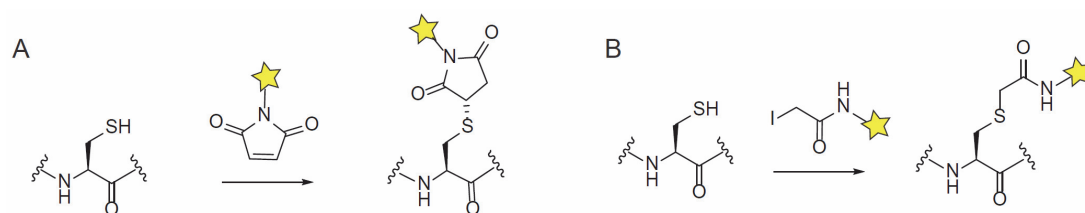


Figure 6. Protein labeling. Two different methods to site specifically label proteins on a cysteine, either by the reaction of A) maleimide-linked dye or B) iodoacetamide-linked dye.

Aminoethylating agents are used to provide histone postranslational modification analogs (*Figure 7A-C*). Methyllysine analogs are produced by the alkylation of the cysteine residue with an electrophilic ethylamine⁸¹. The methyllysine analog contains a sulphide instead of the γ -methylene which leads to a slightly lengthened side chain of 0.28 Å and the pK_a changes slightly by -1.1, increasing the acidity of the ammonium protons slightly⁸². Disulfide linkages have also been exploited (*Figure 7D*) for example with the ubiquitination of H2B, where the ubiquitin with a C-terminal aminoethanethiol linker provided by expressed protein ligation (*see*

chapter 1.4.1) was reacted with H2B-aromatic thiol to form the disulphide-linked ubiquitylated H2B. The disulfide link leads to a slightly longer side chain of 2.4 Å⁸³.

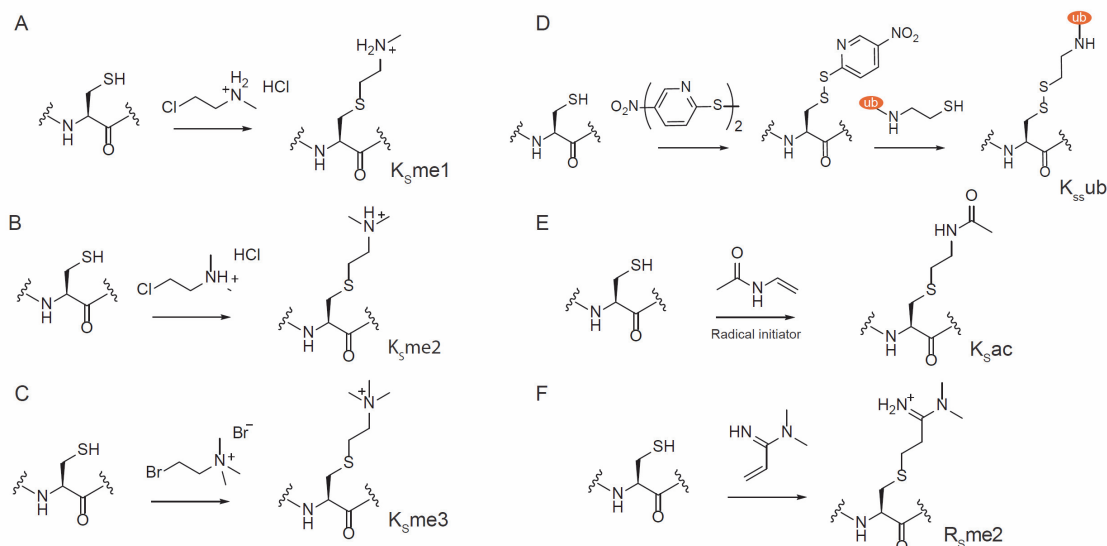


Figure 7. Cysteine chemistry to produce histone PTMs. A-C) Methyllysine analogs are produced by the alkylation of the cysteine residue with an electrophilic ethylamine. D) Disulfide linked ubiquitin. E) Thiol-ene addition with N-vinyl acetamide to produce the acetyllysine analog. F) α,β -unsaturated amidine precursors produce methylated arginine analogs.

The analog of acetyllysine is produced by the thiol-ene addition of N-vinyl acetamide (NVA) to the cysteine^{84,85} (Figure 7E). At the initiation step, a radical thiyl is produced by heat and addition of a radical initiator (VA-044). The cysteine then reacts with NVA to provide a carbon radical, in turn reacting with another cysteine at the radical chain transfer step giving an acetyllysine analog and a new radical cysteine, thereby propagating the reaction. This reaction is described later on, where I synthesised two different acetyllysine analogs; H4K16ac (Figure 33) and H3K56ac (Figure 64). A final example, is the synthesis of methylarginine which is produced by reacting different α,β -unsaturated amidine precursors (Figure 7F).

The resulting modifications are analogs and are slightly longer and more flexible than native amino acids. Davis *et al.* have worked on developing a technique where the cysteine is chemically converted to a dehydroalanine (Dha) followed by the reaction with alkyl halide reagents through a radical reaction producing natural and unnatural aminoacids (Figure 8). This technique has potential in producing a number of different histone PTMs, for example methylated lysine and methylated arginine^{86,87}.

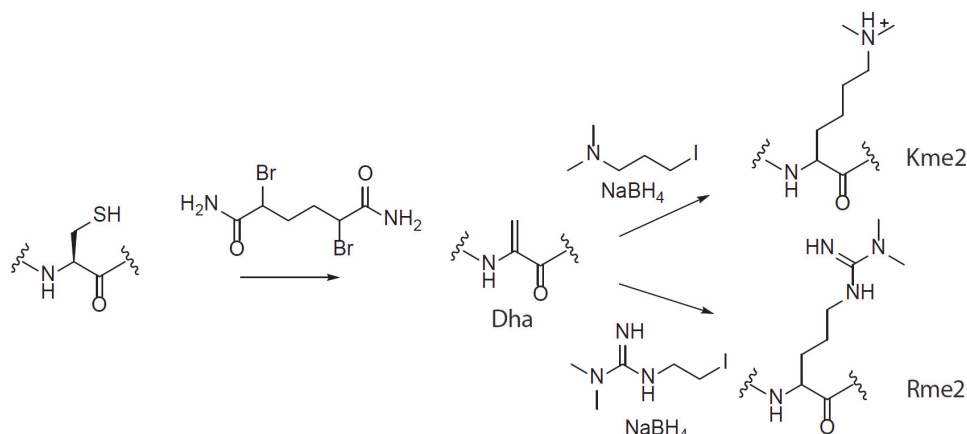


Figure 8. Dha tag for histone PTM synthesis. Cysteine is converted to the dehydroalanine tag, that provides a handle for the synthesis of different PTMs by reacting with alkyl halide reagents.

Cysteine chemistry remains one of the most straightforward methods to produce histone PTMs. However, there are limitations; only one type of PTM can be introduced into the individual proteins, most of these techniques provide analogs to the modifications and if the protein already contains cysteine these have to be mutated and may have an influence on the protein's structure and mechanism.

1.4.2. Enzymatic reactions

Dyes and short tags can also be added to proteins by enzymatic reactions. For example, Sfp phosphopantetheinyl transferase, naturally found in *Bacillus subtilis*, covalently transfers the 4'-phosphopantetheinyl group of Coacetyl A (CoA) to the conserved serine residue on the peptide carrier proteins (PCP) or the acyl carrier protein (ACP) domains in non-ribosomal peptide synthetases and polyketide synthetases respectively^{88–90}.

This Sfp catalysed reaction was used to label proteins fused to PCP with small-molecule probes such as biotin, dyes, crosslinked peptides and sugars^{91,92}, however the 80 residue-PCP is relatively bulky and has been optimized towards the development of a ybbR tag that is only 11 residues in length^{89,90} (Figure 9). The ybbR tag can be fused to the N or C terminus of the protein and even inserted into a flexible loop.

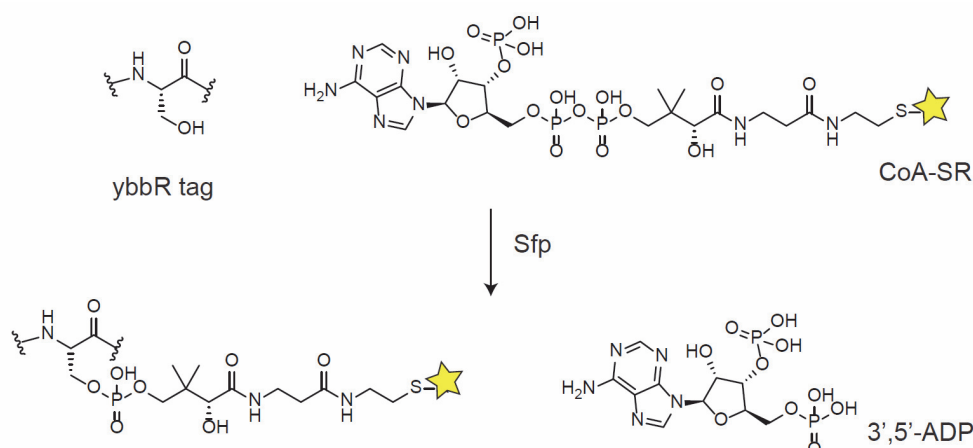


Figure 9. Sfp-catalyzed ybbR tag modification at a specific serine residue. The ybbR tag (DSLEFIASKLA) is fused to the protein. Sfp transferase catalyses the reaction where CoA is modified with a small molecule of choice (dye, biotin, sugars) and transfers specifically the small molecule to the serine of the ybbR tag and releases a 3',5'-adenosine diphosphate.

1.4.3. Native chemical ligation

Native chemical ligation (NCL) is based on the ligation of two peptides, one with a C-terminal α -thioester and the other with a 1,2 aminothiol, thereby providing a native bond at the ligation site^{82,93}. The advantage of chemically synthesized peptides, is that they are not limited to the 20 natural amino acids and one or several PTMs can be introduced into the protein of choice.

The synthesis of peptides by solid phase peptide synthesis (SPPS) was developed in 1963 by Merrifield⁹⁴. This technique relies on the repetition of cleaving the α -amino protecting group of an amino acid, washing, then coupling of the next amino acid and washing again. Peptides are synthesized from the C to N terminus, as opposed to natural ribosomal synthesis. The C-terminal amino acid is linked to a solid surface with an α -amino protecting group. The side chains are also protected by protecting groups that are only removed once the peptide is synthesized. Different types of protecting groups exist, the most popular is Fmoc (N-(9-fluorenyl)methoxycarbonyl) since its cleavage requires mild basic conditions enabling the use of mild acid-labile protecting groups such as Boc (*tert*-butoxycarbonyl) and benzyl groups to protect amino acid side chains⁹⁵.

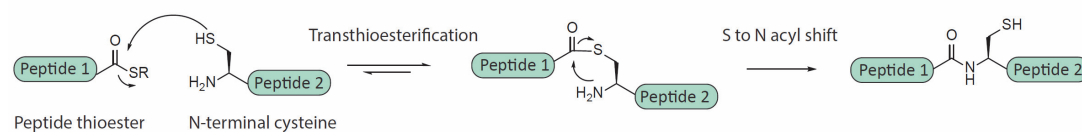


Figure 10. Native chemical ligation. The peptide thioester and the cysteine-peptide react to form a thioester-linked intermediate that undergoes a spontaneous rearrangement, via an intramolecular nucleophilic attack to provide a native amide.

Once the synthesis of the peptide is complete, it is cleaved off the resin and purified. The disadvantage of SPPS is that it is limited to the synthesis of up to 50 amino acids owing to statistical coproducts^{93,94}. In order to synthesize longer than 50 amino acid peptides, native chemical ligation (NCL) was developed by reacting two short peptides together, one containing a C-terminal thioester peptide and a second peptide containing an N-terminal cysteine^{96,97} (Figure 10).

Both peptides are synthesized by SPPS with one or multiple PTMs. The two peptides undergo a reversible thiol/thioester exchange in the presence of a suitable thiol catalyst. The transient formation of the thioester undergoes a nucleophilic rearrangement by a highly favoured intramolecular mechanism to provide a native amide bond. Importantly, the second step of the reaction, where the intramolecular nucleophilic attack takes place is virtually irreversible and over time, all the equilibrating intermediates are depleted by this irreversible step.

NCL has been widely used in protein semi-synthesis, where the natural protein fragment containing an N-terminal cysteine is ligated to a thioester peptide. To semisynthetically reproduce a modified histone, the tail with the desired PTM is synthesized by SPPS and ligated to the recombinantly expressed globular domain with a cysteine at the N-terminal^{85,98}. However, peptide thioesters remain challenging to synthesize with Fmoc protecting group chemistry⁹⁹. One way to obtain the thioester peptide is to synthesize it with a hydrazide which can then be converted to an azide with the addition of an oxidant such as NaNO_2 , followed by addition of MPAA (4-mercaptophenyl acetic acid) to produce the thioester which is then reacted with the N-terminal cysteine-peptide¹⁰⁰ (method used for the synthesis of H3K9me3 see Chapter 2, Figure 21). In addition, the desulfurization of the cysteine to alanine at the ligation site produces a traceless modified histone protein (Figure 11). This conversion follows a thiyl radical mechanism (Figure 11)^{101,102}. The cysteine radical thiyl is generated by the addition of VA-044 and heat. The thiyl radical then reacts with the alkylphosphine of TCEP to form a phosphoranyl

radical. Finally, alanine is produced from homolytic cleavage by abstracting the hydrogen of a neighbouring cysteine peptide, forming a new radical and propagates the reaction¹⁰¹.

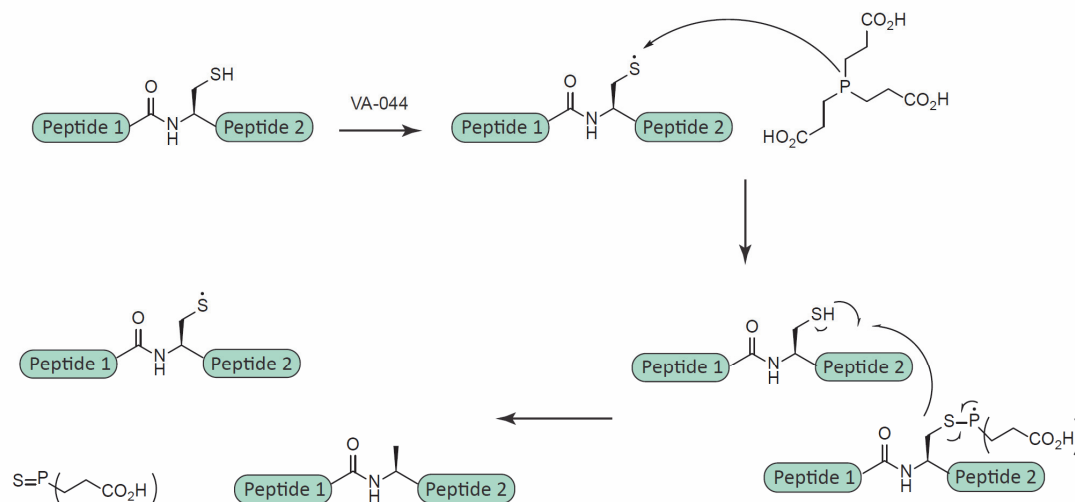


Figure 11. Cysteine desulfurization to alanine. The cysteine radical is initiated by the addition of VA-044 and then reacts with TCEP to form a phosphoranyl radical. Homolytic cleavage results in the alanine peptide and the production of a new cysteine radical.

1.4.4. Expressed protein ligation

Native chemical ligation was an important advancement in the development towards synthesizing histone proteins containing PTMs. The main disadvantage with this technique is that peptide synthesis is limited to 50 amino acids in length. Large semi-synthetic proteins can be prepared from ligating several peptides, however this remains technically challenging and is limited to proteins smaller than around 15 kDa. To overcome this, NCL has been extended to expressed protein ligation (EPL), where the peptide containing a N-terminal cysteine is ligated to a recombinant α -thioester protein¹⁰³.

Intein splicing enables the introduction of a thioester at the C-terminal of the protein which is in turn ligated to a cysteine-containing peptide. Inteins are found in eubacteria, archaea and eucarya¹⁰⁴ and are embedded within essential proteins involved in DNA replication, transcription, and maintenance¹⁰⁵. Intein splicing is an auto-processing event where an intein (intervening protein) excises itself out from a host protein by cleaving two peptide bonds and ligates the exteins (external protein) through the formation of a new peptide bond¹⁰⁶ (Figure 12). The advantage of protein splicing mediated by inteins is that it is a spontaneous reaction and only requires the folding of the protein and no other energy source¹⁰⁶.

Inteins are divided into two main types of splicing:

cis-splicing: This is the most common type of intein, where the intein is expressed as a whole between two exteins¹⁰⁷ (Figure 12). Initiated by the activation of the peptide bond between the N-extein and the intein; the cysteine at the N-terminus of the intein attacks the carbonyl carbon of the C-terminal N-extein. The N to S acyl shift leads to a linear thioester. The cysteine, which is the first residue of the C-extein attacks the thioester leading to a transthioesterification. The C-terminal asparagine of the intein cyclises to form a succinimide and excises the intein. The new bond at the extein, rearranges through a S to N acyl shift to result in a peptide bond. The example is given with a cysteine, however this also works for threonine and serine.

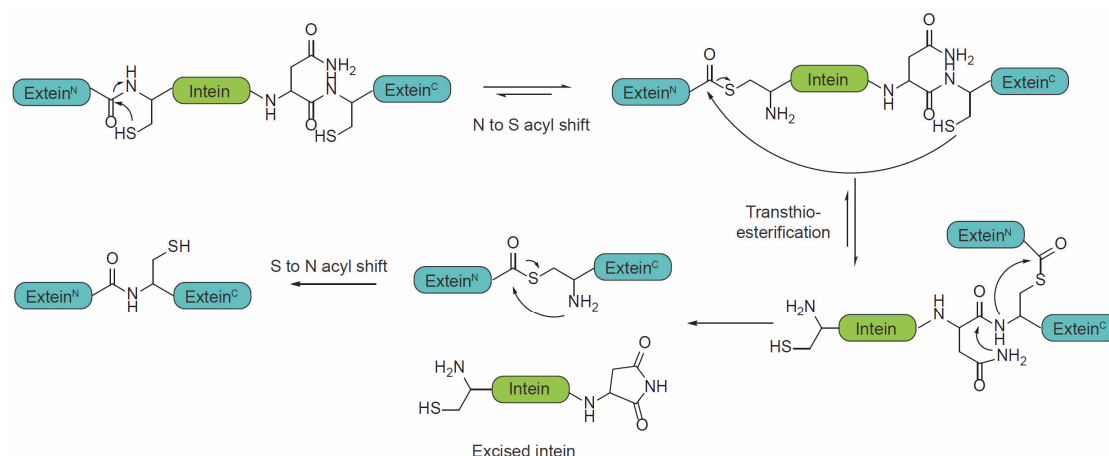


Figure 12. Mechanism of intein cis-splicing. The cysteine attacks the carbonyl group of the peptide bond at the C-terminal of the N-extein, leading to an N to S acyl shift, followed by transthioesterification. The C-terminal asparagine of the intein then cyclises and excises out the intein. The peptide bond is found after a S to N acyl shift.

trans-splicing: the two fragments of the intein are expressed separately (N-intein and C-intein) and fused to an extein. Individually, they do not provide activity, however, once expressed, inteins non-covalently associate and the same chemical steps as for the cis-splicing are observed¹⁰⁸.

The general strategy of EPL is the following: the protein of interest is expressed with a mutated intein, where there is a C-terminal alanine instead of asparagine to block the final step in protein splicing¹⁰⁷. The first step is an N to S acyl shift between the cysteine at the N-terminal of the intein and the peptide bond at the C-terminal of the protein. Cleavage of the intein is obtained by the addition of a small molecule alkyl or aryl thiol to provide the protein thioester which is then ligated to the N-terminal peptide by NCL to provide a native peptide bond.

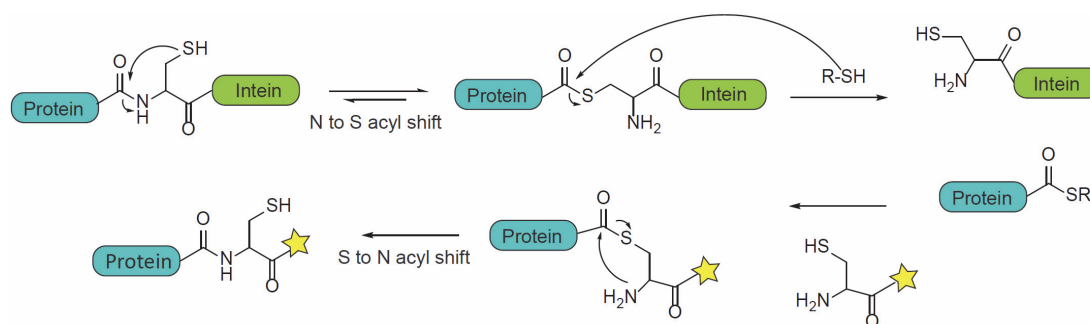


Figure 13. Expressed protein ligation. The protein is expressed with a C-terminal intein. The cysteine attacks the carbonyl group of the peptide bond at the C-terminal of the protein. Addition of an alkyl or aryl thiol leads to cleavage of the intein, producing a thioester which is then ligated to a N-terminal cysteine peptide by NCL.

Trans-splicing is also exploited for EPL. Muir *et al.* developed a method where the N-terminal of the split intein was fused to the protein and the C-terminal of the intein was covalently linked to a column^{107,109} (Figure 14). The protein can be cleaved off the column by adding a small molecule thiol (for example: mercaptoethanesulfonate) and thereby provides a C-terminal thioester which can react with a N-terminal peptide providing a semisynthetic protein. This technique has the advantage that cell lysates can be used, split inteins are fast and there is no premature cleavage from the N-intein before binding to the immobilized C-intein since the intein is split. This method was used for the labeling of HP1, where HP1 was expressed with the N-terminal intein and added to a column with the C-terminal intein. The protein was cleaved off and ligated to a C-terminal labeled peptide (Figure 26).

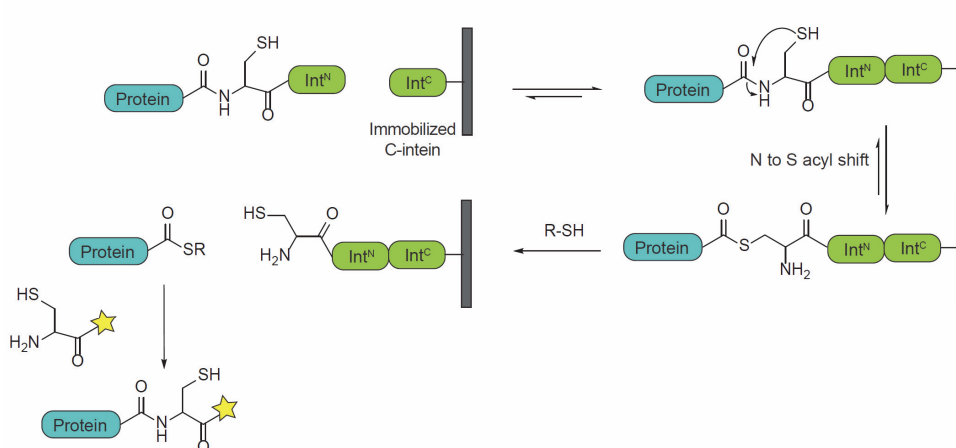


Figure 14. Affinity capture and protein modification by EPL. The protein is expressed with an N-terminal split intein and the C-split intein is attached to a column. The split inteins associate and excise out the protein, giving a thioester that can then react by NCL to a N-terminal cysteine peptide.

1.4.5. Amber suppression

Whereas the previous methods described chemical methods to obtain PTMs, amber suppression follows a biological route. Three codons; TAA, TGA and TAG, do not encode for an amino acid but lead to the termination of the protein synthesis at the ribosome. The amber stop codon (TAG) is the least used in *E. Coli* and has been reprogrammed to introduce an unnatural amino acid through the intermediate of an orthogonal aminoacyl-tRNA synthase/tRNA pair^{110,111}. The new aminoacyl-tRNA synthase aminoacylates the orthogonal tRNA with the unnatural amino acid, which is then incorporated into the polypeptide at the amber stop codon. This technique has been developed to provide the incorporation of a range of modified amino acids. The efficiency of the modified protein is also dependent on the synthetase system used and the type of modification. Addition of more than one PTM is often too complicated to incorporate in a protein due to the limitation on the number of orthogonal codons.

1.5. Fluorescence Microscopy

Many different methods in biochemistry, structural biology or biophysics may be used to study the implication of effector proteins binding to individual or combinations of PTMs. However, standard in vitro techniques, or ensemble measurements do not discriminate between individual molecules, they provide an average over the population of all the molecules. This means that there is no way of obtaining information about the behaviour of each molecule overtime. From in vitro ensemble measurements, molecules may seem to behave in a homogeneous way, however these molecules are not and possess intermolecular variations¹¹². Single molecule methods have been developed in order to address this issue, providing ways to observe individual molecules of a population. There are two main single molecule approaches; the first one is fluorescence microscopy that allows the visualization of single molecules under thermodynamics (non)equilibrium, for example by measuring the dynamics of an effector protein to nucleosomes. Other methods apply force to study molecules such as magnetic/optical tweezers^{112,113}, applied for example to understand nucleosome dynamics by applying force to unwrap DNA of nucleosomes. In this thesis we will focus on the first method; single molecule fluorescence microscopy.

1.5.1. Principles of fluorescence

Fluorescence was first described in 1845 by Sir Frederik Herschel and later in 1852 by Sir George Stokes. Its physical explanation was provided by Alexander Jablonski in 1935. In the 1990s, cloning of the green fluorescent protein and its derivatives pushed the field of fluorescence microscopy further. Since then, a large number of different fluorophores have been developed and microscopy techniques optimized to improve the resolution and go beyond the diffraction limit, with the attribution of the Nobel prize in chemistry for super resolution microscopy in 2014.

Fluorescence is a phenomenon where emission of light occurs from the absorption of a photon (*Figure 15*). In their relaxed state, electrons of fluorophores are at the singlet ground state (S_0). When excited by light, energy from the photon is absorbed by the molecule and pushes an electron to a higher energy singlet state (S_1 , S_2) with higher vibrational energy. This transition is extremely fast, taking place in femtoseconds^{114,115}. The molecules then relax to the lowest vibrational energy of S_1 , this process is called internal conversion, taking around picoseconds. The molecule finally returns to the ground state of different vibrational levels in nanoseconds and emits a photon, referred to as fluorescence¹¹⁶. If the electron is not its lowest vibrational state, then vibrational relaxation takes place to bring the electron down to the ground state.

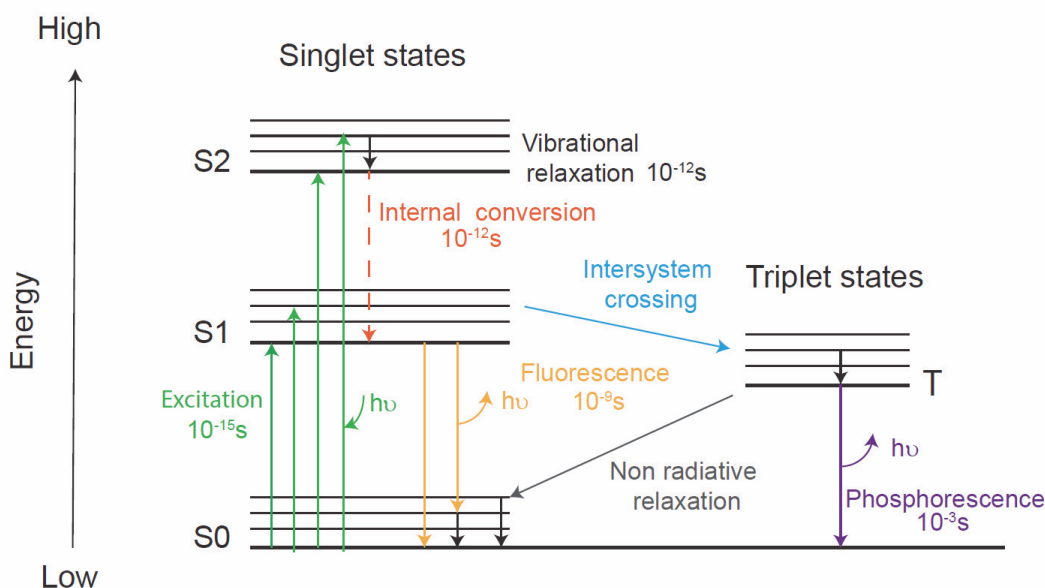


Figure 15. Jablonski Diagram. When a fluorophore is excited by a photon, an electron leaves the ground state (S_0) to a higher excited singlet state. It then relaxes down to the lowest vibrational level of S_1 by an internal conversion/vibrational relaxation process. By relaxing further to the ground state, energy is lost in the form of a photon with lower energy and longer wavelength (than the excitation photon), producing fluorescence.

The energy of fluorescence emission is between the lowest vibrational energy of S_1 and S_0 with vibrational energies ranging from 0 to higher. The fluorescence is therefore emitted with lower energy and a longer wavelength compared to the excited wavelength. The difference between the two wavelengths is called Stokes shift (*Figure 16B*). The absorption and emission transitions involve similar energetic levels, creating an emission spectrum with close symmetry image to the excitation spectrum. The excitation and emission spectra are broad (*Figure 16B*) this factor is important to take into account in microscopy since one excitation wavelength may excite different fluorophores. Another issue is that the emission spectra of fluorophores may overlap.

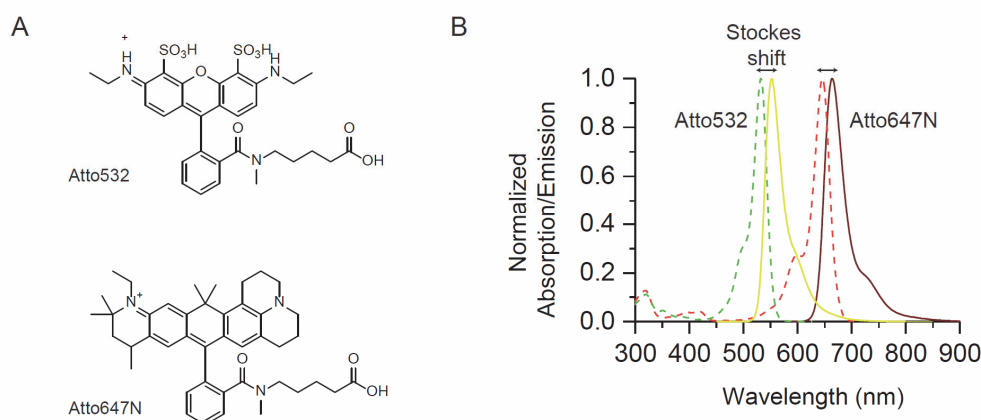


Figure 16. Absorption and Emission spectrum of fluorescent molecules. A) Structures of Atto532 and Atto647N B) Absorption and emission spectrum of Atto532 and Atto647N, the arrows represent Stokes shift.

The excited state can also go to the triplet state through intersystem crossing, a slower process where the electron changes spin (*Figure 15*)^{114,117}. This process is a spin forbidden process, however vibrational energy levels of the triplet state overlap with the lowest energy level in S_1 , which favours intersystem crossing and then internal conversion to the lowest vibrational energy of T leading to a lower number of emitted photons (blinking) and irreversible chemical reactions (bleaching). The forbidden relaxation from the triplet state to the ground state emits phosphorescence and can take up to milliseconds. Triplet state molecules can undergo photochemical reactions, causing irreversible bleaching to the dye and phototoxicity. Fluorophores in T_1 are active in electron transfer reactions with molecular oxygen forming superoxide radicals (O_2^-) and a radical non-fluorescent cationic state (R^+) or a non-fluorescent radical species (1O_2). Superoxide radicals and singlet oxygen species and other reactive oxygen species can further cause photobleaching and degradation of the fluorophore¹¹⁸. This is problematic in single molecule microscopy since individual fluorescent spots are imaged

overtime. It is imperative that fluorophores stay as stable as possible since blinking or bleaching can lead to the misinterpretation of measurements.

Different ways are used to obtain stable dyes. One simple way to reduce bleaching of the dyes is to degas all buffers to prevent reaction of the dye with oxygen species, however this is often not enough and an oxygen scavenging system must be added to the imaging buffer. An example of an oxygen scavenging system is the combination of glucose/glucose oxidase/catalase¹¹⁹ (Figure 17A). Molecular oxygen is reduced by catalytic oxidation of glucose by glucose oxidase to form hydrogen peroxide, a reactive oxygen species, which is then removed by catalase. However, the triplet state quenching by molecular oxygen is now removed and leads to the formation of radical states owing to the fluorophore transferring electrons to its surroundings. To counterbalance this, Trolox an analog of vitamin E, is added to the system to reduce the time the molecule is spent in the triplet state (Figure 17B). Trolox acts as a reductant and its degraded product, a quinone derivative, acts as an oxidant providing a pathway to depopulate the triplet state quickly to form radical cations or anions that are then oxidized or reduced respectively to the ground state¹²⁰.

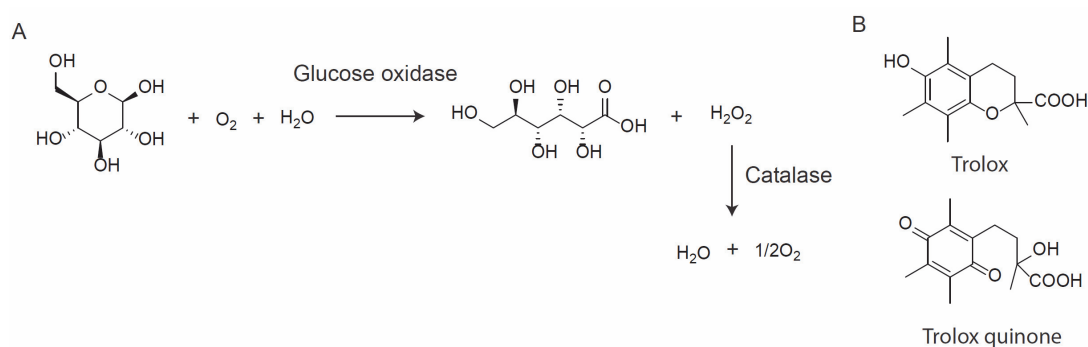


Figure 17. Oxygen scavenging system for fluorescence microscopy. A) Reaction of glucose oxidase/catalase to reduce oxygen in the single molecule system. B) Structure of trolox and its derivative, trolox quinone.

The fluorescence efficiency of a molecule is determined by the quantum yield, defined by the number of emitted photons relative to the number of absorbed photons, taking into account the rate of emission of a fluorophore and the rate of non-radiative decay¹¹⁵. Higher quantum yields mean that the fluorescence intensity is higher and that there are fewer side processes. The fluorescence lifetime is the average time the molecule spends in the lowest level S_1 before relaxing to the ground state. The fluorescence intensity can be decreased by various processes such as various non-radiative processes, quenching by surrounding molecules or resonance energy transfer (FRET) which has been exploited to determine conformational changes of proteins.

Two fluorophores are used, where the emission of the excited fluorophore overlaps with the absorption spectrum of the other. The energy can then be transferred from ‘donor’ dye to the ‘acceptor’ dye.

1.5.2. Fluorescent molecules

Fluorescent proteins are the most popular fluorescent labels for specifically labeling molecules in live cells. They are obtained by fusing the gene of the fluorescent protein to the gene encoding for the protein of choice. The most famous of these fluorescent proteins is GFP (green fluorescent protein), which was discovered in a species of jellyfish, *Aequorea Victoria*¹²¹. The chromophore consists of three amino acids; serine65, tyrosine66 and glycine67, forming a heterocyclic photoactive state¹²². Since the discovery of GFP, many different proteins have been engineered to provide excitation in the whole colour spectrum. Fluorescent proteins have relatively poor photophysics compared to organic dyes or quantum dots, they are less bright, absorb excitation light less efficiently, and are less photostable and so will photobleach after emitting fewer photons than typical equivalent organic dye molecules. Fluorescent proteins are also large (3 nm) and could lead to steric hindrance of the protein of interest.

Quantum dots are inorganic nanocrystals that emit strong fluorescence and emit different wavelengths depending on their size. Quantum dots are often coated with streptavidin or antibodies to allow their conjugation to a specific target. Their fluorescent intensities are 10-100 fold stronger than those of fluorescent proteins and small organic dyes and are extremely photostable but the main disadvantage is their very large size (10-30 nm).

Organic dyes are conjugated to proteins using chemical reactions such as cysteine chemistry, EPL, SNAP-Tag technology^{109,123,124}. The main advantage of organic dyes is their small size (<1 nm) that rarely perturbs the functionality of labeled proteins. They are also bright and more photostable than fluorescent proteins and their emission spectra are far red-shifted compared to fluorescent proteins, facilitating single-molecule imaging in live cells.

1.5.3. Wide-field microscopy

The simplest type of microscopy is wide-field microscopy, composed of a light source with an excitation filter to select for specific wavelength that is then used to excite fluorophores in the sample¹¹⁴. The emitting wavelength is passed through an emission filter to remove

wavelengths coming from the excitation light. The emitted light is then observed through an eyepiece or an image acquisition device such as a CCD camera. When the sample is excited, fluorescence is emitted in all directions. By introducing an objective with a wide angular opening (aperture) more of the deflected light can be captured to provide better resolution. The objective's light-capturing activity or numerical aperture (N.A.) depends on the refraction index of the medium used between the objective and coverslip (usually water or immersion oil) and half the objective opening angle (*Equation 3*).

$$NA = n \cdot \sin\alpha \quad (3)$$

The xy resolution in microscopy is the shortest distance where two fluorescent spots can be visually separated. It is dependent on the numerical aperture of the objective and the wavelength of the excitation light (*Equation 4*).

$$d = \frac{\lambda}{2 \cdot NA} = \frac{\lambda}{2 \cdot n \cdot \sin\alpha} \quad (4)$$

With high NA objectives of 1.14, a theoretical resolution of around 200 nm can be obtained. This means that when two fluorescent spots are closer than 200 nm, they will be observed as one fluorescent spot without discrimination, also known as the diffraction limit. In wide field microscopy the excitation light goes through the whole sample. For thin samples this is not an issue, however for thicker samples with a number of fluorescent molecules in the z axis, this can lead to very high background noise. This issue was solved by the design of confocal laser scanning microscopy¹²⁵ with the implementation of a pinhole to block out of focus light and only let the light from the focal plane pass through, thereby optically sectioning layers of the sample. The image is built up by scanning the sample and detecting point by point¹²⁶.

An interesting method employed to measure protein movement and dynamics in cells is Fluorescence Recovery After Photobleaching (FRAP)¹¹⁴. In this method, the labeled protein of interest is expressed in the cell. A laser beam is used to irreversibly bleach a small focused area. Overtime, the fluorescence of the bleached area is recovered from the fluorescent proteins diffusing in the cell. This recovery time is measured and gives information about the protein dynamics. Although this technique is extremely useful, it gives an average of the proteins and does not discriminate between individual proteins.

Single molecule techniques have been developed to study individual molecules *in vivo* or *in vitro*, to decipher intricate binding dynamic mechanisms of proteins, one of these methods is Total Internal Reflection Fluorescence Microscopy (TIRFM).

1.5.4. Single molecule total internal reflection fluorescence microscopy

Total internal reflection fluorescence microscopy (TIRFM) allows fluorescent molecules to be visualized with a high signal-to-noise ratio^{117,127}. It is achieved by only illuminating the molecules that are within a thin volume near the coverslip surface but not those deeper in the sample.

TIRFM involves a laser beam of wavelength λ directed at an angle of incidence θ to the interface between the glass coverslip of high refractive index n_1 and the water-based medium of lower refractive index, n_2 ¹²⁸. When the angle of incidence is at critical angle θ_c , the light will travel at the interface between the two interfaces (*Figure 18B*).

If the incident angle is higher than the critical angle, total internal reflection of the incident beam occurs, sending the beam back from the microscope coverslip away from the sample and only a short range evanescent field will pass into the low refractive medium (*Figure 18C*)^{117,127}.

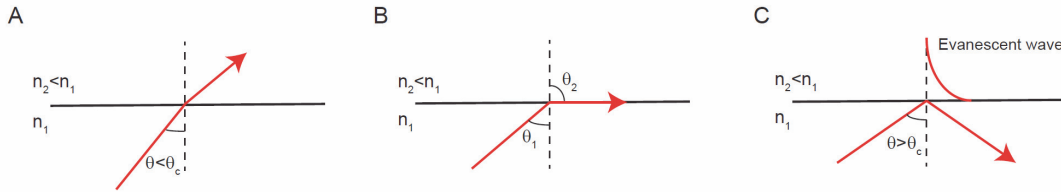


Figure 18. Influence of the incidence angle of the laser beam in TIRFM. A) The laser beam is directed to the coverslip at a lower angle than the critical angle and passes through the medium of refractive index $n_2 < n_1$. B) When the laser beam is at the critical angle, the refractive beam is at the interface between the medium and the glass. C) When the laser beam is at an angle higher than the critical angle, it is refracted away from the coverslip and creates an evanescent field into the sample.

The critical angle can be determined from Snell's law (*Equation 5*), which provides the relationship between the angles of incidence θ_1 and refraction θ_2 and the indices of refraction of the two media.

$$n_1 \sin \theta_1 = n_2 \sin \theta_2 \quad (5)$$

When the laser is reflected at 90° , along the media and the coverslip, the critical angle is given by *Equation 6*.

$$\theta_c = \sin^{-1} \frac{n_2}{n_1} \quad (6)$$

The refractive index of a glass coverslip and water is around 1.51 and 1.33 respectively, giving a critical angle of around 61° ¹²⁷. Oil immersion is used because its refractive index is similar to glass, reducing undesired reflections¹²⁷. The evanescent field into the water-based medium

with intensity $I(z)$ decays exponentially as a function of the vertical distance z from the glass-water interface (*Equation 7*).

$$I(z) = I_o \exp\left(-\frac{d}{z}\right) \quad (7)$$

Where the depth of penetration is defined by *Equation 8*.

$$d = \frac{\lambda}{4\pi} \frac{1}{\sqrt{n_1^2 \sin^2 \theta_1 - n_2^2}} \quad (8)$$

Typical values of the depth of penetration range between 50 to 200 nm. This means that only fluorophores very close to the coverslip are excited, whereas those in the surrounding medium are not. To exploit the excitation at the surface of the coverslip *in vitro*, the protein or DNA of interest is specifically tethered to the coverslip. Other fluorescent molecules not present in the evanescent field are not excited and therefore not observed, giving the advantage of low background noise (*Figure 19B*).

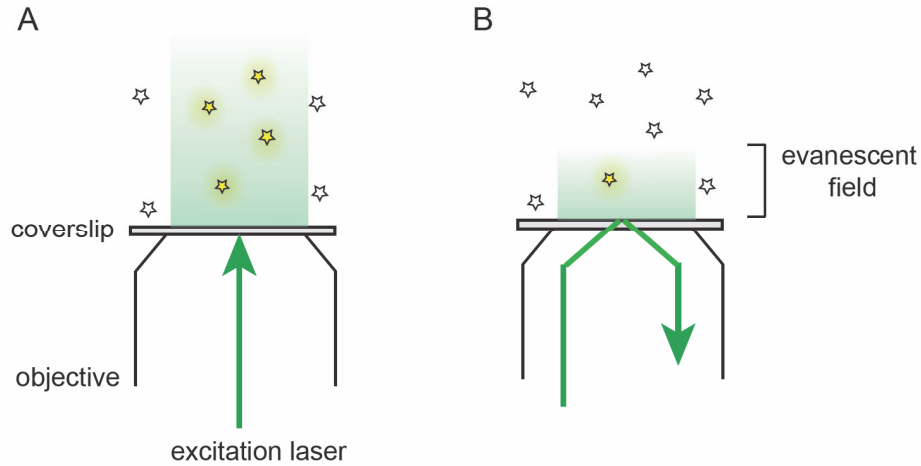


Figure 19. Wide-field vs total internal reflection fluorescence. *A) In wide-field microscopy, the laser excitation beam penetrates through the whole sample. B) In TIRFM the laser excitation beam is directed to the coverslip at an angle and reflects back. The sample at the surface of the coverslip is excited and leads to better signal to noise and enable single molecule measurements.*

Single molecule TIRM provides a method to determine dynamic interactions between proteins. This method can be used to determine the kinetic interactions between an effector protein and synthetic chromatin containing the modification(s) of interest. The chromatin fibers are tethered to the surface of the coverslip and the binding interactions of individual proteins can be determined by measuring their colocalization to each chromatin fiber.

2. Aims of the thesis

The aim of my thesis was to 1) decipher kinetic interactions of an effector protein, HP1 to synthetic chromatin containing H3K9me3 at the single molecule level, 2) determine the influence of chromatin state and HP1 subtypes on HP1 recruitment and 3) develop a single molecule readout of a barcoded library of DNA for protein multiplexing. These aims are developed in the following paragraphs:

1) Deciphering the kinetic interactions of HP1 to H3K9me3 chromatin

Despite the low (micromolar) affinity of HP1 for H3K9me3, these effector proteins are able to achieve efficient heterochromatin localization. To understand HP1 binding dynamics, I worked with Sinan Kilic, Andreas Bachmann and Prof. Beat Fierz to develop a single molecule TIRFM technique. This method would enable us to measure the colocalization of HP1 α to synthetic chromatin fibers containing H3K9me3. In this way we aimed to investigate three models: 1) The co-existence of many low-affinity binding sites leads to rapid re-binding of HP1 after dissociation. 2) The ability of HP1 α to oligomerize on the chromatin fiber, resulting in the formation of stable and long-lived complexes. 3) HP1 increases its affinity upon dimerization.

2) Investigating the influence of chromatin state and HP1 isoforms on HP1 recruitment

In this second part, I continued working on HP1 to further improve our understanding on its recruitment to chromatin. Since chromatin is extremely dynamic in the nucleus we were interested to study the influence of chromatin state over HP1 α binding, either by creating condensed chromatin by the incorporation of Histone H1.1 or by increasing the linker length and addition of a histone PTM, H4K16ac that has been shown to open chromatin fibers. We were also intrigued by the fact that the HP1 family has three different isoforms, which localize to different areas of the cell. I therefore measured the interaction of the three different HP1 isoforms as well as phosphorylated HP1 α to H3K9me3 synthetic chromatin.

Using these single molecule results and in collaboration with Daniel Weilandt and Prof. Vassily Hatzimanikatis we were able to produce a kinetic model of HP1 recruitment to chromatin.

3) Single molecule readout of a barcoded library of DNA for protein multiplexing

The final aim of my thesis was to develop a method where a barcoded library of nucleosomes that can be read-out by single molecule TIRFM. Up to this point, the single molecule set-up in our lab enables the discrimination of a protein binding to one type of modified nucleosome per

channel due to the spectral limitation of dyes. We aimed to improve our system to provide an experimental set up where the protein binding dynamics to a library of nucleosomes are measured. To this end I aimed to develop a method to read-out the barcodes on the nucleosome library which relies on the dynamic hybridization of short ssDNA pieces to their complementary sequence on nucleosomal DNA.

In conclusion, the aim of my thesis was to develop a single molecule TIRF system that would enable us to determine the interaction dynamics of effector proteins to chromatin. This is a valuable technique that helps to shed light on the intricate regulation of chromatin. The third project was focused towards improving our system to enable us to probe more complex systems, where chromatin-binding proteins bind differently depending on the combination of histone marks.

3. HP1 α -chromatin binding at the single molecule level

This chapter is based on the following research articles:

Multivalency governs HP1 α association dynamics with the silent chromatin state. Sinan Kilic, Andreas L. Bachmann, Louise C. Bryan and Beat Fierz. Nature communications. 2015

Single molecule kinetic analysis of HP1 chromatin binding reveals a dynamic network of histone modification and DNA interactions. Louise C. Bryan, Daniel R. Weilandt, Andreas L. Bachmann, Sinan Kilic, Carolin Lechner, Pascal D. Odermatt, Georg E. Fantner, Sandrine Georgeon, Oliver Hantschel, Vassily Hatzimanikatis and Beat Fierz. Nucleic Acids research. 2017

Contribution by other members is indicated in the text and in figure legends.

3.1. Background and overview

Heterochromatin protein 1 is an effector protein, composed of a chromodomain that interacts with micromolar affinity to H3K9me3, a chromo shadow domain that enables monomers to dimerize and an unstructured hinge region that links these two domains^{54,55,67,73}. Three different isoforms are found in humans, HP1 α , HP1 β and HP1 γ ^{55,57}. In living cells, methods such as fluorescence recovery after photobleaching (FRAP) and fluorescence correlation spectroscopy (FCS) have been used to gain insight into the kinetic interactions of HP1 and chromatin^{76,77}. These studies show that HP1 is not stably bound to pericentric heterochromatin but is highly mobile in a stable compartment (or domain) that is actively renewed^{76,77}. Although these results have been helpful to understand the binding dynamics of HP1, the determination of kinetic parameters from FRAP or FCS requires the application of mathematical models, which can lead to misinterpretations of the kinetics. Many factors such as the density and the presence of different marks lead to complicated mechanistic interpretation therefore a single molecule method in a controlled system would be preferable to shed light on these kinetic events.

The general aim of this project was to use a single molecule microscopy method to study the binding of HP1 towards chemically synthesized chromatin fibers to understand how HP1,

which has low affinity towards H3K9me3, is able to increase its affinity and localization to chromatin.

Initially, we aimed to study three main models that have been proposed to explain how HP1, despite its low affinity to H3K9me3 can localize to heterochromatin. I studied the first model whereas the other two models were studied by Andreas Bachmann and Sinan Kilic, however their results will also be included in this thesis since they were important for the experiments that followed.

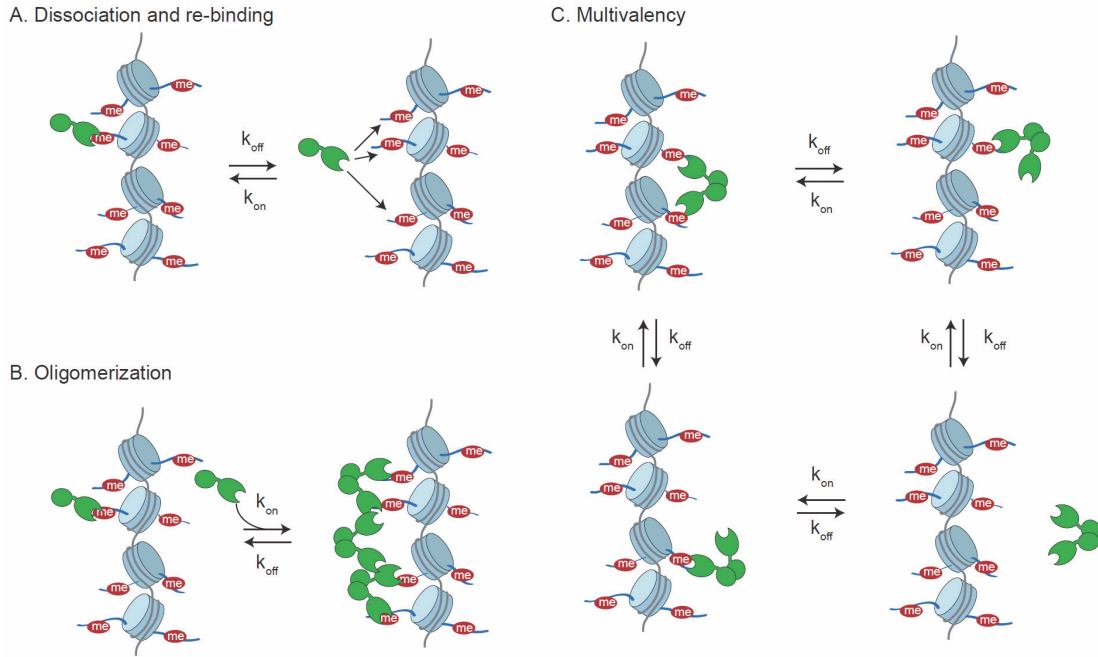


Figure 20. Schematic representation of the three models explaining the retention of HP1 towards H3K9me3-modified chromatin. A) Model I: HP1 rebinds rapidly to the same mark or to a neighbouring mark after dissociation. B) Model II. HP1 forms oligomers along the chromatin or C) Model III. HP1 dimerization increases the likelihood of binding.

The first model (Figure 20A) suggests that the co-existence of many low-affinity binding sites in chromatin fibers allows rapid re-binding of HP1 after dissociation. To study this model, we aimed to probe the interaction of HP1 α towards chromatin containing varying amounts of H3K9me3. A decreased number of marks on the chromatin fiber would potentially lead to lower chances for the protein to re-bind after unbinding.

The second model (Figure 20B) suggests that stable and long-lived complexes are the result of HP1 oligomerization on the chromatin fiber. To study this model, the concentration of HP1 α was increased (1 nM HP1 is used in standard single molecule measurements) to facilitate the potential formation of oligomers.

Finally, the multivalent binding interactions of dimeric HP1 increases binding affinity towards chromatin (*Figure 20C*). This model was studied by comparing HP1 α to a synthetic covalently dimerized HP1 α .

3.2. Results & Discussion

3.2.1. Preparation of HP1 and chromatin

Histone octamers

The first step was to prepare synthetic chromatin. Individual histone proteins were recombinantly expressed and purified, however the trimethylated H3K9 histone was prepared semi-synthetically, by ligating the truncated protein H3(Δ 1-14)A15C to the N-terminal peptide tail containing the trimethylated lysine, H3K9me3(1-14) (*Figure 21A*). The hydrazide at the C-terminal peptide was oxidized by addition of NaNO₂ at pH 3, followed by the formation of an *in situ* thioester by the addition of MPAA. The peptide was then ligated to the truncated protein by NCL. After purification by RP-HPLC and lyophilisation, the semi-synthetic protein was desulfurized using a radical-initiated reaction and purified by RP-HPLC to obtain an alanine instead of cysteine at the ligation junction (*Figure 5B and C*).

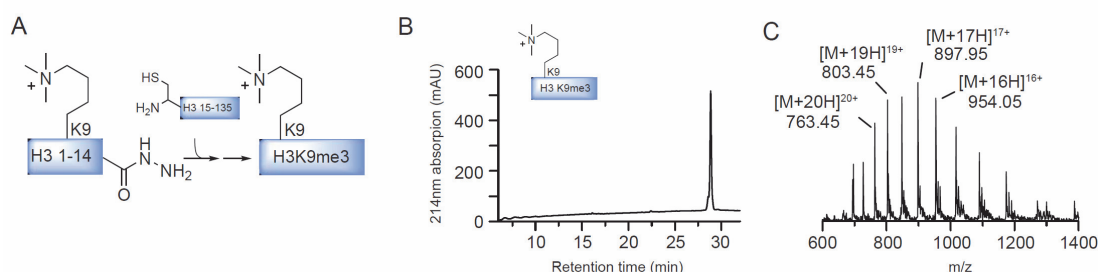


Figure 21. Synthesis of H3K9me3. A) Synthesis scheme of H3K9me3 using a traceless EPL approach. B) Analytical RP-HPLC and C) ESI-MS analysis of the ligation product H3K9me3 after desulfurization (calculated mass: 15251 Da, observed mass: 15248 Da). The peptide was provided by Sinan Kilic and the truncated histone by Carolin Lechner.

Once all the protein histones H2A, H2B, H3K9me3 and H4 were prepared, histone octamers could be assembled. The four different histone proteins were dissolved in unfolding buffer containing guanidine and mixed at equimolar ratio (with a 10 % excess of H2A and H2B). To refold the histones into octamers the mixture was dialyzed against refolding buffer containing a high concentration of salt. The refolded histone octamers were then purified from dimers and tetramers by size exclusion chromatography (*Figure 22A*). Eluted histone octamers were

concentrated (*Figure 22B*) to $\sim 60 \mu\text{M}$, supplemented with glycerol to 50 % and stored at -20°C .

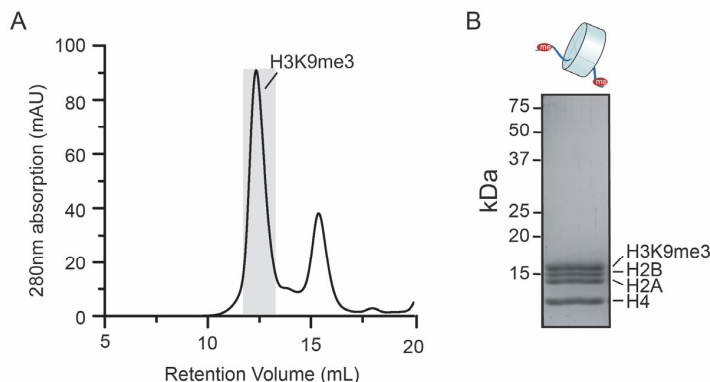


Figure 22. H3K9me3 histone octamer refolding. *A) Refolded histone octamers containing H3K9me3 were purified by size exclusion chromatography. B) SDS-PAGE analysis of the refolded octamers pooled and concentrated after size exclusion chromatography.*

12x 177bp DNA

In parallel to preparing histone octamers, the labeled and biotinylated chromatin DNA (*Figure 23A*) was produced. To prepare the DNA, a plasmid containing 12 repeats of 601 nucleosome positioning sequence (NPS)¹²⁹ separated by 30 bp of linker DNA segments. Each linker DNA contained a ScaI restriction site that enables cleavage between each nucleosome to check for correct formation of chromatin fibers by gel electrophoresis. A unique BsaI restriction site was also added at the 3' end for the ligation of the DNA piece to a labeled anchor. The plasmid was generated recombinantly and purified by size-exclusion chromatography¹³⁰. The chromatin DNA was then released from the vector backbone by EcoRV digestion and purified by PEG precipitation. To obtain a labeled DNA array, it was then digested with BsaI for ligation to a short anchor. This anchor was prepared in the following way: a synthetic oligonucleotide containing an internal amine attached to a dT and a C-terminal biotin, was labeled with Atto647N-NHS ester (5'-ph-CAGCTAGTCTGCT-(amine-linker)-CAGATATCGTCG-Biotin-3'). The labeled ssDNA was then annealed to its complementary strand (*Figure 23A*). Once the 12x '601' array DNA was ligated to a short anchor, the excess anchor was removed by purification with QIAquick spin columns (*Figure 23B*). DNA for mononucleosomes, used in control experiments, was prepared using the same methodology, but a 1x 601 NPS sequence was used.

3. HP1 α -chromatin binding at the single molecule level

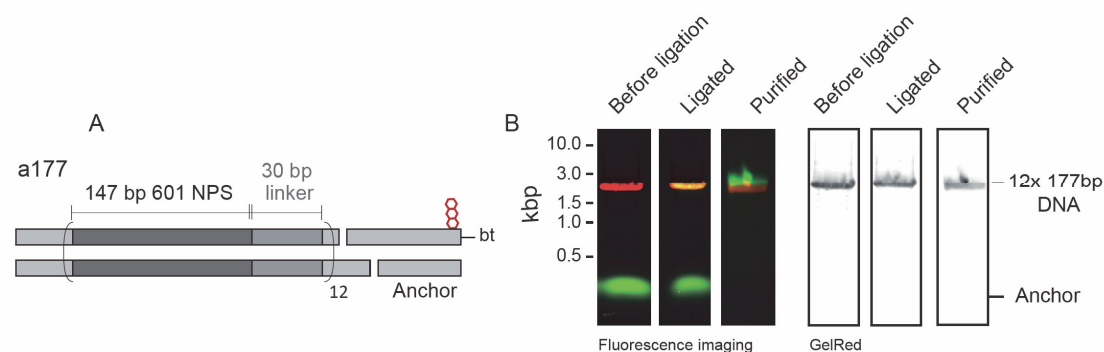


Figure 23. Preparation of 12x 177bp labeled chromatin DNA. A) Schematic representation of the 12x 147bp NPS with 30 bp linker DNA. B) Production of fluorescently labeled and biotinylated 12x 177bp DNA. In the fluorescence overlay, red: GelRed, green: Atto647N.

Chromatin reconstitution

Chromatin arrays were reconstituted at a concentration of around 1 μ M per mononucleosome (100 pmol). Chromatin DNA was mixed with 1 equivalent (per 601 site) of histone octamers (different amounts of H3K9me3 octamers were mixed with unmodified octamers, *Figure 24 A and B*) in reconstitution buffer with low salt concentration (10 mM KCl). 0.5 molar equivalents of low affinity NPS site sequence (MMTV buffer DNA) which is around 150 bp, was added to prevent oversaturation of the array DNA. The reactions were gradually dialyzed from high salt buffer containing 2 M KCl, to reconstitution buffer over 12 hours with a two-channel peristaltic pump. After dialysis, the reconstituted chromatin arrays were analysed on a 0.6% agarose gel (*Figure 24A*) or non-denaturing 5% polyacrylamide gel electrophoresis (PAGE) in 0.5x Tris-Borate-EDTA (TBE) running buffer following *ScaI* restriction digest, which cuts between each nucleosome (*Figure 24B*).

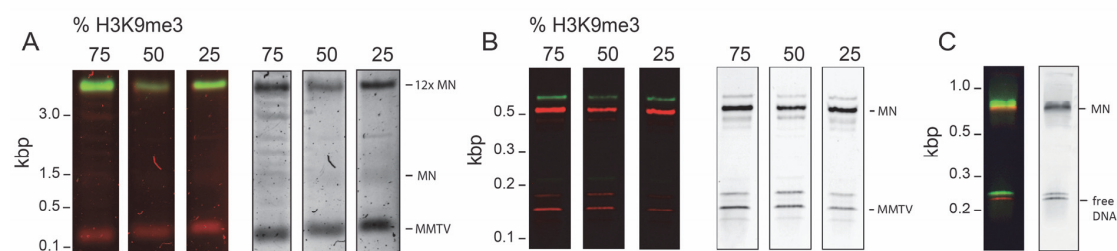


Figure 24 Reconstituted chromatin with different degrees of H3K9me3 octamers. A) Agarose gel analysis of reconstituted 75%, 50% or 25% H3K9me3 labeled chromatin arrays with a177 DNA. Green: Atto647N, red: GelRed. B) Native PAGE analysis of *ScaI* digested 75%, 50% or 25% H3K9me3 labeled chromatin arrays with a177 DNA. Green: Atto647N, red: GelRed. C) Native PAGE analysis of mononucleosomes with H3K9me3 and Atto647N-labeled 1x 601 DNA. Green: Atto647N, red: GelRed.

The octamers preferably refold with the 601 Widom sequence compared to MMTV DNA. By running these two gels, we can make sure the chromatin is reconstituted properly, on one hand

there is still a small band corresponding to free MMTV DNA and a light band corresponding to mononucleosomes with MMTV DNA, which means that the 12x 177bp DNA was saturated enough with octamers to start forming nucleosomes with MMTV DNA.

Mononucleosomes with H3K9me3 octamers were formed in the same way, without addition of MMTV DNA (Figure 24C).

HP1 α -Atto532

For smTIRF experiments, HP1 was labeled with Atto532, this enable us to discriminate between the A647N-labeled chromatin which is excited with the 640 nm laser with its fluorescence emission detected in the far red channel and the protein which is excited with the 530 nm laser with its fluorescence emission detected in the yellow/orange channel. Since HP1 already contains several cysteines we could not use simple cysteine chemistry to label the protein. Therefore, to minimize the risk of structurally perturbing the protein, an EPL-based approach was used to label the protein at its C-terminal. The idea was to convert the recombinant HP1 fused to the N-terminal part of the *N. punctiforme* (Npu) split-intein into a C-terminal thioester¹⁰⁹ and then ligate it to a tripeptide carrying an Atto532 fluorophore (Figure 26A). First of all, the C-terminal cysteine of the purified tripeptide (Thiozolidine-G₂-C₃-CONH₂), synthesized by SPPS, was reacted with Atto532-iodoacetamide, followed by quenching of the reaction by TCEP. Thiazolidine opening was achieved by treatment with 0.5 M methoxylamine at pH 5 (Figure 25A). The labeled tripeptide was purified by semipreparative RP-HPLC and lyophilised.

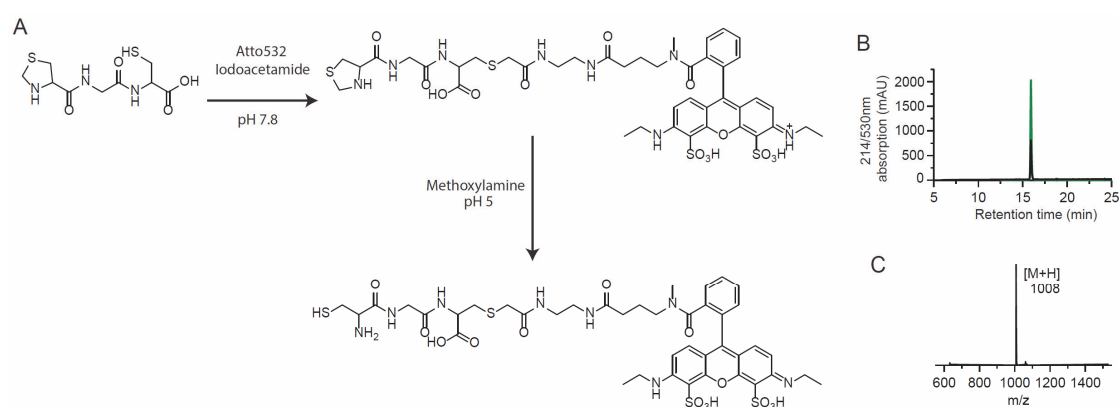


Figure 25. Labeling strategy for the CGC peptide. A) The thiozolidine-CGC peptide is coupled to Atto532 iodoacetamide in solution followed by opening of the thiazolidine using 0.5 M methoxylamine at pH 5. B) RP-HPLC (black curve: 214 nm and green curve: 530 nm) and C) ESI-MS of the product (expected mass: 1009 Da, observed mass: 1008 Da). The tripeptide was synthesized by Beat Fierz.

3. HP1 α -chromatin binding at the single molecule level

HP1 α , fused to the NpuN split-intein sequence¹⁰⁹ at its C-terminus, followed by a hexahistidine tag was expressed in *E. coli* by IPTG induction. Proteins were purified over a Ni-affinity resin column, followed by anion exchange chromatography to remove DNA. The HP1 α -Npu^N fusion construct at a concentration of 50–100 μ M was applied to a column of 125 μ l SulfoLink resin slurry, containing the immobilized Npu^C peptide (Figure 26A). The two split inteins come together to release the protein and addition of MESNA leads to the formation of a thioester. The labeled tripeptide, added with MPAA to the column, was ligated to the protein. Eluted fractions were pooled (Figure 26B) and the protein was purified by size exclusion chromatography (Figure 26C).

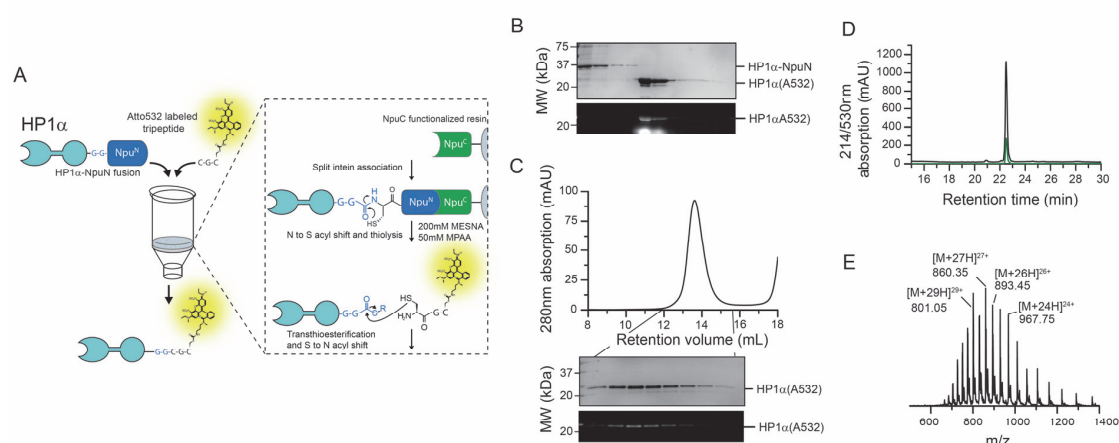


Figure 26. HP1 α labeling. A) Schematic representation of the procedure to fluorescently label HP1 α using split-intein mediated EPL. B) SDS-PAGE analysis before and after HP1 α labeling. C) Purification of HP1 α -A532 by size exclusion chromatography. D) RP-HPLC (black curve: 214 nm and green curve: 530 nm) of HP1 α -A532. E) MS of HP1 α -A532 (HP1 α : calculated mass: 23200 Da, observed mass: 23202 Da).

3.2.2. Single molecule microscopy

Coverslip preparation

Having all necessary components in hand, we then proceeded to measure HP1 α -chromatin interaction dynamics using smTIRFM. However, an essential step for single molecule microscopy experiments was the preparation of microscopy slides. If the cleaning or the passivation was not done properly, fluorescent spots could be present during measurements or the labeled protein of interest could bind unspecifically to the unpassivated surface areas and lead to inconclusive experiments. Different methods were tested; the slides were either cleaned by plasma cleaning or piranha cleaning (Figure 27B and Figure 28). In the case of oxygen plasma cleaning, surface contaminants are broken down and react with oxygen species created

3. HP1 α -chromatin binding at the single molecule level

in the plasma and are evacuated from the chamber with a pump, resulting in a clean surface. In the case of the piranha solution, the slides and coverslips are immersed in a mixture of concentrated H₂SO₄ and 30% H₂O₂ with a ratio of 3:1, leading to a highly corrosive and strong oxidizing solution to remove any trace of organic contaminants and providing a hydroxyl terminated surface (*Figure 27B*).

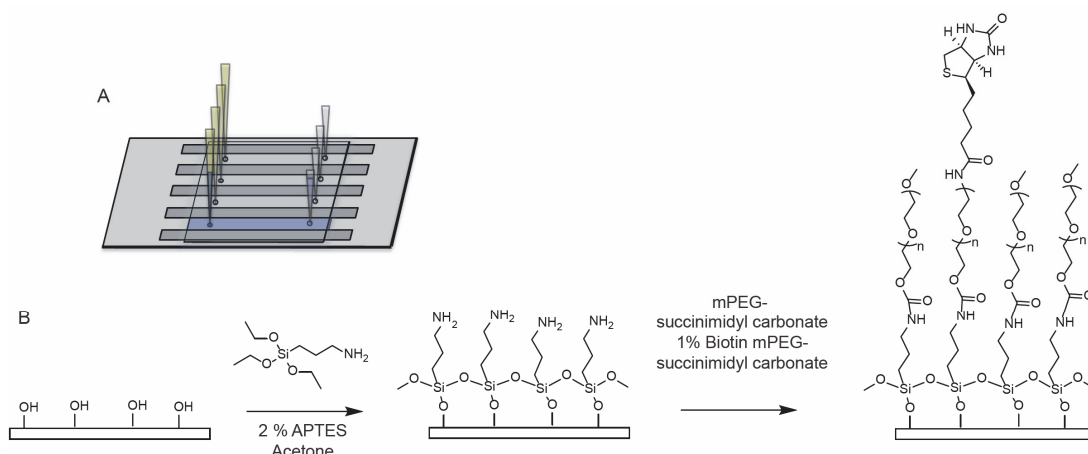


Figure 27. Preparation of microscopy glass coverslips. A) Schematic representation of the microscopy coverslip. The coverslip is glued to a slide with double-sided tape to form four channels. Tips were glued to each end of the channels to enable the injection of samples. B) Surface passivation of the glass. First the glass was cleaned to provide a hydroxyl surface. Then it was reacted with 2% APTES in acetone and finally mPEG-succinimidyl was bound covalently to the APTES to form a polymer brush.

The passivation was carried out with either PLL-g-PEG (Poly(L-Lysine)-grafted-poly(ethylene glycol)) which electrostatically interacts through the PLL backbone to the glass surface to form a densely packed polymeric brush or by silanizing the glass surface with 2 % (3-aminopropyl)triethoxysilane (APTES) in acetone creating a polymerized mono-layer covalently bound to the glass surface by forming bonds between neighbouring silanols (*Figure 27B*). This was followed by a PEGylation step where the succinimidyl carbonate on the PEG reacts with the amine of the silanized surface. In order to check the surface, the labeled protein was injected into the channels and imaged in the yellow/orange channel with excitation from the 530 nm laser in TIRFM. From the images taken for each condition (*Figure 28A-E*), the nicest passivation was observed with the slides cleaned by piranha etching, followed by silanization and PEGylation. After the silanization step, the slides and coverslips were dried and assembled into flow cells, containing four channels each separated by double-sided adhesive tape (*Figure 27A*) and kept in the -20°C freezer under vacuum until further use.

Before an experiment, the assembled slides were thawed and pipette tips were inserted into the drilled holes and sealed with epoxy glue to provide channels that can be easily filled and washed

out. The APTES layer provides free amino groups that are then reacted with mPEG(5000)-succinimidyl carbonate, with 1% biotin-mPEG(5000)-succinimidyl carbonate to provide a PEGylated surface (*Figure 27B*). After PEGylation, the channels were extensively washed before proceeding to experiments.

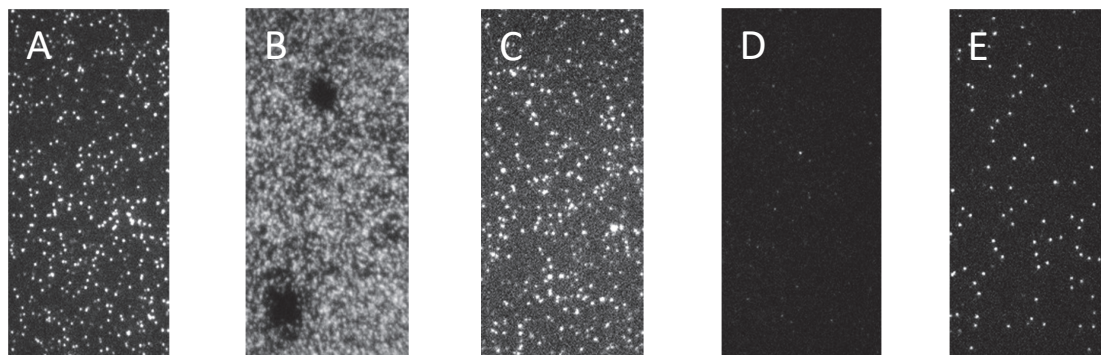


Figure 28. Different methods to passivate glass coverslips. 25 x 50 μm area of A) Plasma cleaned and 10 % PLL-PEG, 1 nM HP1 B) Plasma cleaned, silanized and PEGylated for 24 hours, 1 nM HP1, C) Plasma cleaned, silanized and PEGylated for 3 hours, 1 nM HP1 D) Piranha cleaned, silanized and PEGylated for 3 hours, 1 nM HP1 E) 250 pM chromatin binding to neutravidin after passivation observed in D).

Experimental procedure

For chromatin immobilization, a neutravidin solution at 0.2 mg/ml was infused using a high-precision syringe pump and incubated for 5 min, followed by extensive washes. Then, 500 pM chromatin arrays were injected into the neutravidin treated flow chamber for 5 min and then washed out. Chromatin coverage was observed in TIRF microscopy by fluorescent emission in the far-red channel upon excitation by a 640 nm laser line (*Figure 29A*). Dynamic binding experiments were initiated by infusion of Atto532-labelled HP1 α in imaging buffer. In order to measure HP1 α dynamics, the 532 nm laser line was used for excitation and the emission observed in the yellow/orange channel (*Figure 29A*) with an EMCCD camera at 20 frames/s over an area of 25 x 50 μm with a resolution of 160 nm/pixels. Every 200 frames, an image of the chromatin positions in the far-red channel was recorded to correct for drift correction.

Data analysis

The movies of HP1 α -chromatin interactions were then analysed. First of all, the movies were converted into TIF format and the first 200 frames were removed in ImageJ to get rid of the first frames where there is a higher background level. A semi-automated Matlab script written by Prof. Beat Fierz was then used to make a global baseline-correction and drift-correction. Individual chromatin array positions were determined using a peak-finding

3. HP1 α -chromatin binding at the single molecule level

algorithm from the far-red images. Fluorescence intensity traces for each chromatin position were obtained by integrating over a circle of 2 pixel radius (=320 nm) (*Figure 29B*). Individual HP1 fluorescence peaks were included based on point-spread-function (PSF) and distance cut-offs.

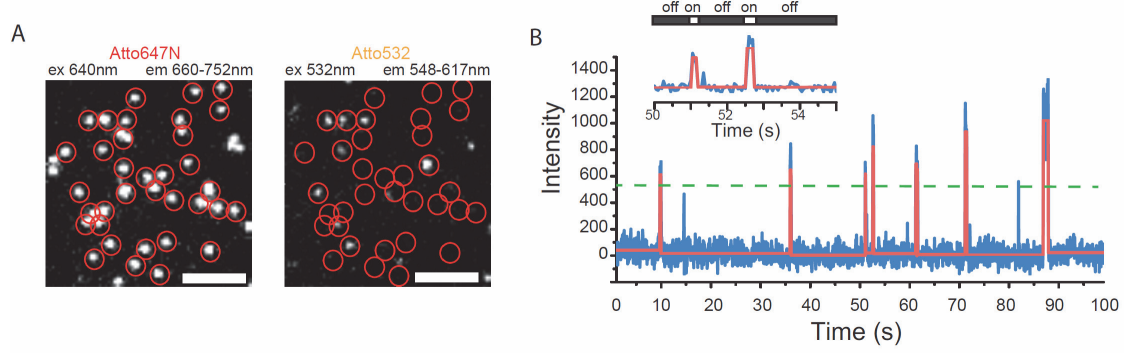


Figure 29. Single molecule colocalization of HP1 to chromatin. *A) Left: single chromatin arrays were detected by Atto647N emission. Right: HP1 α interaction dynamics were monitored by Atto532 emission. Scale bar: 5 μ m. B) Time trace of fluorescence intensity (blue) from a single chromatin array showing transient HP1 α binding events, fitted by a step function (red). Inset: determination of bound (on-) and unbound (off-) times by a thresholding algorithm.*

Kinetics were extracted from fluorescence traces using a semi-automated thresholding algorithm. Cumulative histograms were constructed from dark and bright intervals and fitted to sums of mono or bi-exponential functions. The cumulative histograms for HP1 dwell times were generally fitted with a double-exponential function (*Equation 9*). Where $\tau_{1,off}$ corresponds to the short binding events and $\tau_{2,off}$ corresponds to the long binding events with their respective amplitudes A_1 and A_2 .

$$Counts = A_1 e^{-\frac{t}{\tau_{off,1}}} + A_2 e^{-\frac{t}{\tau_{off,2}}} \quad (9)$$

The dissociation rate constant was then determined from the inverse of the binding time (*Equation 10*).

$$k_{off} = \frac{1}{\tau_{off,1}} \quad (10)$$

The cumulative histogram for times between binding events were fitted with a mono-exponential function (*Equation 11*).

$$Counts = A_1 e^{-\frac{t}{\lambda_{on}}} \quad (11)$$

The association rate constant was determined by the inverse of λ_{on} multiplied by the concentration of HP1 in the experiment and the number of nucleosomes on the chromatin fiber (*Equation 12*).

$$k_{on} = \frac{1}{\lambda_{on} \cdot c_{HP1} \cdot n_{br \text{ of nucleosomes}}} \quad (12)$$

Finally, the dissociation constant per nucleosome is given by *Equation 13*.

$$K_D = \frac{k_{off}}{k_{on}} \quad (13)$$

3.2.3. HP1 α binding to 12x 177a H3K9me3 chromatin

The first experiment in smTIRFM, which will be used as a reference for all the following experiments, was to measure the dynamic binding of 1 nM HP1 α -A532 towards H3K9me3 chromatin. A kinetic analysis of the resulting dwell-time histograms revealed double-exponential dissociation kinetics, with a fast major phase decaying with a time constant of $\tau_{off,1} = 0.25 \pm 0.03$ s (\pm s.d.) and a slower process with $\tau_{off,2} = 2.30 \pm 0.88$ s (*Figure 30B and E, Table 1*). These time constants are comparable to HP1 α dwell times observed in living cells⁷⁷. Furthermore, the observed dwell times were not limited by fluorophore photobleaching, as HP1 α -Atto532 decayed with a time constant >40 s under typical imaging conditions⁹⁸. Conversely, analysing the time intervals between binding events yielded an apparent association time constant of $\lambda_{on} = 22.9 \pm 9.8$ s (*Table 1*). From λ_{on} (taking into account the HP1 α concentration and the number of nucleosomes per array) a microscopic association rate constant of $k_{on} = 3.58 \times 10^6 \text{ M}^{-1}\text{s}^{-1}$ was determined, resulting in an apparent K_D of 1.1 μM for individual nucleosomes in an array (*Table 1*). This association rate constant is within the expected range of 10^5 - $10^6 \text{ M}^{-1}\text{s}^{-1}$ for diffusion-controlled binding reactions of proteins¹³¹. The experiment was repeated using unmodified (H3K9me0) chromatin arrays (measured by Andreas Bachmann). In the absence of the mark, HP1 α binding was almost completely abolished (*Figure 30D*), and the few binding events decayed with fast kinetics. Having established a system that allows the quantitative determination of the HP1 α interaction kinetics with modified chromatin arrays, we proceeded to test different models of interaction.

Model I: HP1 α undergoes rapid dissociation and rebinding

To assess the possibility that HP1 α undergoes a series of dynamic microdissociation and rebinding events, I investigated the kinetic effect of reducing the number of available binding sites with the hypothesis that if there are fewer trimethylated H3K9 marks on chromatin, HP1 will more like diffuse away than rebind to the chromatin fiber. The stochastic binding dynamics of HP1 α to chromatin arrays containing different fractions of trimethylated H3K9 (25%, 50% 75% and 100%, *Figure 24A-B*) was measured (*Figure 30D, Table 1*). The

3. HP1 α -chromatin binding at the single molecule level

residence time decreased from 0.25 s to 0.19 s from fully methylated chromatin to 75 % methylated chromatin. The residence time decreased even further with lower methylation density, indicating that when the effector protein dissociates from a mark it can rapidly rebind to a neighbouring mark if it is in close proximity to the first mark. However, if the neighbouring mark is too far away as displayed by lower degrees of methylated chromatin, HP1 will not reach the capture radius of this binding site and will diffuse away. This hypothesis was confirmed by measuring the interaction of HP1 to H3K9me3 mononucleosomes, without the presence of a “neighbouring H3K9me3 nucleosome”. This control also resulted in faster dissociation kinetics with a residence time of 0.13 s (Figure 30E, Table 1). These results indicate that rapid dissociation and rebinding events indeed contribute to the apparent residence time observed in densely modified chromatin.

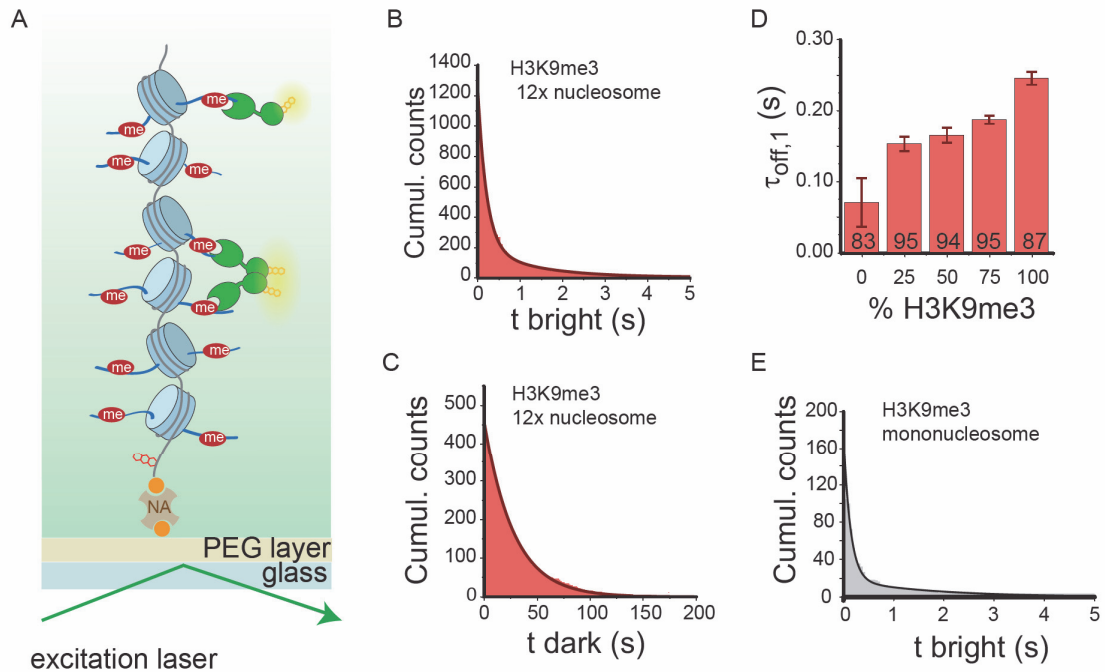


Figure 30. HP1 α binding to H3K9me3 chromatin. A) Schematic representation of a smTIRF experiment with 1 nM Atto532 labeled HP1 and H3K9me3 chromatin bound to the surface of the coverslip through a neutravidin-biotin interaction. B) Dissociation kinetics: cumulative histogram of binding intervals (t_{bright}) for 100 chromatin arrays, fitted by a double-exponential function. C) Association kinetics: cumulative histogram of intervals between binding events (t_{dark}) over 30 chromatin arrays, fitted by a single-exponential function. D) The HP1 α residence time ($\tau_{off,1}$) depends on H3K9me3 density. Numbers indicate % amplitude of the fast phase (errors: s.e.m.; $n = 2-16$ replicates). E) Dissociation kinetics: cumulative histogram of binding intervals for HP1 α binding to H3K9me3 mononucleosomes.

Model II: HP1 α molecules compete for H3K9me3 sites

The ability of HP1 α to oligomerize along the chromatin fiber was studied. Such a model for propagation of heterochromatin has been proposed for the yeast homologue Swi6^{67,132}. Under our standard measurement conditions (1 nM HP1 α), the chromatin fibres are only occupied by single HP1 α monomers or dimers, thus rendering the formation of larger oligomers impossible. To increase HP1 α occupancy by providing the potential for the protein to oligomerize, Andreas Bachmann performed experiments where the total protein concentration in the flow cell was increased by the addition of unlabelled HP1 α . This resulted in a concentration-dependent decrease of 0.25 s for 1 nM HP1 α to 0.13 s at 1 mM total HP1 α concentration (*Table 1*). This indicates that HP1 α does not form higher-oligomeric complexes, but increases the dynamic behaviour of HP1, where individual proteins compete for binding sites. This local competition then prevents rapid rebinding of dissociated HP1 α molecules, resulting in an apparent decrease in residence time, in a process known as facilitated dissociation^{133,134}. Such concentration-dependent dissociation kinetics were also observed for several other DNA-binding proteins such as DNA polymerases^{135,136}.

Model III: Multivalent chromatin interactions accelerate HP1 α binding

The influence of multivalent chromatin interactions on HP1 α recruitment was explored. K_D values of 0.5–5 μ M have been reported for CSD homodimerization of different HP1 subtypes¹³⁷. Therefore, under single-molecule conditions (at 1 nM concentration) a large fraction of HP1 α dimers is dissociated into monomers. To measure the dynamic interaction of dimeric HP1 α , the protein was constrained into a dimeric state by covalently ligating two HP1 α proteins with a shugoshin PxVxI-containing peptide (hSgoL1, residues 448–457). hSgoL1 plays a role in the protection of centromeric sister-chromatids and interacts with HP1, both in cell division and interphase with different functions^{138,139}.

At a concentration of 0.5 nM HP1 α cdm (equivalent to 1 nM HP1 α monomers), binding events of longer average duration and of increased frequency compared with HP1 α were observed. Residence times of $\tau_{\text{off},1} = 0.33 \pm 0.01$ s (87 % amplitude) and $\tau_{\text{off},2} = 3.40 \pm 0.53$ s (13 % amplitude) were measured with single-exponential binding kinetics of $\lambda_{\text{on}} = 7.45 \pm 1.87$ s (*Figure 31, Table 1*). Importantly, the dimeric HP1 α cdm also exhibited significantly more rapid chromatin binding, with $k_{\text{on}} = (2.24 \pm 0.60) \times 10^7 \text{ M}^{-1}\text{s}^{-1}$ (*Table 1*). This corresponds to a six-fold increase in the association rate constant for HP1 α cdm compared with HP1 α , and results in an apparent K_D of 0.14 μ M, about 60-fold increased affinity compared with isolated H3

peptides⁹⁸. In conclusion, HP1 α dimerization directly results in a significant increase in chromatin residence time. This effect can be attributed to the increased possibility of simultaneous engagement of two K9me3-bearing H3-tails in the chromatin array, the inability of dimers dissociating into monomers, as well as an increased chance of rebinding upon transient dissociation for HP1 α cdm.

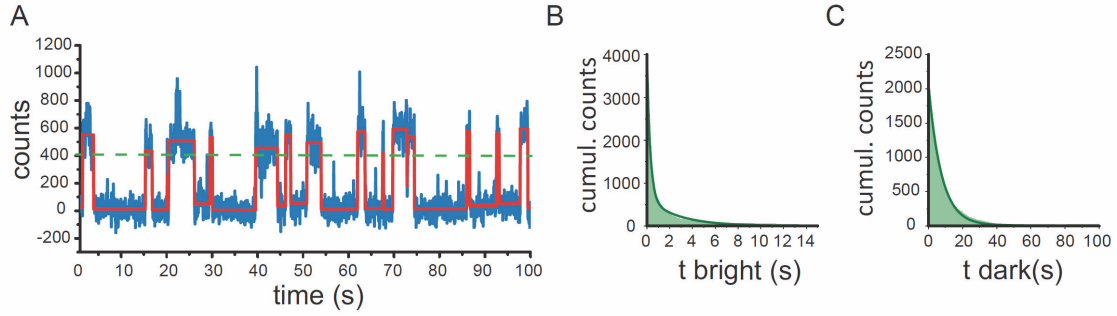


Figure 31. Constrained dimeric HP1 α binding to H3K9me3 chromatin. *A)* Time trace of fluorescence (blue) from a single chromatin array fitted by a step function (red) and showing transient HP1 α cdm binding events. *B)* HP1 α cdm dissociation kinetics fitted with a double exponential function ($\tau_{off,1} = 0.33 \pm 0.01$ s, $\tau_{off,2} = 3.40 \pm 0.53$ s). *C)* HP1 α cdm dissociation kinetics fitted by a single-exponential function ($\lambda_{on} = 7.45 \pm 1.87$ s). Data produced and analysed by Sinan Kilic and Andreas Bachmann.

3.3. Conclusion

We have developed a single molecule method to determine the binding dynamics of an effector protein, HP1, towards chemically defined chromatin fibres. HP1 α binding towards H3K9me3 dodeca-nucleosome arrays revealed double exponential dissociation kinetics with residence times of 100-300 ms in the major kinetic phase. The residence times were shown to be dependent on the density of H3K9me3 on the chromatin arrays, indicating that HP1 recruitment is provided by multiple micro-dissociation and rebinding events. A slower process on the seconds timescale was detected, which may arise from multivalent interactions. Increasing the HP1 α concentration reduced the residence time of bound molecules. This argues against the formation of higher order HP1 α oligomers, which was proposed for Swi6^{67,132}. However, Swi6 contains an extended α -helix in its CD as well as a lysine-containing loop, proposed to provide an additional site of interaction. Covalently linked dimeric HP1 α showed significantly faster association kinetics and longer residence times.

From these results we can propose a preliminary model (which will be extended in the following chapter). HP1 α is in a monomer-dimer equilibrium, once it is in the capture radius of H3K9me3 by non-specifically associating with the nucleosome it specifically binds to the mark correlating

3. HP1 α -chromatin binding at the single molecule level

with the residence times measured in our single molecule system. Importantly multivalent binding increases its affinity and association rate to chromatin. Residence times of HP1 to chromatin were short and may be a mechanism to provide competition with other effector proteins.

In the following chapter we will discuss the influence of chromatin state over the binding of HP1 α and study the three HP1 isoforms which are similar in structure but have potentially different mechanism.

Experimental system		Dissociation kinetics			Association kinetics			Equilibrium	Replicate
Chromatin	Effector	$\tau_{\text{off},1}$ (s)	%A1	$\tau_{\text{off},2}$ (s)	%A2	λ_{on} (s)	k_{on} ($\text{M}^{-1}\text{s}^{-1}$) $\times 10^6$	K_d	n
H3K9me3 (100 %)	HP1 α	0.25 \pm 0.03	87 \pm 7	2.26 \pm 1.22	13 \pm 7	22.9 \pm 9.8	3.64 \pm 1.56	1.16 \pm 0.54	16
H3K9me0	HP1 α	0.08 \pm 0.03	83 \pm 10	3.70 \pm 4.90 [†]	17 \pm 10	N/A [§]	N/A [§]	N/A [§]	3
H3K9me3 (75 %)	HP1 α	0.19 \pm 0.01	95 \pm 3	4.03 \pm 4.09	5 \pm 3	51.0 \pm 25.8	1.63 \pm 0.12	3.23 \pm 1.63	5
H3K9me3 (50 %)	HP1 α	0.17 \pm 0.03	94 \pm 6	4.09 \pm 3.62	6 \pm 6	48.2 \pm 15.2	1.73 \pm 0.59	3.40 \pm 1.24	6
H3K9me3 (25 %)	HP1 α	0.15 \pm 0.02	95 \pm 2	4.57 \pm 3.13	5 \pm 2	75.8 \pm 23.0	1.10 \pm 0.33	6.06 \pm 1.99	6
H3K9me3 (MN)	HP1 α	0.13 \pm 0.01	78 \pm 11	1.18 \pm 0.62 [†]	22 \pm 11	N/A [§]	N/A [§]	N/A [§]	13
H3K9me3 (100 %)	HP1 α +50 nM comp	0.19 \pm 0.05	94 \pm 3	3.97 \pm 1.31	6 \pm 3	23.8 \pm 2.84	3.55 \pm 0.17	1.48 \pm 0.43	5
H3K9me3 (100 %)	HP1 α +250 nM comp.	0.13 \pm 0.02	93 \pm 2	3.93 \pm 1.73	7 \pm 2	43.3 \pm 15.8	2.07 \pm 0.52	3.72 \pm 1.25	3
H3K9me3 (100 %)	HP1 α +1000 nM comp	0.11 \pm 0.01	93 \pm 4	2.75 \pm 0.72	7 \pm 4	29.3 \pm 5.51	2.92 \pm 0.37	3.11 \pm 0.67	4
H3K9me3 (100 %)	HP1 α cdm	0.33 \pm 0.01	87 \pm 1	3.40 \pm 0.53	13 \pm 1	7.45 \pm 1.87	22.4 \pm 0.16	0.13 \pm 0.01	4
H3K9me3 (100 %)	HP1 α (I63E)	0.23 \pm 0.10	85 \pm 7	4.11 \pm 2.83 [†]	15 \pm 7	N/A [§]	N/A [§]	N/A [§]	4
H3K9me3 (100 %)	HP1 α (W40A)	0.10 \pm 0.02	85 \pm 21	0.56 \pm 0.49 [†]	15 \pm 21	N/A [§]	N/A [§]	N/A [§]	2
H3K9me3 (100 %)	HP1 α +P3	0.33 \pm 0.04	95 \pm 4	4.80 \pm 3.96	5 \pm 4	10.5 \pm 0.59	0.38 \pm 0.03	0.38 \pm 0.05	4
H3K9me3 (100 %)	HP1 α +P4	0.28 \pm 0.01	93 \pm 4	4.45 \pm 2.10	7 \pm 4	19.6 \pm 6.52	0.84 \pm 0.08	0.38 \pm 0.05	4

Table 1 . Kinetic parameters of HP1 α interaction dynamics to chromatin. The percentage numbers in brackets denote the H3K9me3 modification density. MN denotes mononucleosomes, n is the number of replicates. [†]Due to insufficient statistics $\tau_{\text{off},2}$ is poorly defined. [§]Due to insufficient statistics association kinetics are not accurately determined

4. Investigating the influence of chromatin structure and HP1 subtypes on HP1 recruitment

This chapter is based on the following research article:

Single molecule kinetic analysis of HP1 chromatin binding reveals a dynamic network of histone modification and DNA interactions. Louise C. Bryan, Daniel R. Weilandt, Andreas L. Bachmann, Sinan Kilic, Carolin Lechner, Pascal D. Odermatt, Georg E. Fantner, Sandrine Georgeon, Oliver Hantschel, Vassily Hatzimanikatis and Beat Fierz. Nucleic Acids research. 2017

Contribution by other members is indicated in the text and in figure legends.

4.1. Background and overview

The previous chapter described the development of a single molecule TIRFM technique to determine the dynamic binding of HP1 α to H3K9me3 synthetic chromatin. This enabled us to improve our understanding on the recruitment mechanism of HP1 to heterochromatin. Following on from these results I continued working on HP1 to improve our model by focusing on the influence of chromatin structure on HP1 α binding, the differences between the three HP1 isoforms and a phosphorylation mark found on the N-terminal of HP1 α .

Many factors influence chromatin structure such as the ionic strength, the length of linker DNA connecting nucleosomes, inter-nucleosomal interactions and chromatin associated structural proteins such as histone H1^{12,15,140}. We thus decided to study the influence of chromatin fiber conformation on the binding and retention dynamics of HP1 α . We thought that a more condensed fiber, would lead to marks in very close proximity potentially leading to facilitated dynamic rebinding and multivalent interactions. However, the decompaction of chromatin fibers would lead to the spreading out H3K9me3 marks with capture radiuses further apart and a lower likelihood of HP1 rebinding.

As mentioned in the introduction, HP1 isoforms (HP1 α , HP1 β and HP1 γ) are structurally similar, however, they differ slightly in the unstructured hinge region as well as in the N- and

4. Investigating the influence of chromatin structure and HP1 subtypes on HP1 recruitment

C-terminal domains (Figure 5). Together, these sequence differences result in altered DNA interactions and differences in affinities towards the H3K9me3 peptide^{74,141}. We were therefore interested to analyse these isoforms at the single molecule level on chromatin fibers.

Finally, we studied the influence of a particular PTM on HP1 α itself, the phosphorylation of four serines only present on HP1 α and not the other two isoforms. Phosphorylated HP1 α was shown to lose its unspecific binding to DNA but increase its binding affinity to the H3K9me3 peptide^{74,141}.

4.2. Results & Discussion

4.2.1. The influence of chromatin structure on HP1 binding

12x 197bp DNA

First, we investigated the effect of expanding chromatin structure (i.e. increasing the distance between individual nucleosomes) on HP1 α binding. To this end, two different DNA constructs, based on a 12-mer array of the 601 nucleosome positioning sequence¹²⁹ were compared; the short nucleosome repeat length of 177 bp (from now on referred to as a177), which was used in the previous chapter (Figure 23) and a longer NRL of 197 bp (referred to as a197); resulting in 50 bp DNA linkers between nucleosomes (Figure 32A). The new DNA piece was prepared with the same protocol as for the a177 DNA, where the a197 DNA piece was cut out from a plasmid after its recombinant generation and then ligated to an anchor piece labeled with Atto647N (Figure 32B).

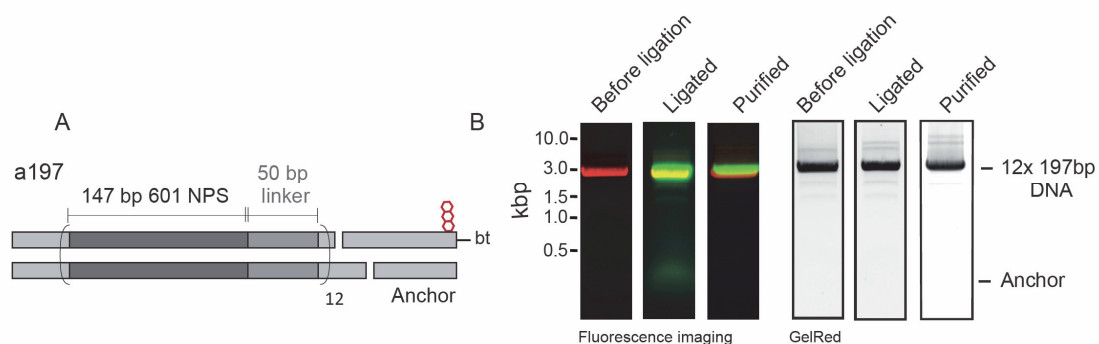


Figure 32. Preparation of 12x 197bp labeled chromatin DNA. A) Schematic representation of the 12x 147bp NPS with 50 bp DNA linkers. B) Production of fluorescently labeled and biotinylated 12x 147bp DNA. In the Fluorescence overlay, red: GelRed, green: Atto647N.

4. Investigating the influence of chromatin structure and HP1 subtypes on HP1 recruitment

H4K_s16ac synthesis

To further ensure an open, extended chromatin state, the acetylated H4K16 histone was introduced since it is known to disrupts key internucleosomal interactions⁵; experiments using hydrodynamic and spectroscopic methods have shown that incorporation of H4K16ac disrupts local and higher-order chromatin fiber decompaction^{24,40,142}. We decided that it was not essential to prepare the native modified protein and that a close structural analog would suffice since the aim was to influence the structure of chromatin provided by the charge at the H4 tail. H4 carrying the point mutation K16C was recombinantly expressed and purified (Figure 33A-C). For the site-specific installation of the acetyl-lysine analog, H4K16C was reacted with N-vinylacetamide in the presence of the radical initiator VA-044 (Figure 33D-F). Once the product was confirmed by analytical RP-HPLC and ESI-MS, the protein was purified by semipreparative RP-HPLC and lyophilised.

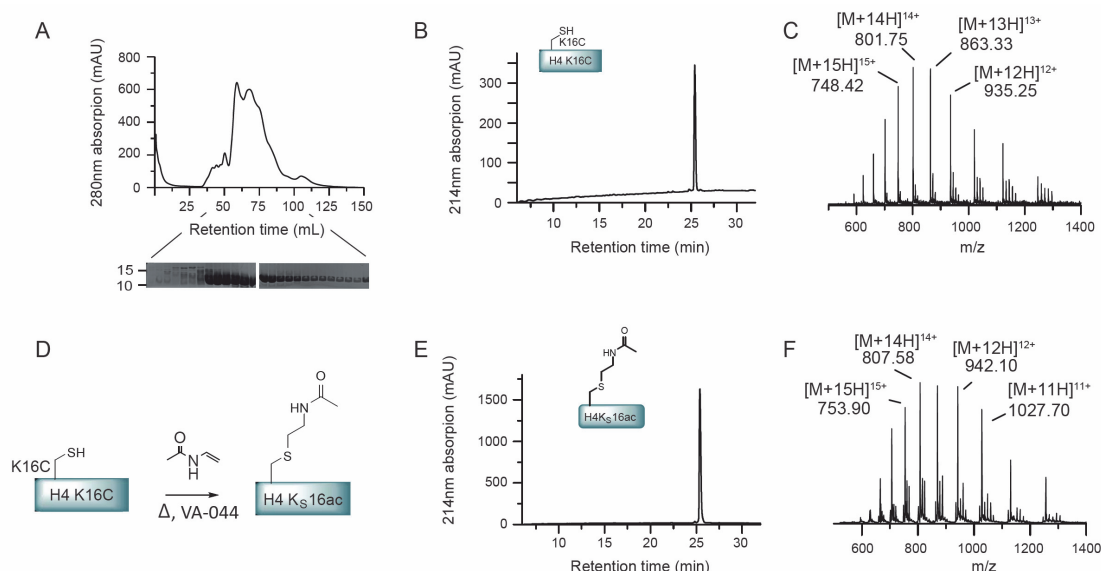


Figure 33. Preparation of H4K_s16ac. A) Ion exchange chromatography of H4K16C. B) RP-HPLC and C) ESI-MS analysis of purified H4K16C (calculated mass: 11211 Da, observed mass: 11211 Da). D) General scheme of the thiol-ene reaction to synthesize H4K_s16ac. E) RP-HPLC and F) ESI-MS analysis of the H4K_s16ac (calculated mass: 11296 Da, observed mass: 11293 Da).

Octamers and chromatin reconstitution

Histone octamers containing both H3K9me₃ and H4K_s16ac were refolded (Figure 34A and B). Four different chromatin fibers were reconstituted, either containing a177 or a197 DNA with H3K9me₃ or both H3K9me₃ and H4K_s16ac (Figure 34C-E).

4. Investigating the influence of chromatin structure and HP1 subtypes on HP1 recruitment

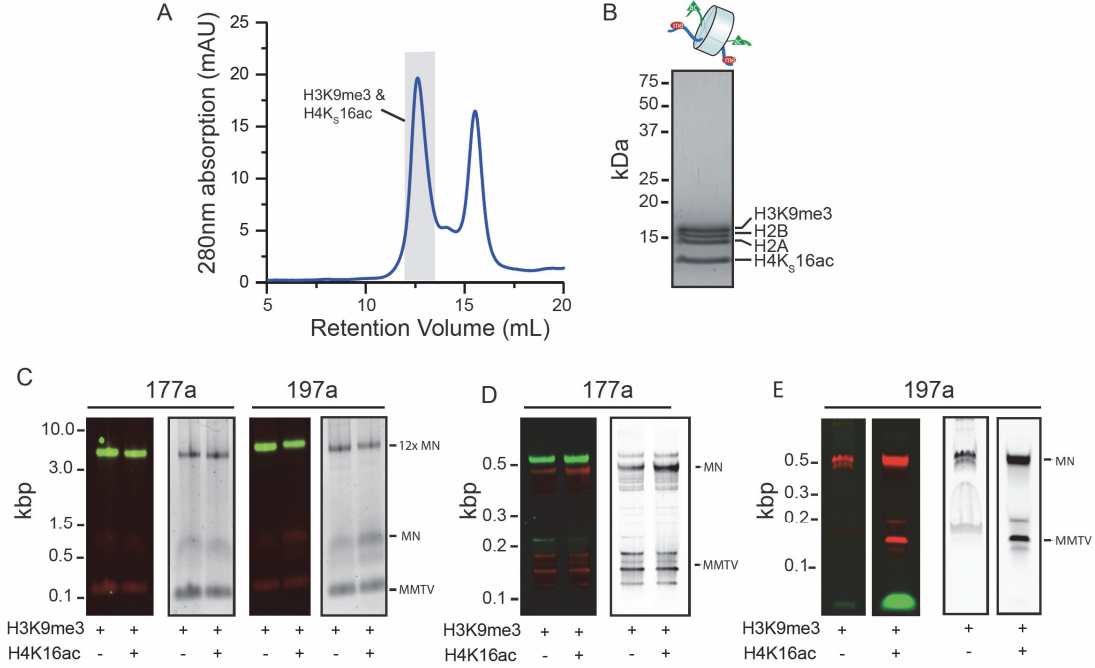


Figure 34. H3K9me3/H4K16ac octamer reconstitution and chromatin refolding. A) H3K9me3/H4K16ac octamers were purified by size exclusion chromatography. B) SDS-PAGE analysis of the H3K9me3/H4K16ac refolded octamers pooled and concentrated after size exclusion chromatography. C) Agarose gel analysis of reconstituted H3K9me3 or H3K9me3/H4K16ac labeled chromatin arrays with a177 or a197 DNA. Green: Atto647N, red: GelRed. Native PAGE analysis of *ScaI* digested H3K9me3 or H3K9me3/H4K16ac labeled chromatin arrays with D) a177bp or E) a197 DNA. Green: Atto647N, red: GelRed.

HP1 α binding to decondensed chromatin

Once the necessary components were prepared, HP1 α binding dynamics towards decondensed chromatin fibers were measured by smTIRF imaging (Figure 35A). In the absence of H4K16ac, the HP1 α residence time was not significantly different between a177 and a197 fibers. With the longer linker the short residence time was $\tau_{\text{off},1} = 0.25 \pm 0.03$ s with 95 % of binding events, compared to $\tau_{\text{off},1} = 0.25 \pm 0.03$ s with 87 % of binding events. For the second slower process, resulting from multivalent interactions, time constants of $\tau_{\text{off},2} = 2.3 \pm 1.2$ (a177) and 2.5 ± 0.3 s (a197) were obtained (Figure 35D and E, Table 2). The similar behaviour of HP1 α indicates that the local density of PTMs is comparable in compact chromatin fibers with a NRL of 177 or 197 bp. This is in agreement with cryo-electron microscopy studies of chromatin fibers of different linker length²⁰, where 177 bp NRL and 187 bp NRL fibers were compared and an increase in 10 bp of the linker DNA did not affect the general zigzag two-start

4. Investigating the influence of chromatin structure and HP1 subtypes on HP1 recruitment

helix structure of the chromatin with fiber dimensions (diameter \times height) from about 27.2×28.7 nm for 177 bp NRL to about 29.9×27.0 nm for 187 bp NRL.

Chromatin fibers containing H4K_s16ac adopt an open chromatin state^{24,40,43,142}. In this chromatin context, the HP1 α residence times were accordingly reduced by 25–35% for $\tau_{\text{off},1}$ and by a similar degree for $\tau_{\text{off},2}$ (Figure 35B-E, Table 2). Importantly, this effect was more pronounced for a197 than for a177 fibers, indicating that the lower density of binding sites provided by both longer linker length and H4K_s16ac, reduced the probability of HP1 α to rebind after dissociation. Together, these measurements thus indicate that HP1 α retention is sensitive to chromatin fiber conformation: chromatin decompaction lowers the local H3K9me3 density, reducing both multivalent binding and the probability of re-binding of transiently dissociated HP1 α , thereby shortening the HP1 α residence time.

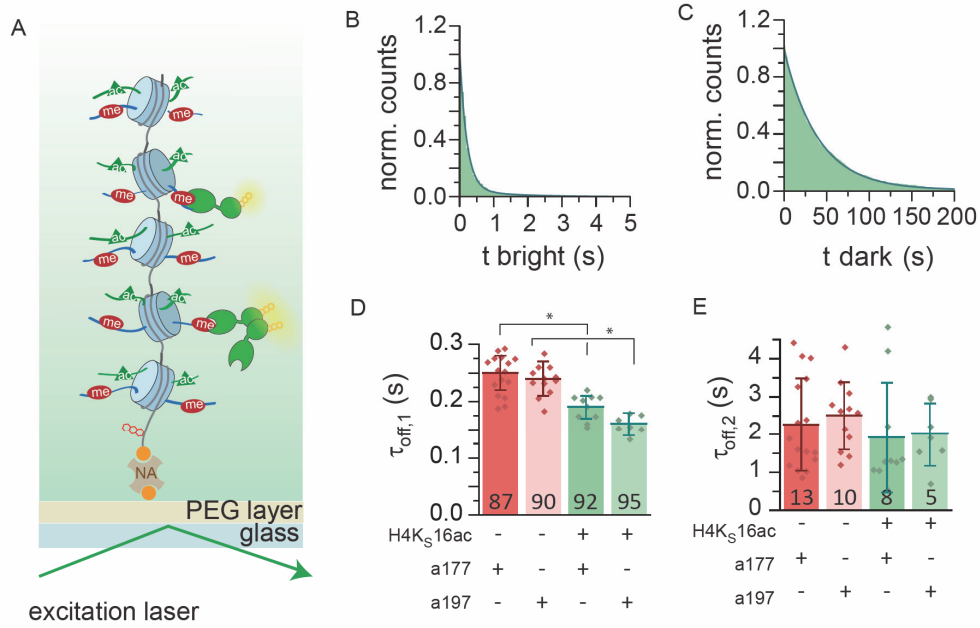


Figure 35. HP1 α binding to H3K9me3 & H4K_s16ac chromatin. A) Schematic representation of a smTIRF experiment with 1 nM Atto532 labeled HP1 and H3K9me3/H4K_s16ac chromatin bound to the surface of the coverslip through a neutravidin-biotin interaction. B) Dissociation kinetics of HP1 α binding to H3K9me3/H4K_s16ac chromatin: cumulative histogram of binding intervals (t_{bright}) fitted by a double-exponential function. C) Association kinetics of HP1 α binding to H3K9me3/H4K_s16ac chromatin: cumulative histogram of intervals between binding events (t_{dark}) fitted by a single-exponential function. D-E) Chromatin decompaction by H4K_s16ac reduces $\tau_{\text{off},1}$ and $\tau_{\text{off},2}$ in both a177 and a197 fibers. Numbers indicate % amplitude. Error bars: standard deviation (s.d.), $n = 7$ –16 replicates, $*P < 0.05$, Student's t -test.

Histone H1.1

After measuring HP1 binding to decondensed chromatin, the next step was to investigate HP1 α interaction dynamics to compact chromatin, where the local density of H3K9me3 marks is increased.

Chromatin fibers have been shown to be efficiently compacted by linker histone H1 incorporation^{20,143} and heterochromatin regions contain near stoichiometric levels of linker histone H1. We therefore decided to create compact chromatin fibers with the addition of histone H1.1.

Human histone H1.1 was recombinantly expressed from *E. Coli* and purified by cation exchange and then size exclusion chromatography (Figure 36A-C).

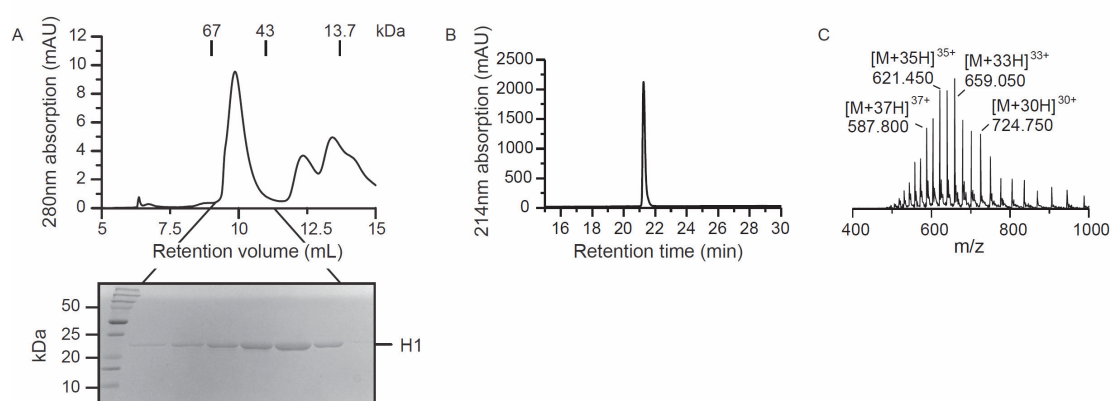


Figure 36. Purification of Histone H1.1. A) Size exclusion chromatography and SDS-PAGE of histone H1.1 purification. B) Analytical RP-HPLC and C) ESI-MS of purified histone H1.1. (Calculated mass: 21711 Da, observed mass: 21714 Da).

Labeled H1.1 was also prepared since this would allow us to control the correct formation of chromatin fibers and check that the protein stays bound to the chromatin fiber in our TIRF microscopy system. For fluorescent labeling, a cysteine residue was added to the C-terminus of H1.1 by site-directed mutagenesis. After recombinant expression and purification by cation exchange, the protein was reacted with Atto532-iodoacetamide, overnight at 4°C. The dye was quenched with TCEP and purification was achieved by size exclusion chromatography (Figure 37A-C).

4. Investigating the influence of chromatin structure and HP1 subtypes on HP1 recruitment

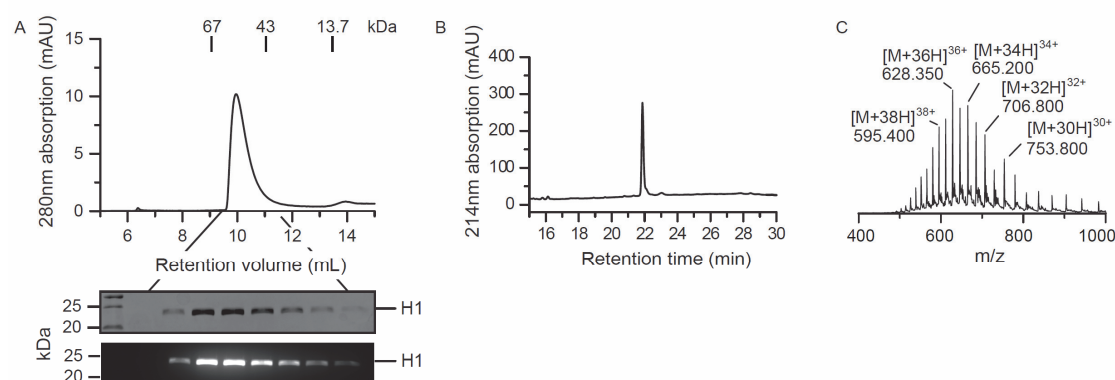


Figure 37. Purification and labeling of H1.1-A532. A) Size exclusion chromatography and SDS-PAGE of H1.1-A532 purification. B) Analytical RP-HPLC and C) ESI-MS of purified Histone H1.1-A532 (Calculated mass: 22582 Da, observed mass: 22587 Da).

Chromatin reconstitution with Histone H1.1

To reconstitute chromatin with Histone H1.1, the linker histone was added to the histone octamers and DNA mixture before dialysis, different equivalents were prepared and those with 0.5, 1 and 1.5 were used for single molecule measurements. After the dialysis, the reconstituted chromatin arrays were analyzed on a 0.6 % agarose gel (Figure 38A) or non-denaturing 5 % polyacrylamide gel electrophoresis (PAGE) in 0.5 x Tris- Borate-EDTA (TBE) running buffer following ScaI restriction digest (Figure 38B). Interestingly, addition of H1.1 led to a stepwise shift on the agarose gel and inhibited ScaI digest (Figure 38B).

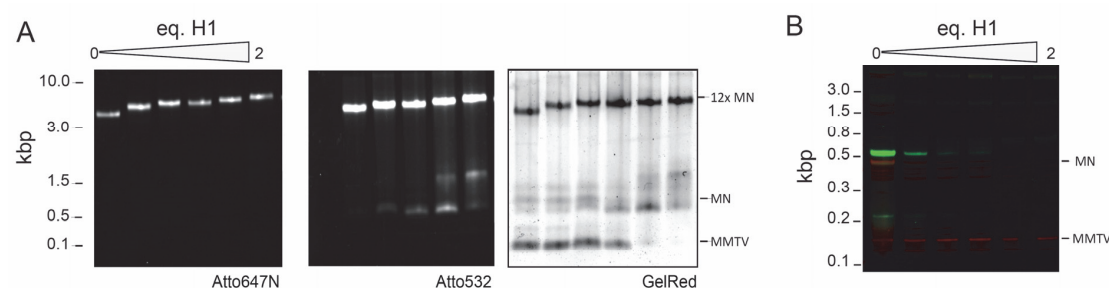


Figure 38. Reconstitution of chromatin with H1.1. A) Agarose gel analysis of reconstituted chromatin with 0-2 eq. of H1-A532. B) Native PAGE analysis of ScaI digested chromatin with 0-2 eq. H1.1. Green: Atto647N, red: GelRed.

AFM imaging of chromatin fibers

We also wanted a more visual method to observe condensed and decondensed chromatin fibers. In collaboration with Pascal Odermatt, a PhD student from the Laboratory for Bio- and Nano- Instrumentation, EPFL, atomic force microscopy (AFM) was used to image chromatin fibers (Figure 39A-C). AFM is used to get a topological image of a sample. The probe or AFM

4. Investigating the influence of chromatin structure and HP1 subtypes on HP1 recruitment

tip is attached to a flexible cantilever and a laser beam is reflected off the back of this cantilever onto a photo-diode which is a position sensitive detector (*Figure 39A*). Two types of imaging modes can be performed, the contact mode, where the AFM tip is in constant contact with sample surface or the tapping mode, where the cantilever oscillates, thereby reducing lateral forces on the sample and reducing sample damage^{144,145}. After reconstitution, chromatin fibers with or without H1.1 were fixed with glutaraldehyde and transferred onto a freshly cleaved mica surface. Atomic force microscopy images of the dried chromatin fibers were acquired in tapping mode in air. We observed a clear difference between chromatin fibers without H1 (*Figure 39B*) which formed a ‘beads on a string’ structure and chromatin fibers with H1 that formed compacted structures (*Figure 39C*).

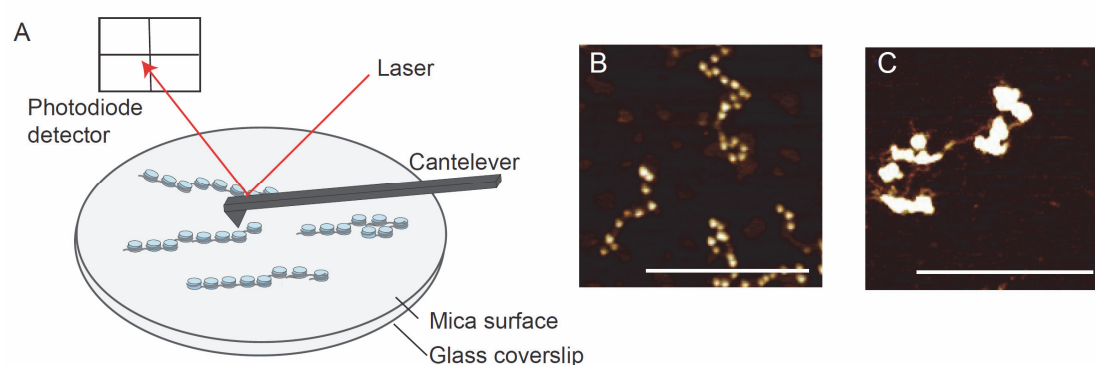


Figure 39. AFM of chromatin fibers. A) Schematic representation of AFM, where the AFM tip, attached to a cantilever probes the surface of the sample. A laser is reflected off the back of the cantilever and detected with a photodiode detector. B) AFM image of chromatin fibers without H1 and C) with H1. Scale bar: 400 nm. In collaboration with Pascal Odermatt.

H1.1 behaviour on chromatin at the single molecule level

To ensure stable H1.1 incorporation under single-molecule conditions, chromatin fibers were prepared containing H2A labeled with Alexa Fluor 488 at position 110 and H1.1 labeled with Atto532 at its C-terminus (*Figure 37*). We then confirmed the colocalization of H1.1, H2A as well as chromatin DNA on the single-molecule level (*Figure 40A and B*). To determine the occupancy of H1.1 on chromatin arrays, Atto532-labeled H1.1 was imaged for 60 s with high laser intensity. Stepwise photobleaching was observed (*Figure 40D*) and analysed from the recorded traces using a step-detection algorithm. This analysis revealed that in chromatin fibers with 50 bp linker DNA (a197) a 1:1 stoichiometry of H1.1 to nucleosome was established (*Figure 40F*). In contrast, for a177 only one H1.1 molecule was incorporated per di-nucleosome (*Figure 40E*), in agreement with earlier reports¹⁴³. To determine the residence time of H1.1 on a chromatin fiber, single molecule measurements were performed as follows: Chromatin fibers

4. Investigating the influence of chromatin structure and HP1 subtypes on HP1 recruitment

were imaged with excitation from the 647 nm laser over 100 ms for localization, subsequently Atto532-labeled H1.1 was imaged over 2000 s with 100 ms exposure time. The delay between each excitation was increased stepwise up to 40 s to avoid contributions from photobleaching (Figure 40C). The traces from 50 different arrays were then averaged and fitted with a bi-exponential function. We thus determined the residence time of H1.1 under our experimental conditions, and observed that the majority of H1.1 molecules (70 %) remained bound over a 33 min observation period, whereas a smaller subset (30 %) dissociated with a 5 min time constant (Figure 40B). For H1 binding to nucleosomes, residence times of up to 25 min were reported *in vitro*¹⁴⁶. While these residence times are sufficiently long compared to our experimental timescale (~10 min), we ensured full H1.1 saturation by performing the measurements in the presence of 100 pM H1.1 added to the measurement buffer.

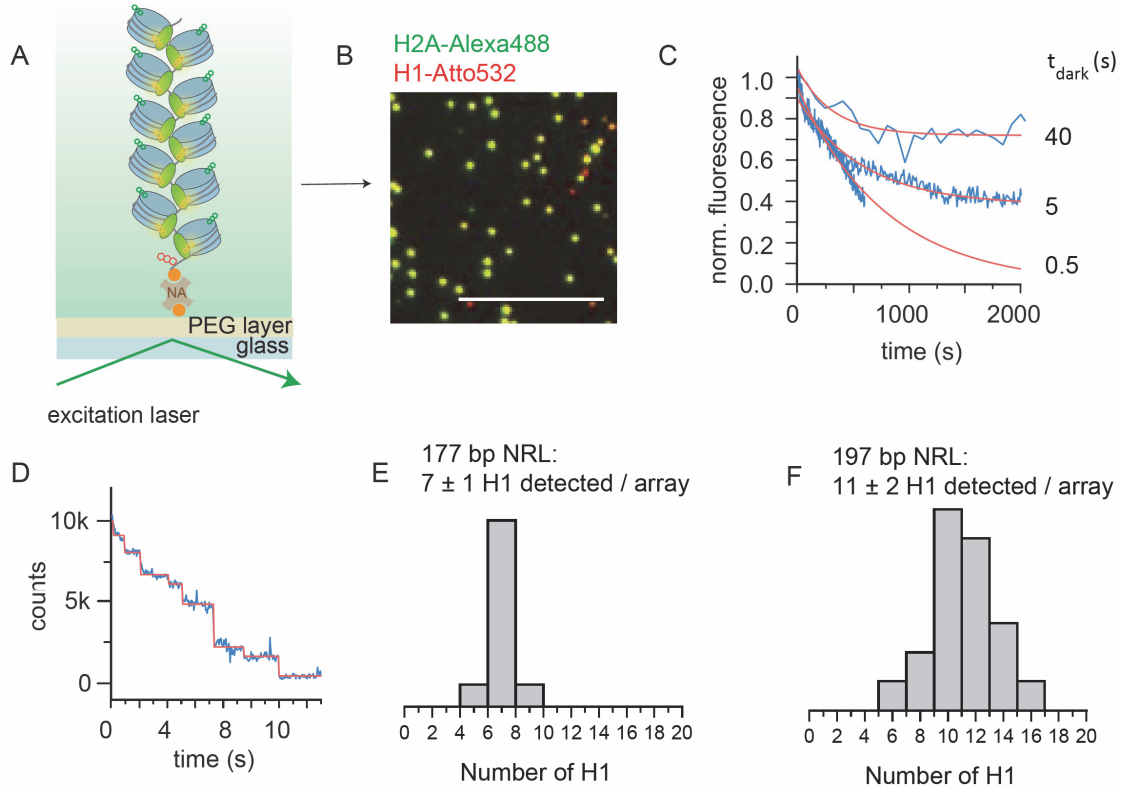


Figure 40. Characterizing H1.1 residence on chromatin fibers. A) Schematic representation of chromatin fibers reconstituted with H1.1-Atto532 and H2A-Alexa488. B) Single molecule analysis green: H2A-Alexa488, red: H1-Atto532. Scale bar: 10 μm . C) Determination of the residence time of H1-Atto532: >50 chromatin fibers are imaged using stroboscopic imaging with the indicated dark times ($t_{\text{dark}} = 0.5, 5, 40$ s). For the longest t_{dark} , only H1.1 dissociation is limiting showing 70 % of molecules remaining bound >2000 s, whereas 30 % dissociate with $\tau = 313$ s. D) Example of stepwise bleaching of fibers containing H1-Atto532. E) Analysis of H1 content of chromatin fibers by step-wise bleaching analysis, demonstrating 7 H1/array for a 177 chromatin and F) 11 H1/array for a 197 chromatin.

HP1 α binding to condensed chromatin

Having established suitable experimental conditions, we proceeded to measure HP1 α dissociation and association kinetics with chromatin fibers that were compacted by H1.1 (Figure 41A). For a177 fibers we observed a decrease in $\tau_{\text{off},1}$ with H1.1 incorporation (from 0.25 s without H1 to 0.19 s for 1 eq. H1), which was concomitant with an increase in $\tau_{\text{off},2}$ (from 2.26 s without H1 to 3.68 s for 1 eq. H1). Similarly, in a197 fibers $\tau_{\text{off},2}$ was increased from 2.49 ± 0.26 s to 3.63 ± 0.39 s (Figure 41D and E, Table 2), however without a change in $\tau_{\text{off},1}$ (Figure 41D and E, Table 2). These results, in particular for a197 fibers, thus show that chromatin compaction by H1.1 induces a prolongation of the HP1 α residence time. In both array contexts (a177 or a197 with H1), chromatin compaction increases H3K9me3 density, facilitating multivalent interactions. These findings are in agreement with equilibrium experiments of HP1 binding in compact chromatin^{63,147}. The stabilizing effect may however be mitigated by H1.1 leading to steric restriction¹⁴⁸ and changes in H3 tail mobility¹⁴⁹. Moreover, the basic, unstructured tail of H1 interacts with linker DNA¹⁵⁰, thereby shielding DNA charges and reducing electrostatic interactions, which might be important for HP1 α recruitment and retention.

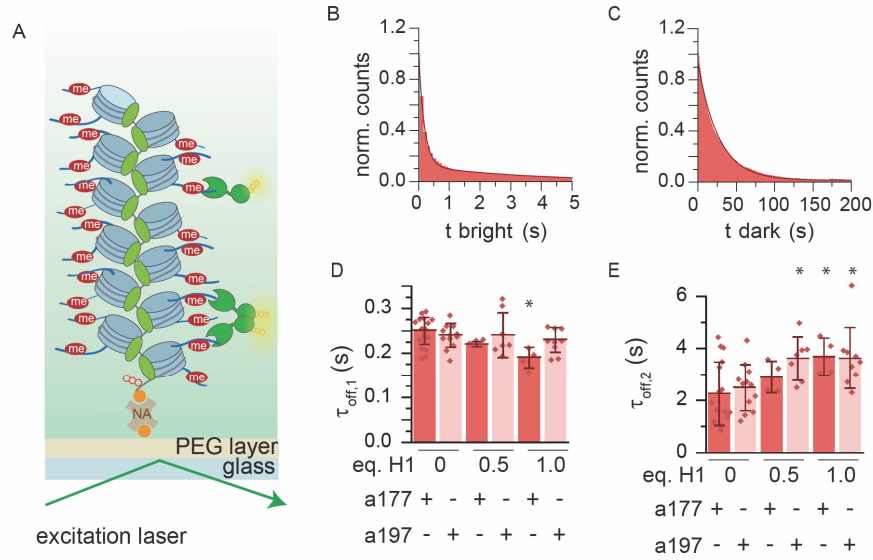


Figure 41. HP1 α binding to condensed chromatin. A) Schematic representation of a smTIRF experiment with 1 nM Atto532 labeled HP1 and condensed chromatin bound to the surface of the coverslip through a neutravidin-biotin interaction. B) Dissociation kinetics of HP1 α binding to H3K9me3 and H1.1 chromatin: cumulative histogram of binding intervals (t_{bright}) fitted by a double-exponential function. C) Association kinetics of HP1 α binding to H3K9me3 and H1.1 chromatin: cumulative histogram of intervals between binding events (t_{dark}) fitted by a single-exponential function. D) Dependence of $\tau_{\text{off},1}$ and E) $\tau_{\text{off},2}$ on H1.1 incorporation for both a177 and a197 chromatin fibers. Error bars: s.d., $n = 4-16$ replicates, * $P < 0.05$ versus fibers of the same NRL without H1.1, Student's t -test.

4. Investigating the influence of chromatin structure and HP1 subtypes on HP1 recruitment

Experimental system			Dissociation kinetics			Association kinetics		Equilibrium	Replicate
Chromatin	NRL	Effector	$\tau_{off,1}$ (s)	%A1	$\tau_{off,2}$ (s)	%A2	k_{on} ($M^{-1}s^{-1}$) $\times 10^6$	K_d	n
H3K9me3	177	HP1 α	0.25 \pm 0.03	87 \pm 7	2.26 \pm 1.22	13 \pm 7	3.64 \pm 1.56	1.16 \pm 0.54	16
H3K9me3 & H4K16ac	177	HP1 α	0.19 \pm 0.02	92 \pm 4	1.92 \pm 1.45	8 \pm 4	2.76 \pm 1.58	2.58 \pm 1.42	10
H3K9me3 0.5 eq H1	177	HP1 α	0.22 \pm 0.01	95 \pm 2	2.90 \pm 0.60	5 \pm 2	3.34 \pm 2.46	1.34 \pm 0.07	4
H3K9me3 1 eq H1	177	HP1 α	0.19 \pm 0.02	95 \pm 3	3.68 \pm 0.72	5 \pm 3	2.84 \pm 1.19	2.16 \pm 0.85	4
H3K9me3 1.5 eq H1	177	HP1 α	0.20 \pm 0.01	91 \pm 2	3.68 \pm 0.79	9 \pm 2	1.96 \pm 0.65	2.85 \pm 1.27	4
H3K9me3	197	HP1 α	0.24 \pm 0.03	90 \pm 7	2.49 \pm 0.89	10 \pm 7	2.51 \pm 0.82	1.87 \pm 0.70	12
H3K9me3 & H4K16ac	197	HP1 α	0.16 \pm 0.02	95 \pm 5	2.00 \pm 0.83	5 \pm 5	2.25 \pm 0.44	2.96 \pm 0.91	7
H3K9me3 0.5 eq H1	197	HP1 α	0.24 \pm 0.05	92 \pm 5	3.61 \pm 0.84	8 \pm 5	1.29 \pm 0.65	1.29 \pm 0.65	7
H3K9me3 1 eq H1	197	HP1 α	0.23 \pm 0.03	92 \pm 3	3.61 \pm 0.84	8 \pm 3	1.61 \pm 0.77	1.61 \pm 0.77	9
H3K9me3 1.5 eq H1	197	HP1 α	0.22 \pm 0.01	92 \pm 1	3.76 \pm 0.28	8 \pm 1	1.52 \pm 0.25	1.52 \pm 0.25	5

Table 2. Kinetic parameters of HP1 α interaction dynamics to condensed or open chromatin.
n is the number of replicates

4.2.2. Dynamic interactions of HP1 isoforms to H3K9me3 chromatin

HP1 α , HP1 β and HP1 γ

HP1 α , β and γ differ mainly in the unstructured hinge region (HR) as well as in the N- and C-terminal domains (Figure 5). Together, these sequence differences result in altered DNA interactions, mediated by a stretch of basic amino acids in the HR: HP1 β and HP1 γ have been reported to exhibit significantly reduced DNA binding compared to HP1 α . Thus, to explore the relationship between DNA interactions and PTM recognition by HP1 proteins in a chromatin context, we decided to perform a comparative study of the three mammalian HP1 isoforms. To investigate their chromatin binding dynamics, HP1 β (Figure 42A-D) and HP1 γ (Figure 42E-H) were recombinantly expressed, purified and fluorescently labeled with same procedure as for HP1 α .

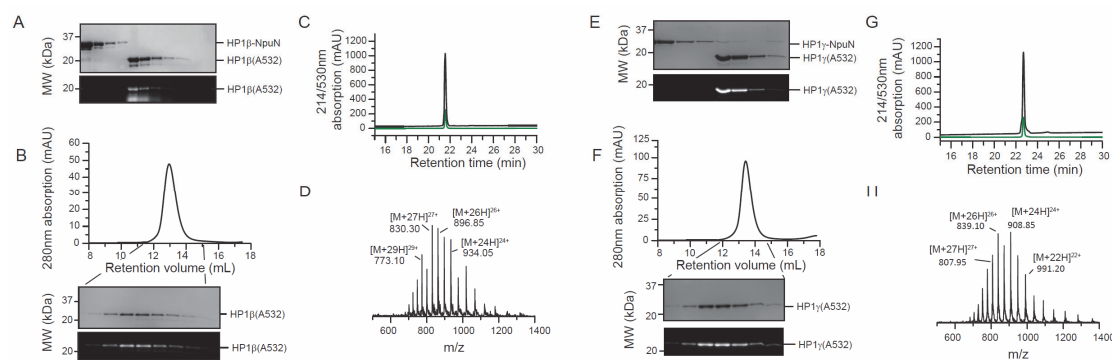


Figure 42. Purification and labeling of HP1 β and HP1 γ . A) SDS-PAGE analysis before and after labeling of HP1 β . B) Purification of HP1 β -A532 by size exclusion chromatography. C) RP-HPLC of HP1 β -A532 (black curve: 214 nm and green curve: 530 nm). D) MS of HP1 β -A532 (HP1 β : calculated mass: 22390 Da, observed mass: 22394 Da). E) SDS-PAGE analysis before and after labeling of HP1 γ . F) Purification of HP1 γ -A532 by size exclusion chromatography. G) RP-HPLC of HP1 γ -A532 (black curve: 214 nm and green curve: 530 nm). H) MS of HP1 γ -A532 (HP1 γ : calculated mass: 21786 Da, observed mass: 21789 Da).

Electromobility shift assay

Prior to performing single molecule experiments, two in vitro experiments were done. First of all, an electrophoretic mobility shift assay (EMSA) was carried out to determine the unspecific binding of the different HP1 isoforms to DNA (Figure 43). Three different concentrations of DNA were incubated with a DNA piece containing the 601 Widom sequence and a Cy5 label for 15 min at 37°C, which were then analysed on a non-denaturing 5 % polyacrylamide gel. We observed that HP1 α is the only isoform that can unspecifically bind to

4. Investigating the influence of chromatin structure and HP1 subtypes on HP1 recruitment

DNA at a concentration of 7 μ M. We also observed a shift dependent on the concentration of HP1 α , implying that the ratio DNA to HP1 α is not 1:1.

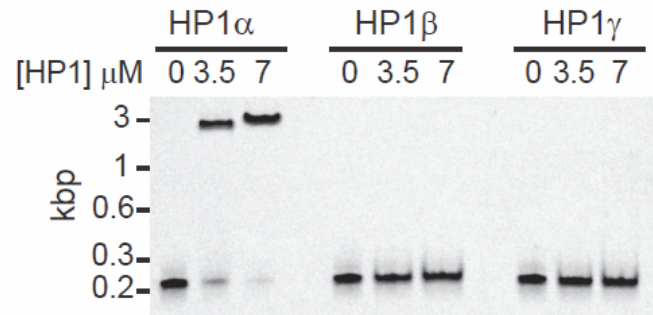


Figure 43. Electrophoretic mobility shift assay of HP1 α , HP1 β and HP1 γ . The three different HP1 isoforms were incubated at 0, 3.5 and 7 μ M concentration with a 193bp DNA piece and analysed on a non-denaturing 5 % polyacrylamide gel.

HP1 α hinge mutant

As mentioned previously, HP1 α , β and γ differ mainly in the unstructured HR (hinge region). HP1 β and HP1 γ have been reported to exhibit significantly reduced DNA binding compared to HP1 α ¹⁴¹. To confirm that the increased DNA interactions of HP1 α originates from the hinge-region an EMSA was performed with HP1 α mutated at its hinge region. HP1 α was expressed and purified where the six lysines/arginine residues localized in the hinge region, were converted to alanine (Figure 44D)¹⁴¹.

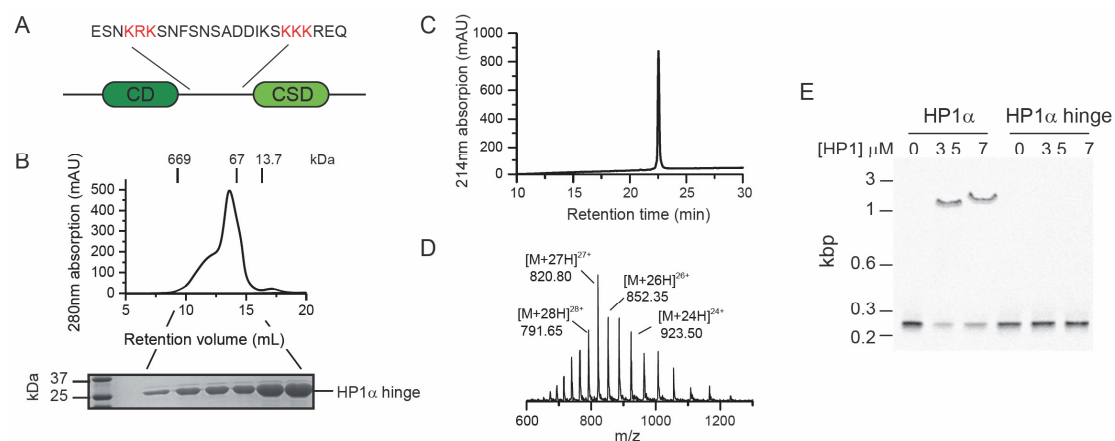


Figure 44. Purification and EMSA of the HP1 α hinge mutant. A) Schematic representation of HP1 α , where the amino acids highlighted in red are mutated to alanine to provide the HP1 α hinge mutant. B) Purification of HP1 α hinge by size exclusion chromatography. C) RP-HPLC of HP1 α hinge mutant. D) MS of HP1 α hinge mutant (calculated mass: 22136 Da, observed mass: 22137 Da). E) EMSA of HP1 α and HP1 α hinge mutant and a 193bp DNA piece analysed on a non-denaturing 5% polyacrylamide gel.

4. Investigating the influence of chromatin structure and HP1 subtypes on HP1 recruitment

The HP1 α -hinge mutant was expressed in *E.Coli*, purified by Ni-affinity and then anion exchange chromatography to remove DNA. The hexa-histidine-tag was then removed by thrombin cleavage and the protein was finally purified by size exclusion chromatography (Figure 44B). The electrophoretic mobility shift assay did not display a band shift for the HP1 α hinge mutant up to 7 μ M protein concentration. We can therefore confirm that the lysine and arginine residues at the hinge region are important for HP1 α 's unspecific binding to DNA (Figure 44E).

Microscale Thermophoresis

Binding studies between the HP1 isoforms and the H3K9me3 (1-14) peptide were performed by microscale thermophoresis (MST) which relies on thermophoresis (the directed motion of molecules in temperature gradients)¹⁵¹. Visible light is used for fluorescence excitation, for which different types of LED-filters can be used. An infrared (IR) laser with a wavelength of 1480 nm is coupled into the light path of fluorescence excitation/emission. In a first step, the fluorescence of the sample (placed in a glass capillary) is measured (Figure 45A). Then, a localized spot is heated by IR radiation for several seconds (Figure 45B). This leads to an abrupt change in fluorescence of the molecules owing to the temperature change and then relatively slow thermophoresis which is a diffusion-limited process and lasts several seconds.

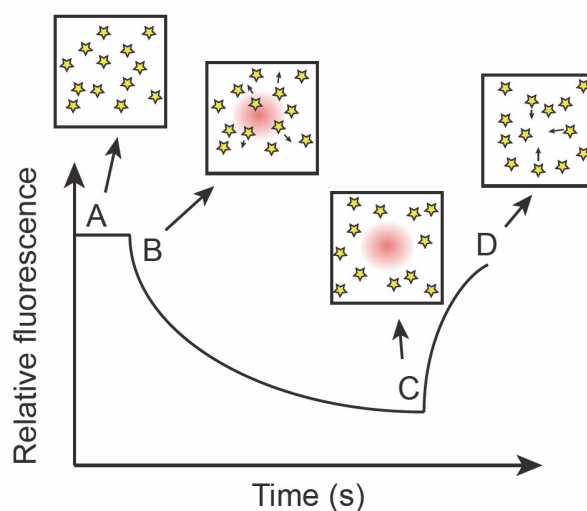


Figure 45. Microscale Thermophoresis. A) The fluorescence of the sample is measured. B) A localized spot is heated by IR radiation for several seconds. This leads to an abrupt change in fluorescence of the molecules owing to the temperature change and then relatively slow thermophoresis which is a diffusion-limited process and lasts several seconds until the fluorescence reaches a plateau C). D) The IR laser is switched off and fluorescence is recovered.

4. Investigating the influence of chromatin structure and HP1 subtypes on HP1 recruitment

The thermophoretic motion creates a concentration gradient of the fluorescent molecules. The fluorescence intensity reaches a plateau representing the steady state in which thermodiffusion is counter balanced by mass diffusion (Figure 45C). Finally, the IR-laser is switched off and the fluorescence is recovered (Figure 45D), and back diffusion, driven by pure mass diffusion, leads to the compensating of the concentration gradient. An advantage of the technique is that low amounts of protein or peptides are needed and the measurement is relatively fast¹⁵¹.

To measure binding affinities of HP1 to H3K9me3, the labeled protein was added to a serial dilution of the peptide and loaded onto premium coated capillaries. A cap scan was performed at 20 % detection light intensity to check that each capillary contained the same amount of protein. Thermophoresis was measured at 40 or 60 % infrared heating-laser power. Data were normalized to the start and end point, averaged and fitted with a quadratic binding equation (Figure 46A-C). From these fittings we obtained the following binding affinities; HP1 α binds with the lowest affinity to the peptide with a K_D of 11.6 μ M. HP1 β binds with the strongest affinity with 1.4 μ M and HP1 γ binds with an affinity of 4.1 μ M.

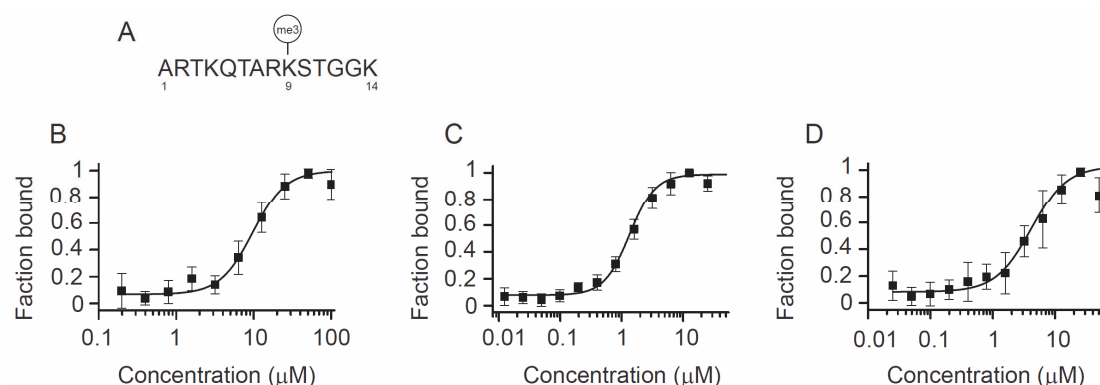


Figure 46. Microscale thermophoresis of HP1 α , β and γ binding to H3K9me3 peptide. A) Sequence of the H3K9me3 (1-14) peptide. B) HP1 α binding to a H3K9me3 (1-14) peptide, $K_D = 11.6 \mu$ M. C) HP1 β binding to a H3K9me3 (1-14) peptide, $K_D = 1.4 \mu$ M. D) HP1 γ binding to a H3K9me3 (1-14) peptide, $K_D = 4.1 \mu$ M. All fittings were done with a quadratic binding equation with a one-site binding model.

In summary, we confirmed that HP1 α interacts with DNA by EMSA, whereas DNA binding was found to be greatly reduced for HP1 β and HP1 γ . In addition to differences in DNA binding, HP1 isoforms also exhibit varying affinities for their target histone PTM. The affinity for H3K9me3 was increased for both HP1 β and HP1 γ compared to HP1 α when measuring binding to a modified histone peptide⁷⁹.

HP1 α , β and γ binding to H3K9me3 chromatin

The next step was to measure the dynamic binding of HP1 β and HP1 γ at the single molecule level. We initially thought that owing to their higher affinity for the H3K9me3 modification, single molecule measurement would reveal increased residency on the chromatin fiber. Surprisingly, we found that the major residence time, $\tau_{\text{off},1}$, for both HP1 β and HP1 γ was reduced compared to HP1 α (Figure 47A, Table 3), indicating weaker chromatin binding in spite of their higher affinity for H3K9me3. The binding rate constants, k_{on} , were significantly lowered compared to HP1 α , for HP1 β by a factor of 5.8 and for HP1 γ by a factor of 3.9 (Figure 47B, Table 3). Only the slow dissociation process of HP1 β exhibited an increased time constant ($\tau_{\text{off},2}$) compared to the α -isoform (Figure 47A), indicating the presence of a strongly bound molecular subpopulation.

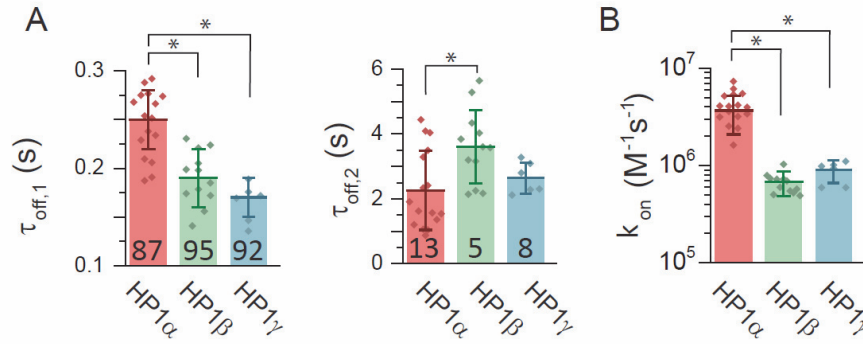


Figure 47. HP1 HP1 α , HP1 β and HP1 γ binding to H3K9me3. Comparison of A) dissociation time constants ($\tau_{\text{off},1}$ and $\tau_{\text{off},2}$) and B) association rate constants (k_{on}) obtained from smTIRF experiments for HP1 α , HP1 β and HP1 γ and a177 H3K9me3 chromatin fibers. Error bars: s.d., $n = 4\text{--}16$ replicates, * $P < 0.05$ versus fibers of the same NRL, Student's t-test.

Salt dependence of HP1 α binding

Based on these observations, we hypothesized that DNA interactions could be the origin behind the fast binding kinetics of HP1 α and its prolonged residence time on chromatin. We therefore tested if shielding charge–charge interactions by increasing the ionic strength of the solution might reduce fast binding and chromatin retention of HP1 α . Indeed, increasing the ionic strength from 130 to 260 mM KCl resulted in both a decrease in HP1 α residence time (from 0.25 s for 130 mM KCl to 0.14 s for 260 mM KCl for the short residence times) as well as a 10-fold reduction in the binding rate constant (Figure 48, Table 3). However, we cannot exclude that secondary salt-effects contribute to the observed changes in interaction kinetics, for example, changes in H3 tail dynamics or alterations in local chromatin structure. These

4. Investigating the influence of chromatin structure and HP1 subtypes on HP1 recruitment

effects, in accordance with our own results are however most likely smaller in magnitude compared to direct charge based DNA interactions. Together, these experiments thus reveal that DNA interactions play an important role for HP1 recruitment to chromatin.

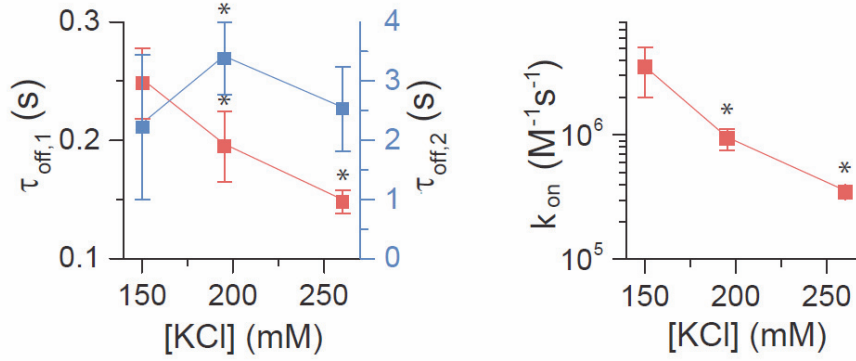


Figure 48. HP1 α binding to H3K9me3 chromatin at increasing salt concentrations. $\tau_{off,1}$, $\tau_{off,2}$ and k_{on} for HP1 α at 130 mM-260mM salt concentration. Error bars: s.d., $n = 4-16$ replicates, * $P < 0.05$ versus fibers of the same NRL with 130 mM KCl, Student's t -test.

4.2.3. Dynamic interactions of phosphorylated HP1 α to H3K9me3 chromatin

Phosphorylated HP1 α

In the cell, PTMs on the HP1 proteins themselves provide a mechanism to regulate the strength of DNA binding. Indeed, mass-spectrometry studies allowed to map PTMs on each HP1 isoform revealing a complex modification landscape⁷². In particular, a number of phosphorylation sites were identified on all HP1 proteins. HP1 α is unique in that it contains an N-terminal extension (NTE) containing four serine residues (Figure 5D and Figure 49A) which have been found to be highly phosphorylated *in vivo*^{74,141}. Phosphorylation of these serines was shown to increase affinity for H3K9me3, while at the same time decreasing DNA binding^{74,152}. Intriguingly, these PTMs were also identified in stimulating HP1 α multimerization, thereby increasing multivalency and inducing phase-separation behavior¹⁴¹.

We were thus interested in characterizing the effect of NTE phosphorylation on HP1 α binding dynamics. We used casein kinase 2 (CK2) to phosphorylate HP1 α . In order to determine optimal conditions for the enzymatic reaction, HP1 was mixed with increasing amounts of CK2 and ATP spiked with $[\gamma\text{-}^{32}\text{P}]\text{-ATP}$. After incubation at 37°C for 3 hours the reaction mixture was analyzed by 12 % (SDS)-PAGE followed by autoradiography detection (Figure 49C). To determine the number of phosphorylation sites in each reaction, the gel was dried and the bands

4. Investigating the influence of chromatin structure and HP1 subtypes on HP1 recruitment

corresponding the protein were cut out and their radioactivity was measured by calibrated scintillation counting. Since HP1 phosphorylation reached saturation when reacted with 100 U CK2, we used this condition to prepare phosphorylated HP1 α in smTIRF measurements (ATP was removed by dialysis). HP1 α phosphorylated by CK2 displayed no binding to DNA in the EMSA assay with up to 7 μ M in protein concentration (*Figure 49D*). Interestingly, it has been shown that phosphorylated HP1 α has stronger affinity to the H3K9me3 since the phosphorylated serines at the N-terminal create a strong negatively charged platform that electrostatically interacts with K14 and K18 on the histone H3¹⁴¹.

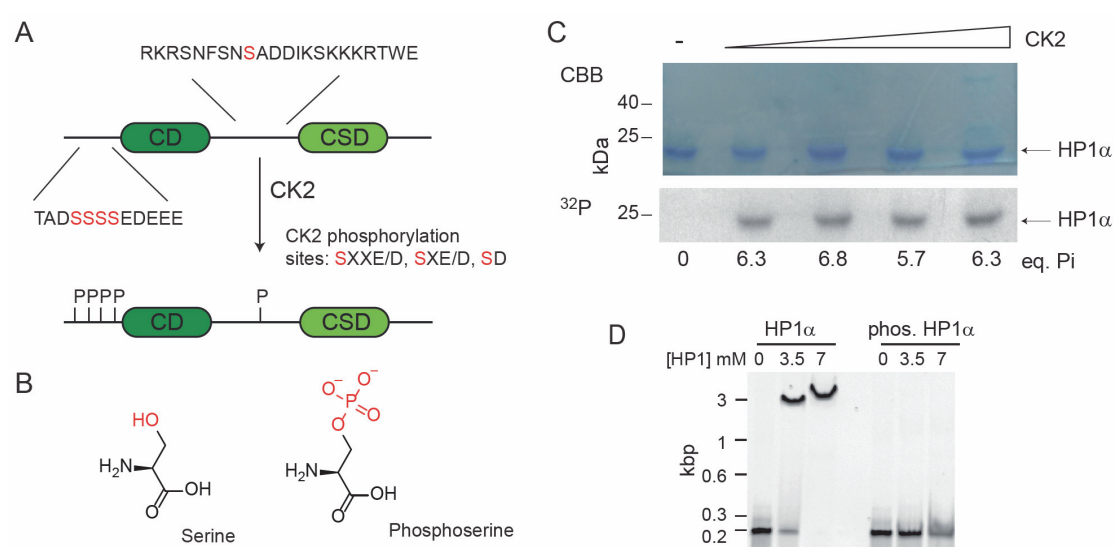


Figure 49. Phosphorylation of HP1 α . A) General scheme of HP1 α phosphorylated by CK2, serines recognized by CK2 are highlighted in red. B) Structure of serine and phosphoserine. C) CK2-mediated phosphorylation of HP1 α using [γ -³²P]-ATP for quantification. CBB: Coomassie Brilliant Blue staining, ³²P: Autoradiography. Eq. Pi is measured by scintillation counting. Data produced with Sandrine Georgeon. D) EMSA of HP1 α and phosphorylated HP1 α and a 193bp DNA piece analysed on a non-denaturing 5% polyacrylamide gel.

Phosphorylated HP1 α binding to chromatin

At the single molecule level (*Figure 50A*), the reduced DNA interaction propensity of pHP1 α resulted in two-fold slower chromatin binding compared to non-phosphorylated HP1 α (*Figure 50C*, *Table 3*). In contrast, dissociation of pHP1 α from chromatin was found to be slowed down as well, with a significant fraction of binding events (10 ± 1 %) that decayed with a time constant of $\tau_{\text{off},2} = 5.6 \pm 0.37$ s (*Figure 50B*, *Table 3*). Phosphorylation of HP1 α thus not only decreases its binding rate by reducing DNA binding, but stabilizes multivalent interactions on chromatin, possibly through conformational changes within the protein¹⁵³ and additional interactions with the H3 N-terminal tail^{74,141,152}.

4. Investigating the influence of chromatin structure and HP1 subtypes on HP1 recruitment

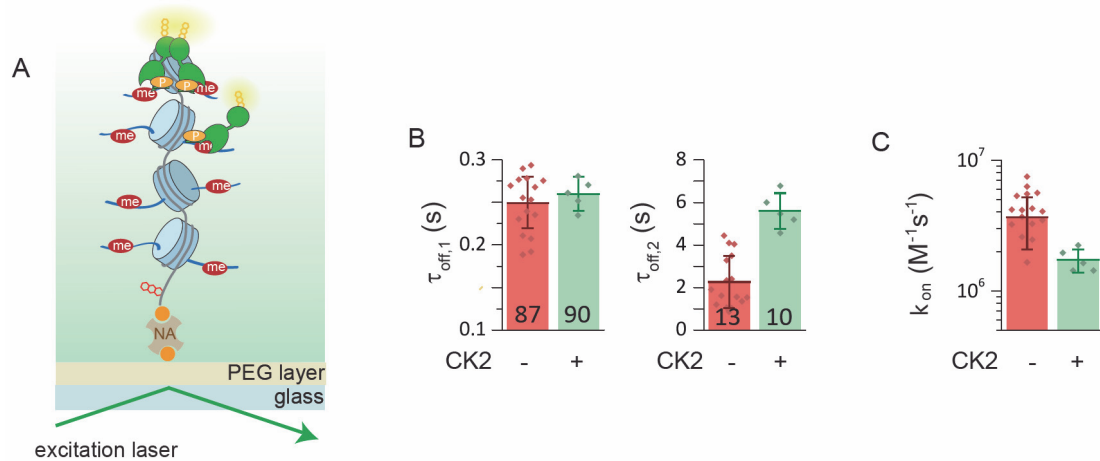


Figure 50. Phosphorylated HP1 binding to H3K9me3 chromatin. A) Schematic representation of a smTIRF experiment with 1 nM phosphorylated HP1 α -A532 and H3K9me3 chromatin bound to the surface of the coverslip through a neutravidin-biotin interaction. B) Comparison of the chromatin residence times $\tau_{off,1}$ and $\tau_{off,2}$ for unmodified (CK2 -) and phosphorylated (CK2 +) HP1 α . C) Comparison of binding rate k_{on} for unmodified (CK2 -) and phosphorylated (CK2 +) HP1 α . Error bars: s.d., $n = 4-16$ replicates, $*P < 0.05$ versus fibers of the same NRL 1 nM HP1 α , Student's t -test.

4. Investigating the influence of chromatin structure and HP1 subtypes on HP1 recruitment

Experimental system			Dissociation kinetics				Association kinetics		Equilibrium	Replicate
Chromatin	NRL	Effector	$\tau_{off,1}$ (s)	%A1	$\tau_{off,2}$ (s)	%A2	k_{on} (M ⁻¹ s ⁻¹) x10 ⁶	K _d	n	
H3K9me3	177	1 μ M HP1 α	0.25 \pm 0.03	87 \pm 7	2.26 \pm 1.22	13 \pm 7	3.64 \pm 1.56	1.16 \pm 0.54	16	
H3K9me3, 195 mM KCl	177	3 μ M HP1 α	0.19 \pm 0.03	89 \pm 4	3.32 \pm 0.61	11 \pm 4	1.10 \pm 0.19	5.10 \pm 1.25	5	
H3K9me3, 260 mM KCl	177	3 μ M HP1 α	0.14 \pm 0.01	86 \pm 4	2.97 \pm 0.71	14 \pm 4	0.36 \pm 0.03	19.24 \pm 2.46	6	
H3K9me3	177	1 μ M PhosHP1 α	0.26 \pm 0.02	90 \pm 2	5.60 \pm 0.84	10 \pm 2	1.73 \pm 0.35	2.31 \pm 0.47	5	
H3K9me3	177	5 μ M HP1 β	0.19 \pm 0.03	95 \pm 2	3.60 \pm 1.13	5 \pm 2	0.63 \pm 0.14	8.37 \pm 2.42	10	
H3K9me3	177	3 μ M HP1 γ	0.17 \pm 0.02	93 \pm 3	2.64 \pm 0.48	7 \pm 3	0.89 \pm 0.23	7.57 \pm 3.22	5	
H3K9me3	197	5 μ M HP1 β	0.22 \pm 0.02	97 \pm 2	3.78 \pm 0.23	3 \pm 2	0.96 \pm 0.11	4.84 \pm 0.79	3	
H3K9me3	197	3 μ M HP1 γ	0.15 \pm 0.01	91 \pm 3	2.17 \pm 0.5	9 \pm 3	0.87 \pm 0.08	8.19 \pm 2.13	6	

Table 3. Kinetic parameters of HP1 α , HP1 β and HP1 γ interaction dynamics.
n is the number of replicates.

4.2.4. *In vivo* dynamic binding of HP1

We then wondered how DNA interactions, modulated by phosphorylation, affect HP1 α dynamics in cells. We thus performed FRAP experiments for wild type HP1 α (fused to the monomeric fluorescent protein mEos3.2 via its N-terminus) and two mutant proteins: one construct corresponded to the previously used hinge-mutant, devoid of DNA binding affinity. To probe the *in vivo* effect of HP1 α phosphorylation, we produced a second HP1 α construct where all four serines in the NTE were mutated to alanine (AAAA), thus preventing NTE phosphorylation. Mouse NIH 3T3 fibroblasts were transfected with the three mEos3.2-tagged HP1 α variants.

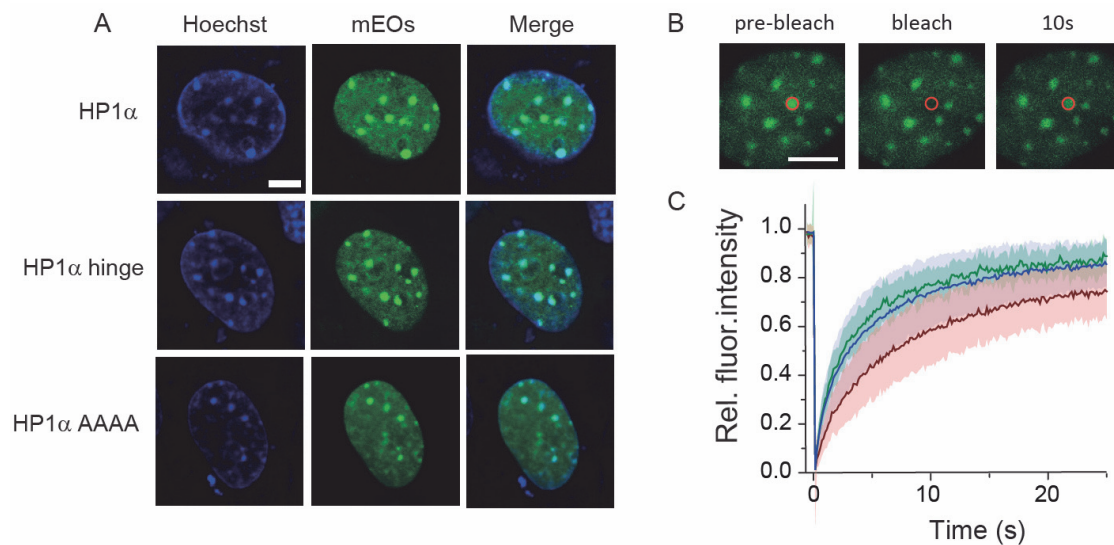


Figure 51. *In vivo* dynamics of HP1 α (wild-type), HP1 α (AAAA-mutant) and HP1 α (hinge-mutant) using FRAP. A) Confocal fluorescence images of mouse NIH 3T3 cells transfected with mEos3.2-HP1 α , mEos3.2-HP1 α (AAAA) or mEos3.2-HP1 α (hinge mutant) and overlayed with Hoechst staining. Scale bar, 5 μ m. B) FRAP experiment with mEos3.2-HP1 α showing dynamic recovery within 10 s. Scale bar: 5 μ m. C) FRAP analysis for HP1 α (wild-type, red), HP1 α (AAAA-mutant, green) and HP1 α (hinge-mutant, blue) demonstrating decreased chromatin binding for the mutant proteins. Exponential fits to the FRAP data resulted in a recovery time constant of 8.1 ± 0.7 s for HP1 α , a recovery time constant of 4.8 ± 0.6 s for HP1 α (AAAA-mutant) and a recovery time of 5.1 ± 0.5 s for HP1 α (hinge-mutant). Errors: s.d.

All constructs displayed heterochromatin localization (Figure 51A). FRAP measurements targeting heterochromatin foci revealed an increased mobility for both the hinge-mutant HP1 α (Figure 51C, blue trace) as well as for the AAAA-mutant HP1 α (Figure 51C, green trace), as compared to wild-type HP1 α (Figure 51C, red trace). Together, these findings correlate well with our *in vitro* findings that demonstrate the importance of DNA interactions, but also indicate the compensatory effect of NTE phosphorylation. The effects of hinge- or NTE-mutations on

4. Investigating the influence of chromatin structure and HP1 subtypes on HP1 recruitment

HP1 α dynamics are however markedly smaller than mutations disrupting HP1 α dimerization⁹⁸. The latter mutation drastically reduced chromatin retention (i.e. the while still retaining heterochromatin localization. This is in agreement with the importance of multivalent interactions for the organization of HP1 α domains in the cell^{153,154}. Mutations targeting the CD finally result in complete lack of sub-nuclear targeting due to loss of any specific interactions with the chromatin landscape⁷⁶. Together, these experimental results strengthen the hierarchy of interactions observed in the kinetic model for HP1-chromatin interactions, where HP1 dimerization is a key parameter governing chromatin recruitment, driven by DNA interactions, whereas histone PTM binding is responsible for targeting to heterochromatin sites.

4.2.5. Kinetic modelling of HP1-chromatin interaction network

In collaboration with Daniel Weilandt from the Laboratory of Computational systems biotechnology, EPFL the detailed mechanism of HP1-chromatin binding dynamics was modelled (*Figure 52*). The kinetic model of HP1 consisted in taking all possible interactions between HP1 and chromatin, X is the monomeric state of HP1, Y is the dimeric state of HP1, 0 is the unbound state, 1 is protein-DNA interaction and 2 is protein-H3K9me3 interaction:

- HP1 α monomeric unbound (X^0)
- HP1 α monomeric – DNA (X^1)
- HP1 α monomeric – H3K9me3 (X^2)
- HP1 α dimeric – unbound DNA (Y^{00})
- HP1 α dimeric – 1x DNA (Y^{01})
- HP1 α dimeric – 2x DNA (Y^{11})
- HP1 α dimeric – 1x H3K9me3 (Y^{02})
- HP1 α dimeric – 2x H3K9me3 (Y^{22})
- HP1 α dimeric – DNA and H3K9me3 (Y^{12})

The model was also designed to include possible migrations between binding sites, occurring when the DNA-bound protein slides or hops along the DNA and then binds to H3K9me3. Migration from monovalent to bivalent bound states as well as from DNA bound states to PTMs and vice versa. It is assumed that the free energy difference of binding to a single site is the same for monomers ($K_{0|1}$ or $K_{0|2}$) and dimers ($K_{00|01}$ or $K_{00|02}$), where $K_{0|1} = K_{00|01}$ and $K_{0|2} = K_{00|02}$.

4. Investigating the influence of chromatin structure and HP1 subtypes on HP1 recruitment

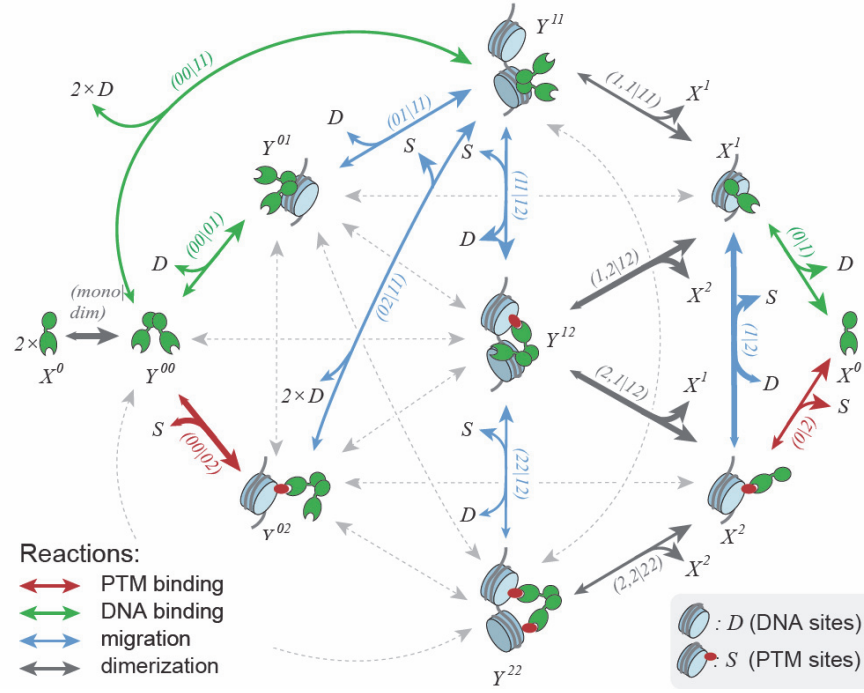


Figure 52. Kinetic model of HP1a binding. Full kinetic model of HP1-chromatin interactions, showing the pathways associated with high flux (arrow thickness). Gray arrows denote reactions associated with low but non-zero flux. Unbound states are labeled ‘0’, DNA bound states ‘1’ and H3K9me3 bound states ‘2’. Double-headed arrows indicate reversible reactions. Arrowhead size indicates the direction of net flux.

The model output was optimized by using a genetic multi-objective optimization algorithm^{155,156} with the combined single molecule data from all HP1 subtypes. Genetic algorithms are based on the process of natural selection, where a randomly generated population evolves through 3 operations: selection (close-fitting individuals to the objective function are selected), recombination (new individuals are created) and replacement (next generation individuals are created through the replacement operation). In this case each experiment is assigned to an objective function that compares dissociation times (τ_{loff} and τ_{loff}), relative amplitudes and the equilibrium value of absorbed protein to the experimental results. Parameters for the model were taken from the median of the population obtained from the optimization algorithm.

The deterministic parameter estimation was then verified by stochastic simulation¹⁵⁷, by transferring the rate equations into propensities. To evaluate the stochastic simulations, t_{bright} and t_{dark} were determined for a single chromatin array with 24 H3K9me3 binding sites and 120 DNA binding sites (Figure 53A). Cumulative histograms were reconstructed (Figure 53B and C) without binding times lower than 0.05 s since these were not measured in smTIRFM since

4. Investigating the influence of chromatin structure and HP1 subtypes on HP1 recruitment

exposure time was set at 50 ms, which allowed a direct comparison with the experimental single molecule data. Several observations were made; the predominant binding pathways involved DNA bound states. Individual observable binding events were composed of multiple rapid transitions between H3K9me3 and intrinsically short-lived DNA bound states. Simulating HP1 interaction kinetics without multivalent binding did not produce bi-exponential kinetics, the slow (τ_{off}) kinetic phase, whereas inclusion of multivalency gave rise to a population HP1 molecules engaged in long-lived interactions. Slow binding times correlate to multivalent binding interactions of HP1. The model was then used to determine the influence of DNA and H3K9me3 interactions on the overall recruitment kinetics of HP1 (*Figure 53D and E*). The apparent association rate constant (k_{on}) and the dissociation rate constant ($k_{\text{off}} = 1/\tau_{\text{off},1}$) were determined from changing either the equilibrium constant for H3K9me3 (K_{PTM}) or the equilibrium constant for DNA binding (K_{DNA}). The association rate constant was found to be more sensitive to changes in K_{DNA} , whereas HP1 retention on chromatin depended more strongly on K_{PTM} .

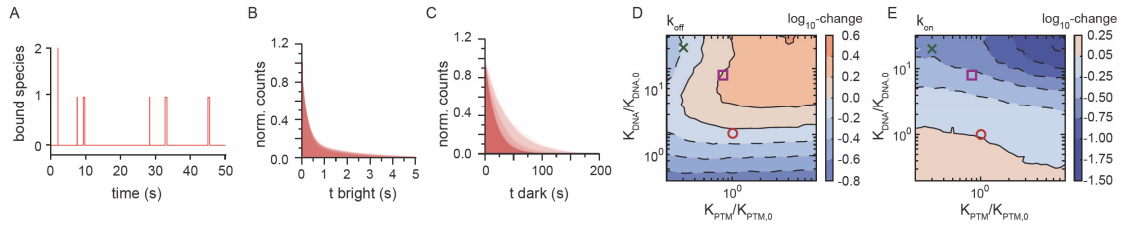


Figure 53. Kinetic modeling using stochastic simulations of HP1 binding to chromatin. A) Reaction trace from stochastic simulation based on the model shown in Figure 52 indicating binding and dissociation dynamics of HP1. B) Overlay of cumulative histograms for HP1 dwell times obtained from stochastic simulations using the best ranked parameter sets. C) Overlay of cumulative histograms for HP1 unbound (dark) times obtained from stochastic simulations using the best ranked parameter sets. D) Dependence of simulated HP1 dissociation rate constants ($k_{\text{off}} = 1/\tau_{\text{off},1}$) on relative changes in K_{PTM} and K_{DNA} . Parameters for O: HP1 α , X: HP1 β , \square : HP1 γ . The colour code and contour lines indicate changes in the dissociation rate on a logarithmic scale. E) Dependence of simulated HP1 binding rate constants (k_{on}) on relative changes in K_{PTM} and K_{DNA} interactions. Parameters for O: HP1 α , X: HP1 β , \square : HP1 γ . The colour code and contour lines indicate changes in the binding rate on a logarithmic scale. Data produced by Daniel Weilandt.

A global sensitivity analysis¹⁵⁸ was performed to quantify the impact of a parameter on the model output (*Figure 54*). The defined output parameters were: bound HP1 concentration, the two apparent dissociation time constants and the percentage of the amplitude of the slow dissociation process (A2). The analysis was performed on all the model parameters by varying the forward and reverse rate constants for each reaction. The total HP1 concentration and the microscopic rate constants governing binding to DNA and to H3K9me3, HP1 dimerization and a number of internal migration pathways were found to be key determinants for chromatin

4. Investigating the influence of chromatin structure and HP1 subtypes on HP1 recruitment

retention. From this, predictions on how HP1 binding dynamics may change in a cellular environment can be made. For example, increasing the local HP1 concentration results in more chromatin bound protein.

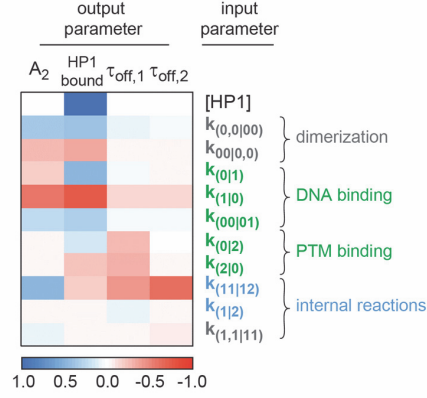


Figure 54. Global sensitivity analysis of HP1 binding to chromatin. The heat map denotes the average order of magnitude change of the indicated model output with respect to the set of most sensitive model parameters, blue indicates correlation of parameter and output, red indicates anticorrelation. Data produced by Daniel Weilandt.

Cellular proteins that stabilize HP1 dimerization increase the chromatin bound population and prolong the residence times by inducing multivalent states. However, an increase in migration reaction rates, that can occur from local competition in the nucleus or active mechanisms such as chromatin remodelling, will provide dissociation pathway and thereby faster HP1 release times. In conclusion, the combination of DNA and PTM interactions are responsible for chromatin targeting, as DNA binding has strong effects across all parameters, whereas histone PTM binding provides specificity for heterochromatic regions.

4.3. Conclusion

This chapter was focused on probing the relative influences of spatial and chemical features in chromatin on the interaction dynamics of the HP1 family proteins. I compared chromatin of different architecture; in either an open (with linker lengths of 30 or 50 bp and addition of H4Ks16ac) or a compact conformation (induced by a linker histone). We observed that HP1 α prefers a compact fiber state, due to an increase in multivalent interactions. In agreement, linker histones are abundant in heterochromatic regions¹⁵⁹. HP1 α has been reported to increase chromatin compaction upon binding⁶⁹. This results in a positive feedback, which further stabilizes HP1 α association to heterochromatin. Conversely, in embryonic stem cells, where chromatin adopts a globally open state, HP1 dynamics have been found to be markedly

4. Investigating the influence of chromatin structure and HP1 subtypes on HP1 recruitment

increased¹⁶⁰. Chromatin conformation is thus a direct modulator of multivalent effector interactions. The observed sensitivity to chromatin structure for HP1 α was however smaller compared to the linker-DNA sensitivity of the *S. pombe* HP1 ortholog Swi6⁶⁷, which shows a strong increase in H3K9me3-specific binding for short linker-DNA lengths. The preference of Swi6, for short linker-DNA can be rationalized as *S. pombe* exhibits much shorter NRLs as compared to mammalian cells.

Combined single-molecule experiments comparing all three human HP1 subtypes, together with computational modelling further allowed us to generate a detailed picture of the dominant chromatin interaction pathways. In this dynamic capture model, the most common HP1 recruitment and retention pathways involve charge-dependent DNA interactions, which increase the capture radius for specific sites (i.e. H3K9me3 modified nucleosomes). This situation, where lower-affinity interactions guide an effector protein to its molecular target are reminiscent to the target search of transcription factors¹⁶¹. From initial short-lived dynamic encounter complexes, HP1 molecules can transition into states involving more long-lived PTM-based interactions, either mono-, bivalent or mixed states where DNA and PTMs are simultaneously engaged. Moreover, DNA interactions enable rapid transitions between neighbouring nucleosomes, facilitating rapid re-binding after dissociation from H3K9me3. Here, we demonstrate that reducing the strength of charge-based interactions directly lowers the probability of H3K9me3 binding. Simultaneously the residence times of HP1 proteins is decreased as re-binding reactions are disfavoured. For this reason, the HP1 β and HP1 γ isoforms both exhibit slower binding and reduced chromatin retention in comparison to the HP1 α isoform, in spite of their higher affinity for H3K9me3. The molecular properties of HP1 proteins are modulated by various PTMs⁷². Examples include HP1 β phosphorylation at T51, which is important during initiation of the DNA damage response¹⁶², or S83 phosphorylation of eukaryotic HP1 γ ¹⁶³. Moreover, both HP1 α and HP1 β are phosphorylated throughout the cell cycle¹⁶⁴. The key phosphorylation sites in HP1 α involve serine residues in the NTE, disrupting DNA binding but strengthening H3K9me3 interactions^{74,141}. In our kinetic assays, we demonstrate that phosphorylated HP1 α can not only compensate the loss in DNA binding by its higher affinity for the H3 peptide⁷⁴, but even demonstrates increased chromatin retention, possibly involving further specific mechanisms. Importantly, NTE-phosphorylation has been implicated in phase-separation behaviour^{153,154}, involving conformational changes of the HP1 α dimer as well as interactions beyond the dimer. PTMs are thus clearly a critical mechanism for the cell to both regulate local dynamics as well as emerging behaviour over larger spatial scales.

4. Investigating the influence of chromatin structure and HP1 subtypes on HP1 recruitment

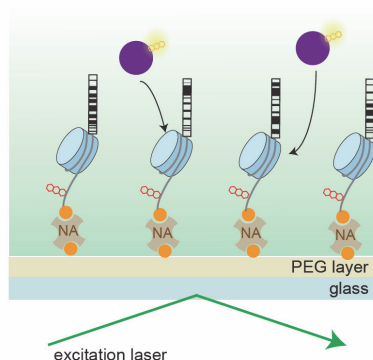
Taken together, we have gained insight into the mechanisms of chromatin interaction by multivalent effectors. Importantly, we have determined a key function of helper interactions via the DNA in target search and chromatin retention for effector proteins. We propose that this is a general paradigm for chromatin associated proteins. Effectors are transiently trapped by multiple moderate affinity interactions, and sequential dissociation and rebinding reactions result in effector accumulation in the high-avidity environment of chromatin. Such a dynamic capture mechanism enables a fast response to changes in the local environment or cell state^{79,162}. It further predicts that the interaction kinetics of effectors with chromatin depend on both the multivalency properties of effectors and the structural features of the chromatin fiber, modulating the local concentration of binding sites. Indeed, protein subdomains or regions conferring DNA or general nucleosome binding properties are commonly encountered among chromatin effectors, e.g. in SUV39H1¹⁶⁵, PRC1^{166,167}, PRC2^{168,169} or BRDT¹⁷⁰, in addition to specific PTM reader modules. These interactions are thus required for initial chromatin localization of effector complexes, whereas specific histone PTM recognition directs their accumulation in target chromatin domains.

5. Single molecule multiplexed detection of nucleosomes

5.1. Background and overview

The previous chapters described a single molecule technique to study binding between an effector protein, Heterochromatin protein 1, and synthetically modified chromatin. These measurements enabled us to gain insight into the kinetic binding of HP1. Our next goal was to further develop our single molecule TIRF system to allow protein multiplexing. In its current implementation, for each microscopy channel we could only probe the interaction of the effector protein towards one type of chromatin containing A647N-labeled DNA. For example, when we wanted to compare HP1 binding kinetics to different chromatin fibers (i.e. H3K9me3 and H3K9me3 & H4K16ac), measurements were performed consecutively in 2 different channels with each channel containing one sort of chromatin fiber. However, to compare the protein kinetic binding to different types of chromatin, we aimed to develop a multiplexing technique where the interaction of one protein to many different types of chromatin fibers could be read out in one single molecule experiment. As well as an inherent increase in experimental throughput, there would be no variation in protein concentration which could otherwise take place from one channel to the next, thereby providing better relative values, especially with the association rate constant which is usually difficult to define when there are a low numbers of binding events.

Step 1. Protein multiplexing



Step 2. Barcode read-out

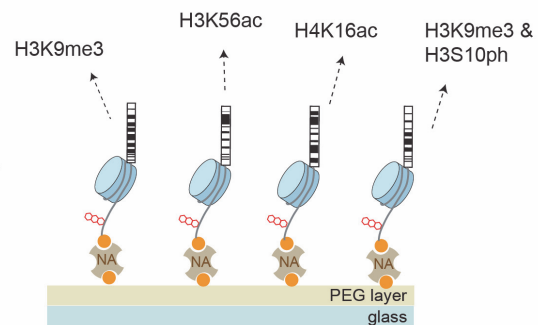


Figure 55. General strategy for single molecule multiplexing. In a first step, protein binding to a library of barcoded nucleosomes is imaged. In a second step, the barcodes are read-out to correlate each barcoded-nucleosome to its modification state.

To measure the interaction of a protein to different chromatin fibers, one solution would be to use a dye for each type of chromatin fiber, however this is not possible for $n > 3$ owing to spectral limitations (*Figure 15 and Figure 16B*). Our solution was to fuse a readable tag to the nucleosomal DNA, such as a barcode (*Figure 55*). When the barcode is read out, it provides the modification state of the nucleosome. With this method, different synthetically modified octamers are prepared and folded into chromatin with barcoded DNA. The dynamic binding of a protein of choice is then measured at the single molecule level and finally the barcode is read-out to provide the modification state of each nucleosome.

The barcoding strategy used in this project was derived from the points accumulation in nanoscale topography (PAINT) technique¹⁷¹. Originally, PAINT was developed to improve subdiffraction imaging by targeting the surface of vesicles with fluorescent probes diffusing in solution¹⁷¹. PAINT technique was further optimized by fluorescently labeling oligonucleotides. The use of ssDNA pieces provides high specificity owing to specific binding to its complementary strand. It was shown that its dynamic binding and dissociation towards the complementary single stranded docking strands protruding from DNA nanostructures could be measured in TIRFM¹⁷² (similar to our single molecule technique). Finally, exchange-PAINT¹⁷³, utilizes the DNA-PAINT technology, where super-resolution imaging is used with transient programmable binding between the fluorescently labeled DNA oligonucleotides and the complementary docking strands with sequential imaging rounds. This allows multiplexing independent on the dye spectra since the same dye can be used for each imaging round.

The barcode we developed for the nucleosomal DNA is derived from the DNA-PAINT technique where single stranded labeled DNA, the **decoder**, diffuses in the channel and specifically binds to its complementary strand, the **template**. We decided to provide a nucleosomal DNA piece with the addition a single stranded site(s), to which a labeled 10-mer oligonucleotide can specifically hybridize. The decoders are either labeled with Atto532, Alexa488 or with both dyes. In this way, in one imaging round the three decoders are imaged at once with alternate switching between the 532 nm excitation laser or 488 nm excitation laser (*Figure 56*). In each round we are therefore limited by three different decoders (x, y, z), however, single stranded sites can be joined and once the decoders are washed out, a new set of decoders can be infused and bind to the second “layer” of the barcode (*Figure 56*). With this method, we are no longer limited by the dyes of each nucleosome but by the number of different sequences provided by combinations of nucleic acids since the decoders are washed out and replaced by a new set of decoders.

Initially, to develop this strategy, we decided to use 6 different decoders with the first layer providing binding sites for x1, y1 and z1 and the second layer providing binding sites for x2, y2, z2. Their combination provides a library of 9 different templates (*Figure 56*).

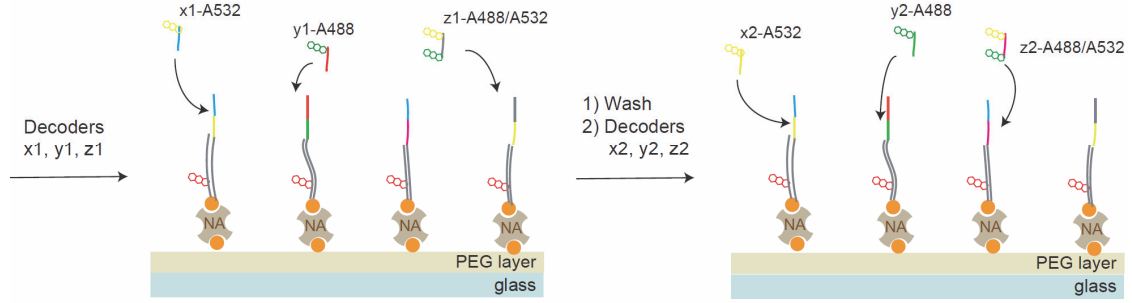


Figure 56. Example of a single molecule decoding experiment. The first set of decoders (x1-Atto532, y1-Alexa488 and z1-Atto488/A532) are injected into the channel and their dynamic binding to the complementary strand is measured. The decoders are washed out and a second set of decoders is added (x2-Atto532, y2-Alexa 488 and z2-Atto488/A532).

5.1.1. General experiment

For a full multiplexing experiment, the strategy consists in the following steps: First of all, a library of octamers is refolded from chemically modified histones. In parallel, nucleosomal DNA with the addition of a barcode is prepared by PCR amplification and purification, where one primer provides both biotin and Atto647N and the other primer the complementary sequence to the single stranded barcode with the thymines replaced by uracils. Histone octamers are then wrapped into the DNA encoding for their specific modification state. Using single molecule TIRF microscopy, the dynamic interactions of a chromatin interaction factor is measured towards the library of nucleosomes. The barcodes are then read-out, for this, the octamers and the chromatin interaction factor are washed out with a high salt-containing buffer. Then, to unmask the ssDNA barcodes for decoding, the complementary strand, containing uracils is enzymatically digested with a USER enzyme (Uracil-specific excision reagent). Decoders are then added in several rounds with thorough washing steps in-between. The data for protein dynamic binding and decoding is then analysed using Matlab.

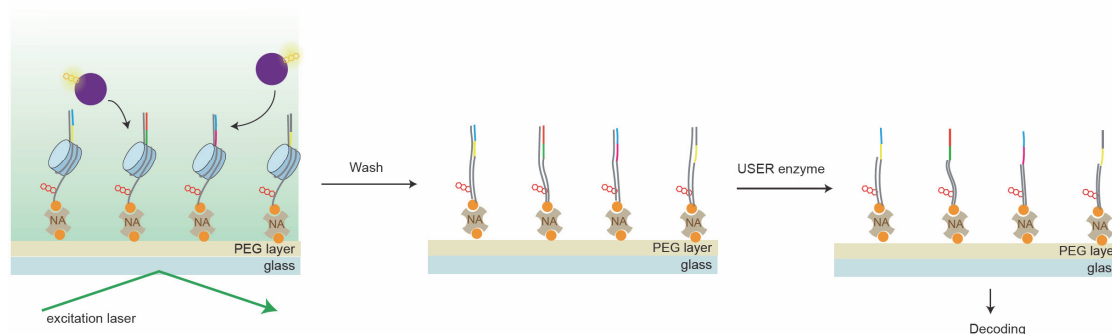


Figure 57. General single molecule multiplexing strategy. In a first step dCas9-Alexa568 binding to the library is measured. The octamers are then washed out followed by the addition of the USER enzyme that cleaves off the complementary strand, liberating the template for decoding.

5.2. Results and discussion

5.2.1. Development of the decoding system

Decoders

The initial focus of the project was to find suitable single stranded DNA pieces that could hybridize efficiently in our single molecule TIRF system. The buffer conditions were optimized to provide hybridization without unspecific binding to the coverslip surface or to other templates, by adding BSA, varying the salt concentration, amounts of glycerol and tween. Different sequences were assessed depending on their residence times and specificity to their complementary sequence, from these, 9 optimal sequences were chosen (*Table 4*) for decoding experiments. Initially, 9-mer oligomers were considered, however the residence times were low (< 1 s). We therefore chose to use 10 base decoders which provide longer binding times (1- 8 s, *Figure 59A-F*)¹⁷².

Decoder	Sequence
x1	Atto532-TAG ATG TAT T
x2	Atto532-ATC CTA ATT A
y1	Alexa488-TAT CAC TAA T
y2	Alexa488-TAC TAC ATT T
z1	Atto532-ATA CTC AAT T-Alexa488
z2	Atto532-TTA GTG ATA T-Alexa488

Table 4. Sequences of the 9 decoders. x1, y1, x2 and y2 all contain a modified amine, whereas z1 and z2 contain an amine and a thiol group for dual labeling.

The decoders were ordered to contain an amine at the 5' end. These single stranded pieces were either labeled with Atto532 NHS ester (in the case of x1 and x2) or Alexa488 TFP ester (in the case of y1 and y2). The dual-labeled decoders (z1 and z2) were ordered with an amine at the 5' end and a thiol at the 3' end and were labeled with Alexa488 maleimide and Atto532 NHS ester. Once labeled, the single stranded DNA pieces were purified by RP-HPLC on a neutral pH stable column using trimethylamine/acetic acid as buffer (*Figure 58A-F*) and lyophilised.

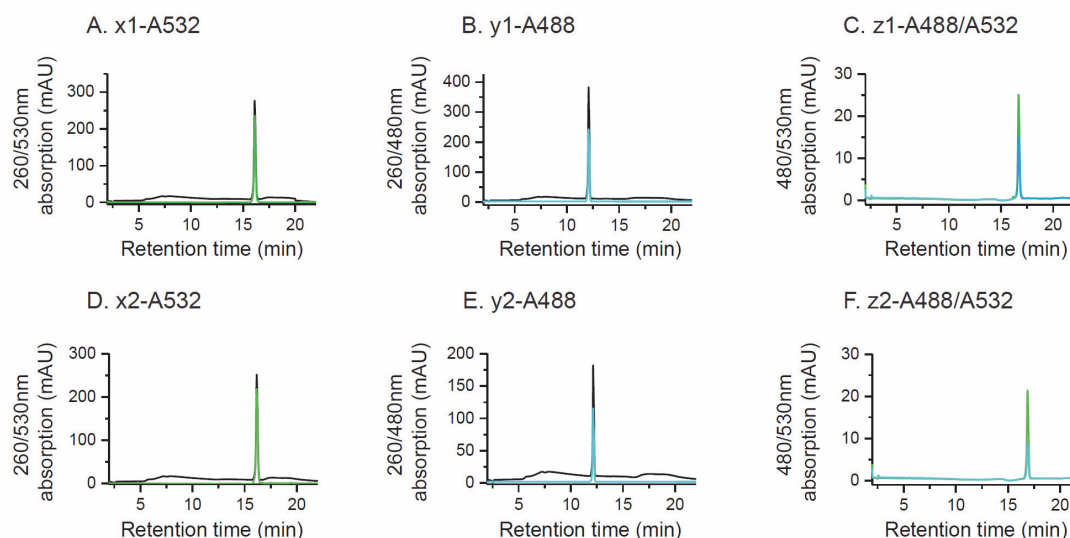


Figure 58 *Chromatograms from RP-HPLC analysis of final purified oligonucleotides. A) x1-A532, B) y1-A488, C) z1-A488/A532, D) x2-A532, E) y2-488 and F) z2-A488/532.*

Single molecule hybridization kinetics

To test the binding efficiency of the decoders, templates were prepared by annealing a ssDNA with A647 and biotin to a longer ssDNA piece that provides ssDNA hybridization sites for the decoders. The hybridization dynamics were measured at the single molecule level. 100 pM of the template DNA were injected into the neutravidin treated flow chamber for 5 min and then washed out. Template coverage was observed in TIRF microscopy by fluorescent emission in the far-red channel upon excitation by a 640 nm laser line. Decoding experiments were initiated by the infusion of one decoder in imaging buffer at a concentration of 5 nM. In order to measure the DNA dynamics, the 488 nm and the 532 nm laser lines were used for excitation and the emission observed in the green or yellow/orange channel respectively with an EMCCD camera at 5 frames/s over an area of 25 x 50 μm with a resolution of 160 nm/pixels over 5000 frames (around 15 min). Every 200 frames, an image of the template in the far-red channel was recorded to correct for drift correction. The movies of decoder-template hybridization were then analysed. First of all, the movies were converted into TIF format and

the first 200 frames were removed in ImageJ to eliminate the first frames where there is a higher background level. A semi-automated Matlab script was then used to make a global baseline-correction and drift-correction, individual chromatin array positions were determined using a peak-finding algorithm from the far-red images. Fluorescence intensity traces (*Figure 59*) for each chromatin position were obtained by integrating over a circle of 2 pixel radius (=320 nm). Individual decoder fluorescence peaks were included based on point-spread-function (PSF) and distance cutoffs. Kinetics were extracted from fluorescence traces using a semi-automated thresholding algorithm. Cumulative histograms were constructed from dark and bright intervals and fitted to sums of mono-exponential functions in both cases (*Figure 59, Equation 11*).

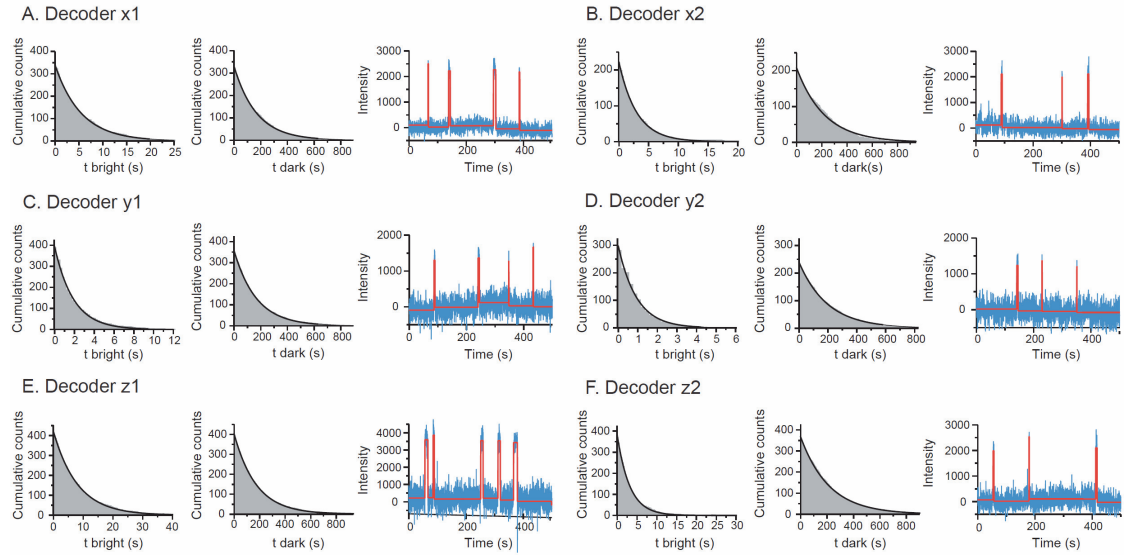


Figure 59. Cumulative histogram of t_{bright} and t_{dark} fitted with mono-exponential function and representative traces of hybridization over 500 s. A) Decoder x1: $t_{\text{off}}=5.49$ s, $t_{\text{on}}=168.79$ s, B) Decoder x2: $t_{\text{off}}=3.00$ s, $t_{\text{on}}=221.44$ s, C) Decoder y1: $t_{\text{off}}=1.90$ s, $t_{\text{on}}=167.26$ s, D) Decoder y2: $t_{\text{off}}=0.94$ s, $t_{\text{on}}=196.50$ s, E) Decoder z1: $t_{\text{off}}=8.15$ s, $t_{\text{on}}=173.37$ s, F) Decoder z2: $t_{\text{off}}=3.17$ s, $t_{\text{on}}=214.58$ s.

5.2.2. Multilayer multiplexing

Nucleosomal barcoded DNA

Once the set of 6 decoders was determined, the next step was to read out a set of barcodes on nucleosomal DNA. Nucleosomal DNA was prepared by a PCR reaction on a plasmid containing the 1x 601 Widom sequence¹²⁹. One primer containing a biotin and an amine modification (5'-Biotin-CGC ACA CTG T(amine linker)GC CAA GTA CTT AC) was labeled with A647N followed by RP-HPLC purification and the other primer contained uracils so that nucleosomes could be properly reconstituted and cleaved off to provide the single

stranded DNA for decoding (Table 5). After PCR amplification, the DNA strand was purified and ethanol precipitated and the pellet resuspended in water.

Template	Sequence
X1X1	UAGAUGUAUUUAUCCUAAUUACGCGU TTGAGACCAAGTACTCC
X1Y2	UAGAUGUAUUACUACAUUUCGCGU TTGAGACCAAGTACTCC
X1Z2	UAGAUGUAUUAGUGAUUAUCGCGU TTGAGACCAAGTACTCC
Y1Z2	UAUCACUAAUUAGUGAUUAUCGCGU TTGAGACCAAGTACTCC
Y1X2	UAUCACUAAUAUCCUAAUUACGCGU TTGAGACCAAGTACTCC
Y1Y2	UAUCACUAAUACUACAUUUCGCGU TTGAGACCAAGTACTCC
Z1X2	AUACUCAAUUAUCCUAAUUACGCGU TTGAGACCAAGTACTCC
Z1Y2	AUACUCAAUUACUACAUUUCGCGU TTGAGACCAAGTACTCC
Z1Z2	AUACUCAAUUUAGUGAUUAUCGCGU TTGAGACCAAGTACTCC

Table 5. Sequences of primers with uracils for nucleosomal DNA used for the 2-layer decoding.

Barcode unmasking

To unmask the ssDNA barcodes for decoding, the complementary strand, containing uracils is enzymatically digested with a USER enzyme. The USER (uracil-specific excision reagent) is composed of two enzymes, the *E.Coli* uracil DNA glycolase and the endonuclease VIII¹⁷⁴. The dU residues are excised from the DNA piece; the phosphodiester backbone dissociate at the 5' terminal to provide the free single stranded template at the C-terminal. All the thymines complementary to the barcode were replaced by uracils to make sure that the sequence is completely removed.

To check that the USER enzyme was working under our single molecule microscopy conditions, I prepared a double stranded DNA piece by annealing a single stranded DNA with A647N on the 5' end and biotin on the 3': 5'-U(amine linker) AU CAC UAA UAC UCA AUU AAC AGC TAG TCT GCT CAG ATA TCG TCG-3'-biotin. The double stranded DNA template was added to the channel and imaged with the 640 nm excitation laser. USER enzyme in 1x Cutsmart buffer was then added to the channel and incubated 10 min at room temperature and washed out. The channel was imaged once more and no fluorescent spots were observed corresponding to the USER enzyme cleaving off uracils at the 5' end and removing the dye (Figure 60).

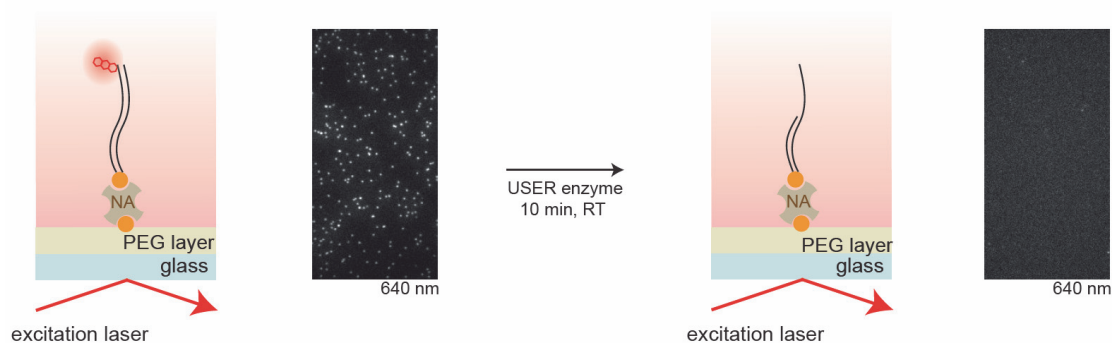


Figure 60. USER enzyme digestion test. Initially the double stranded DNA piece with Atto647N at the 5' end and biotin at the 3' was imaged. USER enzyme was then incubated with the DNA, washed out and imaged again. No fluorescent spots were observed, corresponding to the cleavage of uracils and the release of the dye.

Microfluidics system

The next step was to start decoding the templates with two rounds of decoders. However, stage drifts were observed from one decoding cycle to the next, due to manual injection of the decoders, and the same fluorescent spots could not be localized. This would also be an issue further on, since the same fluorescent spots must be imaged at each step. To prevent stage drift when injecting and washing out samples, an automated microfluidics system was set up (Figure 61). A nitrogen air flow from a tank is passed through plastic tubing to a pressure controller, connected to and controlled with a computer and coupled with a flow sensor, providing a feed-back loop to monitor the flow rate. The controlled air flow is then split to the reservoirs containing the samples. The pressure builds up in the tubes and pushes the samples through the liquid flow tubing to 2-way valves. These valves can be switched on or off and are connected to a microfluidic valve controller, itself connected to the computer. The tubes merge together at an 8-way splitter and the samples are passed through the flow sensor to a 3-way valve to either go to the microscopy slide or to the waste.

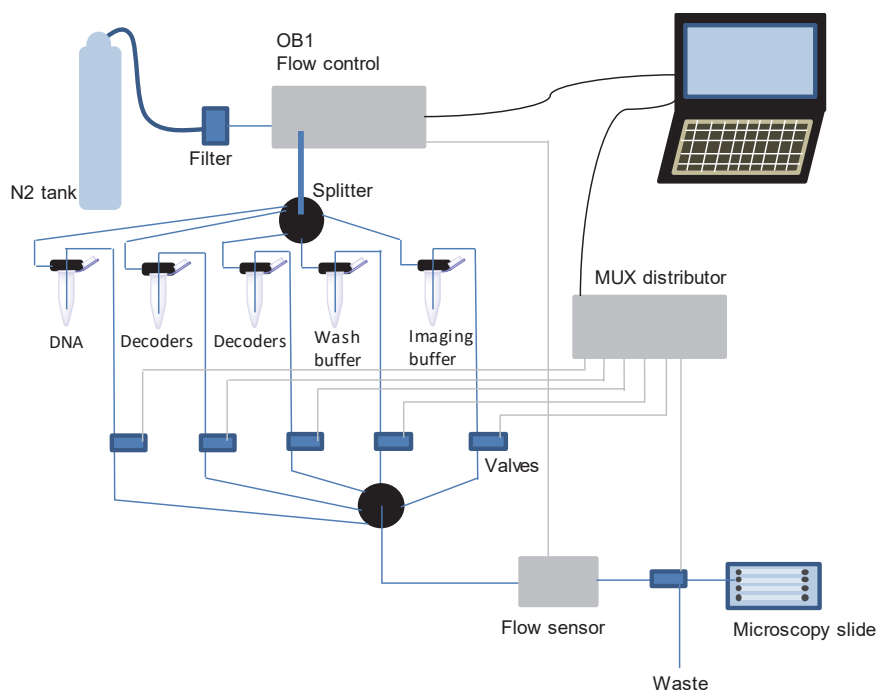


Figure 61. Microfluidics set up. The samples are placed in tubes, connected to a flow of nitrogen. The valves are switched on or off by the valve controller to control the flow from individual tubes. The flow sensor provides a feed-back measurement of the flow to control the correct flow rate. The sample then goes to a 3-way valve to either go to the microscopy slide or the waste.

Single molecule two-layer decoding

Once the microfluidic system was set up we could then proceed with a two-layer decoding of DNA templates. After PEGylation, the channels were extensively washed before proceeding to experiments. For DNA immobilization, a neutravidin solution at 0.2 mg/ml was infused using a high-precision syringe pump and incubated for 5 min, followed by extensive washes. The five tubes containing the following are connected to the microfluidics system: tube 1: 100 pM template DNA/USER enzyme, tube 2: 10 nM decoder 1, tube 3: 10 nM decoder 2, tube 4: 2 M NaCl wash buffer and tube 5: imaging buffer. First of all, the DNA templates were added into the neutravidin treated flow chamber and then washed out to remove unbound templates and the USER enzyme. DNA coverage was observed in TIRF microscopy by fluorescent emission in the far-red channel upon excitation by a 640 nm laser line. Decoding experiments were initiated by infusion of the decoders in imaging buffer. In order to measure decoder colocalizing to the templates, the 532 nm and 488 nm laser lines were used, alternating one after the other every 200 ms. Images were recorded with an EMCCD camera at 5 frames/s over an area of 25 x 50 μm with a resolution of 160 nm/pixels. Every 500 frames, an image of the chromatin positions in the far-red channel was recorded to correct for drift. Imaging was

done over 7'500 frames (25 minutes). The decoders were then thoroughly washed with 2 M NaCl. A new set of decoders was added and the same imaging procedure was done. The movies of DNA hybridization were then analysed. First of all, the movies were converted into TIF format and 488 nm and 532 nm movies were split in ImageJ. The images of the templates were then inserted every 500 frames and the movies were then background corrected. A semi-automated Matlab script was then used for drift-correction, individual chromatin array positions were determined using a peak-finding algorithm from the far-red images. Fluorescence intensity traces for each chromatin position were obtained by integrating over a circle of 200 nm. For each fluorescent spot the hybridization trace overtime is analysed. The traces are either accepted (green spot) or rejected (red spot) depending on the total integrated peaks, the distance and the point spread function (*Figure 62*).

The traces for each template were then cross-correlated to discriminate between an x decoder, y decoder or a z decoder. Individual fluorescence peaks were included based on point-spread-function (PSF), distance cut-offs and average intensity (dependent on the length and number of binding events).

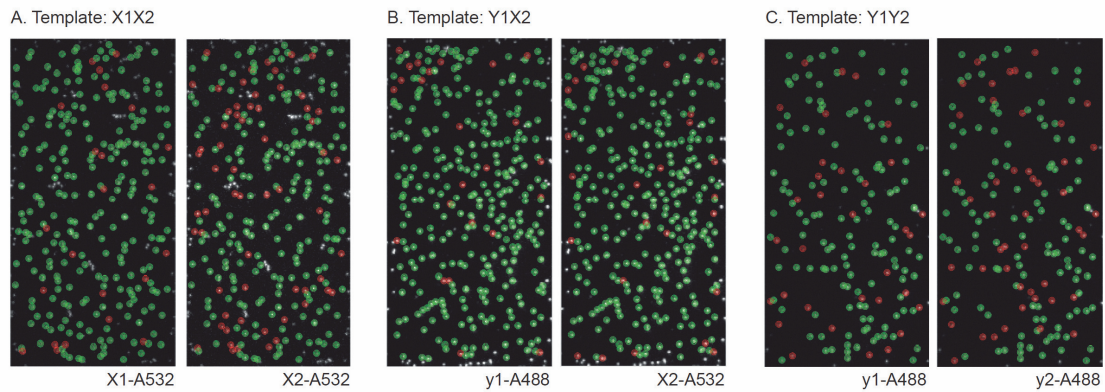


Figure 62. Two-layer multiplexing. A) Template: X1X2, left : x1-A532, right : x2-A532. B) Template: Y1X2, left : y1-A488, right : x2-A532. C) Template: Y1Y2, left : y1-A488, right : y2-A488. Green spots: the decoder binds to the template and red spots: the decoder does not bind to the template.

By individually probing the templates with two-layers of decoding after USER digest (*Figure 62A-C*) several observations can be made. In the majority of cases, when the templates were rejected (*Figure 62A-C*, red) in the first round of decoding owing to the lack of hybridization, the same templates were also rejected in the second round of decoding. This is probably the consequence of either an error in the PCR step when preparing the DNA or the USER enzyme did not free the barcode and prevented decoders from binding to the template. The proportion of hybridized templates (*Figure 62A-C*, green) is slightly lower in the second round of

decoding. The first level of decoding is on the 5' end of the template, whereas the second level of decoding is 10 bases away from the 5' with the complementary strand not completely digested by the USER enzyme.

5.3. Conclusion and Outlook

The aim of this project was to develop a multiplexed decoding strategy to read out a library of nucleosomes in TIRFM. This will enable us to measure the interaction of one protein towards a library of nucleosomes without any variation in protein concentration, thereby providing better relative values, especially with the association rate constant which is usually difficult to define when there are a low numbers of binding events.

9 different decoders were optimized to bind specifically to their complementary sequence. We were able to show that the 'two layers' of the barcode works by washing out one decoder and adding the next one with an automated microfluidic system. The next step to developing the system is to mix the DNA templates and decode them. We can then apply this method in combination with measuring the binding of a protein to a library of nucleosomes; as a proof of concept we chose to work with the DNA-binding protein Cas9 and a library of 9 different nucleosomes with different DNA sequences and either WT, H3K56ac or H2A.Z octamers. In the next paragraphs I will discuss this application and preparation of these components in more detail.

Cas9

The CRISPR (clustered regularly interspaced palindromic repeats) system was originally found in bacteria to fight off viruses by cutting foreign DNA¹⁷⁵. The system was engineered for a wider range of applications, but importantly to modify the DNA in eukaryotic cells^{175,176}; one example is the CRISPR-Cas9 from *Streptococcus pyogenes*. In order to target a specific DNA sequence, the Cas9 protein requires a single guide RNA (sgRNA), where the 5' end contains 20 bp complementary to the DNA sequence followed by a short 3 bp PAM (protospacer-adjacent motif) site on the noncomplementary DNA strand, in the case of Cas9 the PAM site is 5'-NGG-3'¹⁷⁷⁻¹⁸⁰. A single molecule microscopy study has shown the following model for Cas9 binding to DNA strands: In a first step, Cas9 is thought to search for the PAM site in a three-dimensional diffusion based mechanism. Once it has bound to the PAM site, it pushes the DNA to open and the sgRNA binds to its complementary DNA sequence to finally cleave the DNA. In vitro experiments of Cas9 cleaving nucleosomes also demonstrated the

importance of the PAM recognition site, when placed on the nucleosome positioning sequence, Cas9 was unable to cleave the nucleosomal DNA^{177,178}.

DNA sequence design

The aim is to probe the interaction of Cas9 towards nine different nucleosomes that differ in either the octamer or the position of the PAM recognition site and sequence. We chose to study 3 different octamers: unmodified octamers, octamers with the analogue of acetylated H3K56 or octamers with the histone variant H2A.Z. The PAM recognition site on the nucleosomal DNA was placed in three different positions (*Figure 63*); on the outside region of the 601 DNA, slightly in the 601 DNA and in the opposite direction. These positions were chosen such that the strong positioning sites of the 601 DNA are not hindered from binding to the octamers.

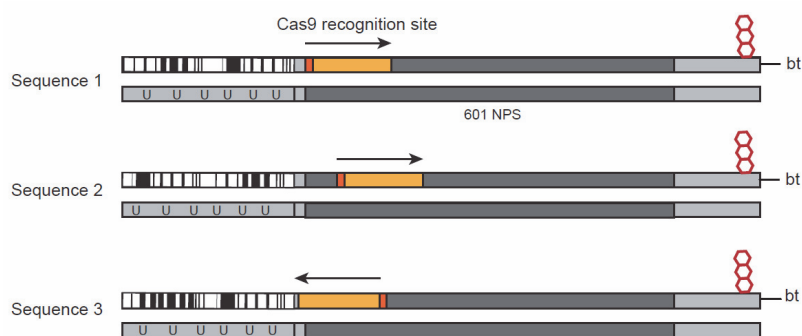


Figure 63. Schematic representation of nucleosomal DNA for Cas9 binding experiments. Orange: sequence for guide RNA hybridization, starting with the PAM sequence (dark orange). The arrow displays the direction of Cas9 binding.

H3K56ac preparation

H3K56ac is involved in nucleosome assembly during replication and enhances transcription. K56 on histone H3 is located on its first alpha helix and provides an interaction with the phosphate backbone of 10 bp of DNA at its entry-exit site¹⁸¹. Interestingly, single molecule FRET revealed that H3K56ac is sufficient to cause a 7-fold increase in DNA breathing⁴¹, owing to the loss of interaction between the H3 tail and the DNA. Therefore, if H3K56ac unwraps DNA, it might increase the likelihood for Cas9 to bind the nucleosomal DNA. H3 carrying the point mutation K56C was recombinantly expressed and purified (*Figure 64 A-C*). For the site-specific installation of the acetyl-lysine analog, H3K56C was reacted with N-vinylacetamide in the presence of a radical initiator (*Figure 64D-F*). Once the product was

5. Single molecule multiplexed detection of nucleosomes

confirmed by analytical RP-HPLC and ESI-MS, the protein was purified by semipreparative RP-HPLC and lyophilised.

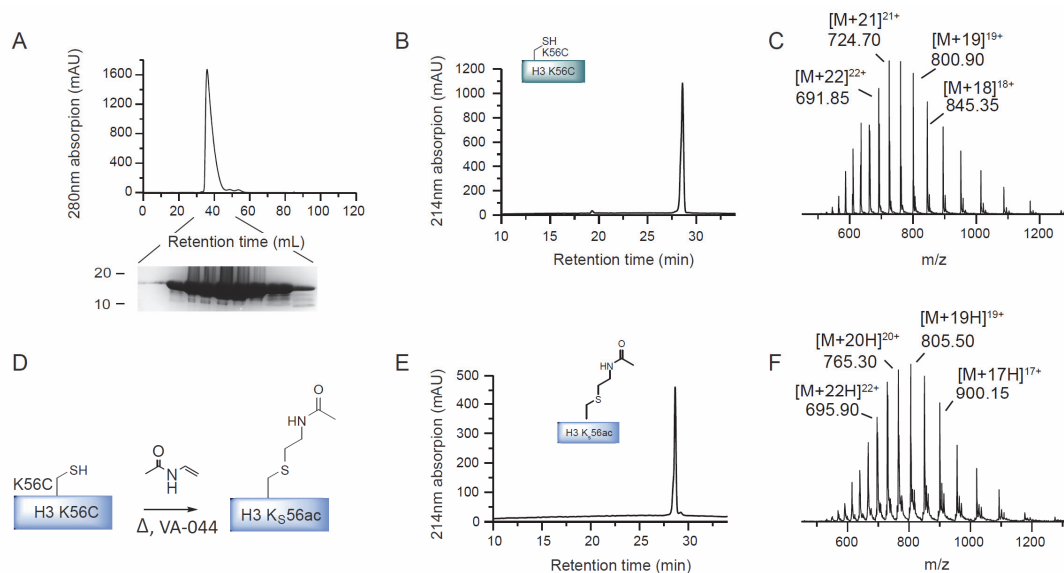


Figure 64. Preparation of H3K56ac. A) Ion exchange chromatography of H3K56C. B) RP-HPLC and C) ESI-MS analysis of purified H3K56C (calculated mass: 15200 Da, observed mass: 15198 Da). D) General scheme of the thiol-ene reaction to synthesize H3K56ac. E) RP-HPLC and F) ESI-MS analysis of the H3K56ac (calculated mass: 15285 Da, observed mass: 15285 Da).

H2A.Z preparation

The sequence of the histone variant H2A.Z is 60 % identical to the canonical H2A. The main difference is found in L1, which is important for the interaction between H2A-H2B dimers within a nucleosome. This interaction is increased with the canonical H2A. The C-terminal H2A provides a docking domain for the interaction with (H3-H4)₂ tetramer, this interaction is slightly reduced for H2A.Z owing to fewer hydrogen bond interactions. H2A.Z also influences the acidic patch; with canonical histones the H2A/H2B acidic patch is mostly provided by H2A. However, H2A.Z provides a larger acid patch and therefore a larger area for the H4 tail from the adjacent nucleosome to bind leading to a more compact secondary structure¹⁸². H2A.Z could be more resistant to dimer loss due to the stronger interaction at the L1-L1 interface, however the loss in interaction with H3 may lead to a more open nucleosome. H2A.Z can have both activating and repressive influence on transcription¹⁸³. H2A.Z was recombinantly expressed and purified (Figure 65A-C).

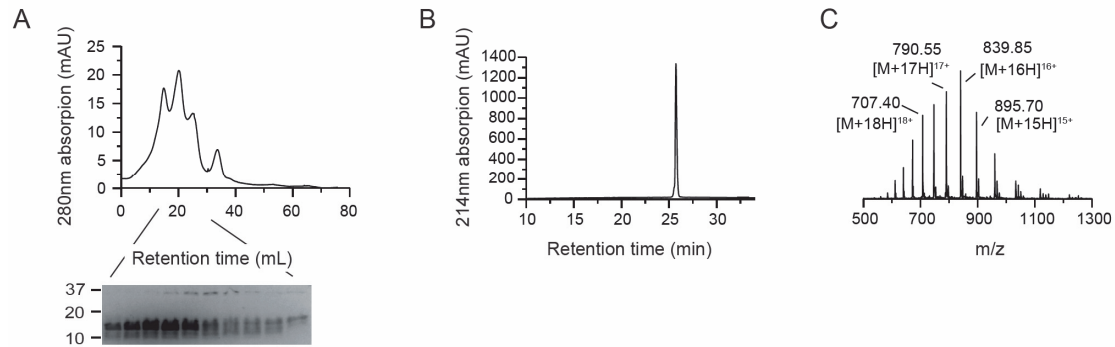


Figure 65. Purification of H2A.Z. A) Ion exchange chromatography of H2A.Z. B) RP-HPLC and C) ESI-MS analysis of purified H2A.Z (calculated mass: 13422 Da, observed mass: 13422 Da).

Cas9 in vitro assay

To check that Cas9 does bind to the DNA, Cas9 cleavage assays were performed on free DNA and nucleosomes¹⁸⁴ (Figure 66) both with the DNA sequence 1 (Figure 63). First of all, the Cas9-guide RNA complex was reconstituted by incubating Cas9 and 2.5 x excess RNA in cleavage buffer. DNA-A647N or nucleosomes containing DNA-A647N were added to the Cas9-guide RNA complex to obtain a final concentration of 200 nM Cas9, 500 nM RNA and 10 nM DNA or nucleosomes and incubated at 37°C. Samples were taken and quenched by adding EDTA and DNA-bound Cas9 was digested by Proteinase K. Samples were mixed with loading buffer and resolved on a 12.5 % polyacrylamide 7 M urea gel. Cas9 was able to cleave the free DNA and the DNA on WT nucleosomes after 15 minutes, however the guide RNA is essential for DNA cleavage (Figure 66).

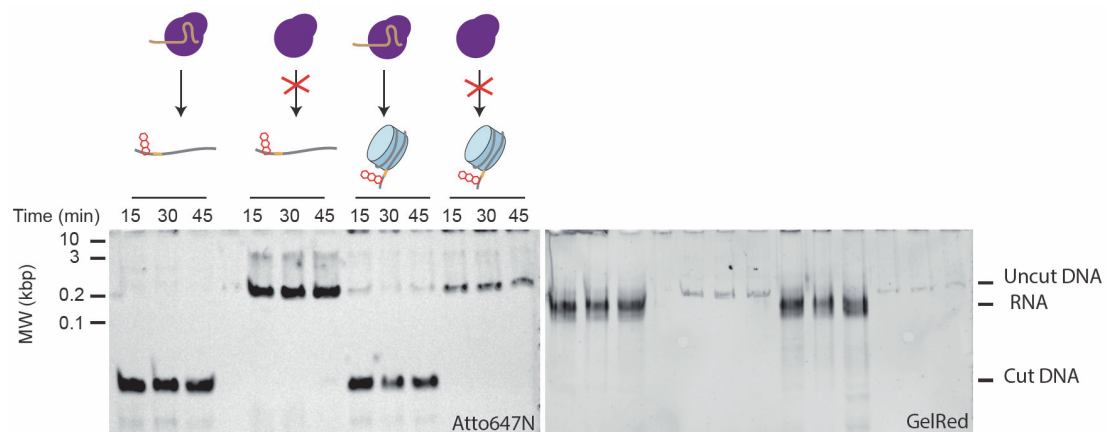


Figure 66. In vitro Cas9 cleavage assay of free DNA and WT nucleosomes. Cas9 was able to cleave the free DNA and the DNA on WT nucleosomes after 15 minutes, however the guide RNA is essential for DNA cleavage.

Cas9 labeling

Purified dCas9 containing a ybbR tag (sequence: DSLEFIASKLA) at the C-terminal was provided by Martin Jinek, University of Zurich. The protein was labelled with Alexa568 using site-specific protein labeling by Sfp phosphopantetheinyl transferase^{89,90}. In a first step, Coacetyl enzyme A was reacted 1 hour at room temperature with maleimide Alexa568 and purified by RP-HPLC. Cas9 was then enzymatically reacted with CoA-Alexa568 with SFP phosphopantetheinyl transferase (*Figure 67A*). The reaction took place at RT for 2 hours, samples from different time points were run on an SDS-PAGE to check the labeling reaction (*Figure 67B*). The labeled protein was then purified from the Sfp synthase and the unreacted CoA-Alexa568 by size exclusion chromatography (*Figure 67C*).

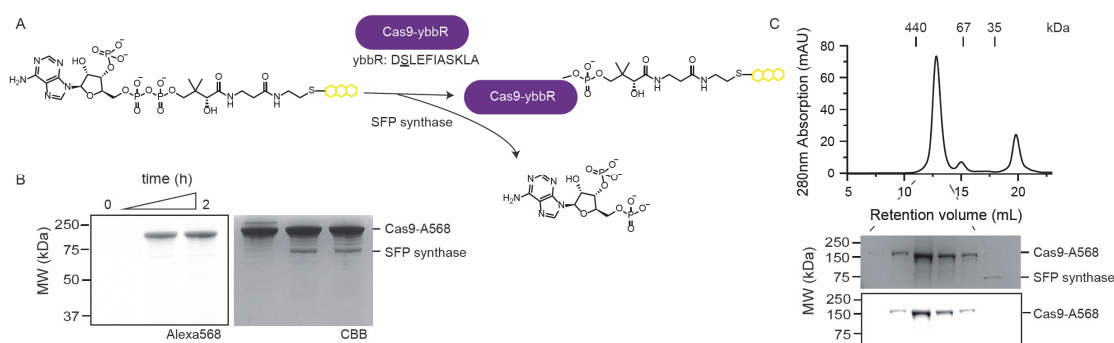


Figure 67. Cas9 labeling. A) Cas9 reaction with CoA-Alexa568 to obtain Cas9-Alexa568. B) SDS-PAGE of the labelling reaction at different time points. C) Size exclusion chromatography of Cas9-A568.

Outlook

We now have all the components in hand to study the interaction of dCas9 to a library of 9 different nucleosomes differing in the positioning site of the PAM recognition sequences and histone variants. The multiplexing technique developed in this chapter will enable us to compare the interactions of Cas9 towards different nucleosomes. So far, single molecule studies of Cas9 have only been performed on DNA and not on nucleosomes¹⁸⁰. These experiments will provide insight into the search and binding mechanism of Cas9 towards different types of nucleosomes.

6. Materials and methods

6.1. Chemicals

All commonly used chemical reagents and solvents were purchased from Sigma-Aldrich Chemical Company (Steinheim, Germany), Fischer Scientific (Fair lawn, NJ, US/Loughborough, UK) or Applichem (Darmstadt, Germany). Acetonitrile was from Lab-Scan Analytical Sciences (Sowinskięo, Poland). 2, 2'-Azobis[2-{2-imidazolin-2-yl}propane]dihydrochloride (VA-044) was purchased from Wako Pure Chemical Industries, Ltf. (Osaka, Japan) and N-Vinylacetamide from (Tokyo Chemical Industry). 76 x 26 mm slides were purchased from Thermo Scientific (Rockford, IL, US) and 24 x 40 mm coverslips from Marienfeld-Superior (Lauda-Königshofen, Germany). (3-Aminopropyl)triethoxysilane (APTES) from Acros Organics, methoxypoly(ethylene glycol) succinimidyl carbonate (mPEG) and biotinylated methoxypoly(ethylene glycol) succinimidyl carbonate (mPEG-Biotin) from Laysan Bio Inc (USA) and Secure Seal adhesive sheets from Grace biolabs (USA). Chemically competent DH5 α , Rosetta(DE3), BL21(DE3) and BL21(DE3)plysS were from Novagen (Darmstadt, Germany) and used to generate stocks of competent cells. Casein Kinase 2 (CK2), T4 DNA ligase, restriction enzymes, Phusion DNA polymerase, DNA ladders, DNA loading dyes and dNTPs were purchased from New England Biolabs (Ipswich, MA, US) distributed through BioConcept (Allschwil, Switzerland). Primers were ordered from and synthesized by Integrated DNA technologies (Leuven, Belgium). Gene sequencing was performed at GATC Biotech (Constance, Germany). Single-point mutations were done using a QuikChange II XL site-directed mutagenesis kit from Agilent (Basel, Switzerland). Atto488 maleimide, Atto532 iodoacetamide, Atto532 maleimide and Atto647N NHS ester were purchased from ATTO-TEC GmbH (Siegen, Germany), Alexa488 TFP was from Thermo Fischer. Materials for hand-casting of agarose and SDS-PAGE gels (agarose, TEMED, APS, acrylamide), analysis of SDS-PAGE gels (Precision Plus ProteinTM All blue standards and Precision Plus ProteinTM dual color standards) and pre-cast Criterion 5% TBE gels were purchased from BioRad (Hercules, CA, US). QiaQuick spin column for PCR purification, gel extraction and nucleotide removal as well as QiaPrep spin columns for miniprep plasmid purification were from Qiagen (Hilden, Germany). Slide-a-lyzer dialysis cassettes and MINI dialysis buttons were from Thermo Scientific (Rockford, IL, US). Amicon Ultracentrifugal concentration units were from Merck Millipore (Tullagreen, Ireland). Spectra/por dialysis tubing was from Spectrum laboratories Inc

(Rancho Dominguez, CA, US). Amino acid derivatives and resins were purchased from Novabiochem, Merck (Hohenbrunn, Germany). Peptide synthesis solvents and reagents were from Acros Organics (Geel, Belgium) (Dimethylformamide, dichloromethane, N,N-diisopropylethylamine and piperidine) or Protein Technologies Inc. (Tucson, AZ, US) (HBTU).

6.2. Instrumentation

Bacterial cells for recombinant protein expression were grown in an HT infors AG incubator, recovered with an Avanti J-20 XPI centrifuge from Beckman Coulter and sonicated using a Vibra-cell VCX 750 Sonics & Materials sonicator. Size exclusion chromatography and ion exchange purification was performed on an AKTA Pure FPLC system from GE Healthcare. Size-exclusion were done using a S200 10/300GL or S75 10/300 column from GE Healthcare. Cation exchange and anion exchange purification was done using HiTrap SP HP (5 ml) and HiTrap Q FF (1 ml) traps from GE Healthcare. Analytical reversed-phase HPLC (RP-HPLC) was performed on an Agilent 1260 series instrument with an Agilent Zorbax C18 column (5 μ m, 4.6 x 150 mm), employing 0.1% TFA in water (RP-HPLC solvent A), and 90% acetonitrile, 0.1% TFA in water (RP-HPLC solvent B), as the mobile phases. Typical analytical gradients were 0-70% solvent B over 30 min at a flow rate of 1 ml/min. Preparative scale purifications were conducted on an Agilent 1260 preparative HPLC system. A Zorbax C18 preparative column (7 μ m, 21.2 x 250 mm) or a semi-preparative column (5 μ m, 9.4 x 250 mm) was employed at a flow rate of 20 mL/min or 4 mL/min, respectively. ESI-MS analysis was conducted on a Shimadzu MS2020 single quadrupole instrument connected to a Nexera UHPLC system. Absorbance spectra were recorded with an Agilent 8453 UV-Vis spectrophotometer. SDS-PAGE, native PAGE and agarose gels were imaged using a ChemiDoc MP imaging system from BioRad. Titrations using microscale thermophoresis were done on a MonoLith NT.115 instrument equipped with blue/green or green/red filters from NanoTemper technologies. Manual peptide synthesis and reactions on solid-phase were carried out in reaction vessels from Peptides International and automated peptide synthesis done on a Tribute instrument from Peptides International Inc. Live-cell confocal microscopy was done on a LSM700 inverted microscope from Zeiss. For single-molecule TIRF microscopy a Nikon Ti-E inverted fluorescence microscope, controlled by NIS-elements, equipped with a CFI Apo TIRF 100x Oil immersion objective (NA 1.49) was used. Scanning force microscopy was performed with a Bruker FastScan AFM and NCHV AFM cantilevers (Bruker). All components for the

microfluidics system (OB1 flow controller, MUX wire, tubings, valves, flow sensor) were purchased from Elveflow.

6.3. Chromatin reconstitution

Expression and purification of H2A, H2A.Z, H2B, H3C110A, H3C56A/C110A, H4 and H4K16C

100 mL precultures of BL21 (DE3) PlysS cells containing the plasmids for histone expression were grown overnight at 37°C, in LB medium supplemented with 100 µg/ml ampicillin and 35 µg/ml chloramphenicol (50 µg/ml for kanamycin for H2A.Z). From these precultures, 30 ml were used to inoculate 6 x 1 liter of LB cultures containing the antibiotics. The flasks were incubated at 37°C, until the OD₆₀₀ reached 0.6. At this point histone expression was induced with 0.4 mM IPTG for 2-3 h, 37°C, 200 rpm. The cultures were then transferred to tubes and centrifuged 10 min at 6000 rpm, 4°C. The pellets were resuspended in a total of 80 mL lysis/wash buffer (20 mM Tris-HCl pH 7.5, 200 mM NaCl, 1 mM EDTA, 1 mM PMSF, 1 mM β-mercaptoethanol, 1 protease inhibitor tablet/50 mL) and transferred to 4x 50 ml falcon tubes. The tubes were flash frozen and kept at -80°C until the next step.

For purification of the histones, the cell lysates were thawed and fresh BME and PMSF were added, followed by sonication (20 %, 10 s on and 30 s off, 3 min) and flash freezing. The lysate was thawed again, sonicated in the same way and centrifuged at 15'000 g, 4°C. The supernatant was disposed of and the pellets were washed with lysis/wash buffer supplemented with 1 % Triton X-100 by resuspending, sonicating and centrifuging. The wash step was done twice and then once without Triton X-100. 10 ml unfolding buffer (7 M Guanidine Hydrochloride, 20 mM Tris-HCl pH 7.5, 10 mM DTT) was added to each pellet, mixed 2 hours at 4°C and centrifuged at 15'000 g, 10 min, 4°C. The supernatant was dialysed overnight against low salt buffer (6 M urea, 10 mM Tris-HCl pH 7.5, 100 mM NaCl, 1 mM EDTA, 1 mM DTT, 0.2 mM PMSF) and loaded onto a HiTrap SP HP, 5 ml column. The protein was purified by increasing the buffer salt concentration to 1 M NaCl. 1.5 ml fractions were collected in a 96 well plate and analysed by SDS-PAGE. Fractions containing the protein were pooled and dialysed against 1 % acetic acid and finally lyophilized. The proteins were further purified by preparative RP-HPLC, collected fractions were characterized by analytical RP-HPLC and ESI-MS. Pure fractions were pooled, lyophilized and kept at -20°C for further use.

Synthesis of H3K_s56ac and H4K_s16ac by cysteine chemistry

Site-specific installation of the acetyl-lysine analogs were done in the same way for H3K_s56ac and H4K_s16ac. The lyophilized cysteine histones were dissolved in 0.2 M acetate buffer, pH 4 to a final concentration of 1 mM, followed by the addition of 50 mM N-vinylacetamide, 5 mM VA-044 and 15 mM glutathione. The reactions were incubated at 45°C for 2 h. Once the product was confirmed by analytical RP-HPLC and ESI-MS, the proteins were purified by semipreparative RP-HPLC, lyophilized and kept at -20°C for further use. A final characterization of the modified histones was done by analytical RP-HPLC and ESI-MS.

Synthesis of H3K9me3

The modified histone peptide H3(1–14)K9me3-NH₂ (carrying a C-terminal hydrazide) was synthesized by Sinan Kilic using solid phase peptide synthesis (SPPS). The truncated protein H3(Δ1–14)A15C, provided by Carolin Lechner was recombinantly expressed as N-terminal fusion to small ubiquitin like modifier (SUMO), the N-terminal SUMO was cleaved by SUMO protease and the protein purified by RP-HPLC. For ligation, in a typical reaction 3 μmol H3(1–14)K9me3-NH₂ was dissolved in ligation buffer (200 mM phosphate pH 3, 6 M GdmCl) at -10°C. NaNO₂ was added dropwise to a final concentration of 15 mM and incubated at -20°C for 20 min. H3(Δ1–14)A15C was dissolved in mercaptophenyl acetic acid (MPAA) ligation buffer (200 mM phosphate pH 8, 6 M GdmCl, 300 mM MPAA) and added to the peptide, followed by adjustment of the pH to 7.5. The ligation was left to proceed until completion (as observed by RP-HPLC). The product (H3K9me3A15C) was purified by semi-preparative RP-HPLC. For desulfurization, H3K9me3A15C was dissolved in tris(2-carboxyethyl)phosphine (TCEP) desulfurization buffer (200 mM phosphate pH 6.5, 6 M GdmCl, 250 mM TCEP). Glutathione (40 mM) and a radical initiator, VA-044 (20 mM), were added, followed by a readjustment of the pH to 6.5. The reaction mixture was incubated at 42°C until completion (verified by RP-HPLC and ESI-MS). The final product, H3K9me3, was purified by semi-preparative RP-HPLC, lyophilized and kept at -20°C for further use. A final characterization of the modified histones was done by analytical RP-HPLC and ESI-MS.

Expression and purification of histone H1.1

100 ml precultures were grown overnight at 37°C, 200 rpm in LB medium supplemented with 100 μg/ml ampicillin and 35 μg/ml chloramphenicol. From these precultures, 30 ml were used to inoculate 2 x 1 liters of LB cultures containing antibiotics. The flasks were incubated at 37°C

shaking at 200 rpm until the OD₆₀₀ reached 0.6. At this point human histone H1.1 expression was induced with 0.5 mM IPTG for 3 h 30 min. The cultures were then transferred to tubes and centrifuged 15 min at 4000 rpm, 4°C. The pellets were resuspended in a total of 40 ml lysis buffer (50 mM Tris-HCl pH 8, 200 mM NaCl, 1 mM EDTA, 2%, 1 mM PMSF, 1 mM BME, 1 protease inhibitor tablet/50 ml) and transferred to 2 x 50 ml falcon tubes. The tubes were flash frozen and kept at -80°C until the next step. For purification of histone H1.1, the cell lysate was thawed and sonicated (30 %, 15 s on and 45 s off, 3 min) and then centrifuged at 15'000 g, 20 min, 4°C. The supernatant was collected and loaded onto a HiTrap SP HP, 5 ml column for cation exchange. The buffer salt concentration was increased to 1 M NaCl to elute the protein. 1.5 ml fractions were collected in a 96 well plate and analysed by SDS-PAGE. Fractions containing the protein were pooled, the buffer was exchanged to gel filtration buffer (50 mM sodium phosphate pH 7, 150 mM NaCl) using P10 columns and the protein was concentrated, followed by purification with size exclusion chromatography using a S75 10/300 GL column in gel filtration buffer. 1 ml fractions were collected in 96 well plate and analysed by SDS-PAGE. Collected fractions containing the protein were pooled, concentrated, mixed with glycerol (to 10%), flash frozen, aliquoted and stored at -80°C. A final characterization of H1.1 was done by analytical RP-HPLC and ESI-MS.

Expression, purification and labeling of Histone H1.1

For fluorescent labeling, a cysteine residue was added to the C-terminus of H1.1 by site-directed mutagenesis, using the Quikchange II XL site-directed mutagenesis kit. The protein was expressed in the same way as for H1.1. After cation exchange and buffer exchange, the protein was labeled with Atto532-iodoacetamide overnight at 4°C. The reaction was quenched with TCEP and purification was achieved by size exclusion chromatography with the S75 10/300 GL column. The purified protein was mixed with glycerol (to 10 %), flash frozen and stored at -80°C. A final characterization of the labeled H1.1 was done by analytical RP-HPLC and ESI-MS.

DNA preparation

A large scale production of the plasmid containing 12x 601 NPS was prepared with DH5α cells. The plasmids contained the 12x 601 NPS with either 30 bp or 50 bp linker DNA with several EcoRV sites and a unique BsaI restriction site at the 3' end of the DNA piece of interest. 100 ml precultures were grown 5 hours, 37°C, 200 rpm in LB medium supplemented with 100 µg/ml ampicillin. From these precultures, 20 ml were used to inoculate 4x 1 liters of LB cultures

containing antibiotics. The flasks were incubated overnight at 37°C, 200 rpm. The cultures were centrifuged 10 min at 4'000 rpm and the supernatant was discarded. The pellets were dissolved in 80 ml Alkaline lysis buffer I (50 mM glucose, 25 mM TrisHCl pH 8, 10 mM EDTA) and homogenized using a syringe. 240 ml Alkaline lysis buffer II (0.2 N NaOH, 1 % SDS) was added and mixed. Neutralization was done by adding 240 ml alkaline lysis buffer III (4 M potassium acetate, 2 M acetic acid) and incubated 15 min at 4°C. The mix was centrifuged at 4'000 g, 15 min at 4°C and the supernatant was filtered with a miracloth. To this, 0.52 volumes of isopropanol was added, incubated 30 min at RT and centrifuged at 4'000 g, 20°C, 30 min. The supernatant was discarded and the pellet dissolved in 20 ml TE buffer (10 mM Tris, 50 mM EDTA). 100 units of RNase A were added and incubated 2 hours at 37°C. KCl was added to obtain a 2 M KCl concentration, followed by plasmid purification with size exclusion chromatography on a sepharose 6 XK 50/30 column. 12 ml fractions were collected and analysed by agarose gel electrophoresis. Fractions containing the plasmid were pooled, isopropanol precipitated with 0.52 Volumes of isopropanol, centrifuged and the pellet redissolved in TE buffer. The plasmids were then subjected to an EcoRV restriction digest to release the DNA pieces of interest. The 12× 601 sequences were purified by polyethylene glycol (PEG) precipitation and dephosphorylated with Antarctic Phosphatase to prevent self-ligation. BsaI digest was then done to provide an overhang to ligate the DNA pieces to the anchor. The anchor was prepared in the following way: an oligonucleotide (5'-ph-CAGCTAGTCTGCT-(amine-linker)-CAGATATCGTCG-3'-Biotin) was labeled using 10 eq. excess of Atto647N-NHS ester in 0.1 M sodium tetraborate, pH 8.5 overnight at 4°C. The labeled oligonucleotide was then EtOH purified to get rid of excess dye and annealed to its complementary DNA strand (5'-CGACGATATCTGAGCAGACTA-3') and ligated (5 eq. excess) to the 12× 601 array DNA with T4 DNA ligase for 1 h at room temperature. The excess dsDNA was removed by purification with QIAquick spin columns (Qiagen), and the final 12× 601 DNA was finally purified by ethanol precipitation.

DNA for mononucleosomes used in HP1 experiments was prepared in the same way, however the plasmid contained only one NPS.

Octamer reconstitution

Core histones H2A, H2B, H3 and H4 (or modified variants) were dissolved at 1 mg/ml in unfolding buffer (20 mM Tris-HCl pH 7.5, 6 M GdmCl) and combined in equimolar ratios (with a 10% excess of H2A and H2B). To refold the histones into octamers the mixture was dialyzed against refolding buffer (10 mM Tris-HCl pH 7.5, 2 M NaCl, 1 mM EDTA). The

refolded octamers were purified by size exclusion chromatography on a superdex S200 10/300 GL column in refolding buffer. 250 μ l fractions were collected in a 96 well plate. Fractions were analysed by SDS-PAGE, those containing octamers were pooled, concentrated to 20–60 μ M, supplemented with glycerol to 50% and stored at -20°C.

Chromatin reconstitution

Chromatin arrays or mononucleosomes were reconstituted at a concentration of around 1 μ M per mononucleosome (100 pmol). Array DNA (a177 or a197) or nucleosome DNA were mixed with 1 equivalent (per NPS) of histone octamer in reconstitution buffer (10 mM Tris pH 7.5, 10 mM KCl, 0.1 mM EDTA) containing 2 M NaCl. For chromatin arrays, 0.5 molar equivalents of MMTV buffer DNA was added to prevent oversaturation. In the case of reconstituted chromatin containing linker histone, 0.5, 1 or 1.5 equivalents H1.1 were also added to the DNA/octamer mixture. The reactions were gradually dialyzed from high salt buffer (10 mM Tris pH 7.5, 1.4 M KCl, 0.1 mM EDTA) to reconstitution buffer over 12 h with a two-channel peristaltic pump. After the dialysis the reconstituted chromatin arrays were analyzed by non-denaturing 5 % polyacrylamide gel electrophoresis (PAGE) in 0.5 x Tris-Borate-EDTA (TBE) running buffer or on a 0.6 % agarose gel following ScaI restriction digest.

6.4. Effector protein preparation

Expression and purification of HP1 α -hinge

6 lysine/arginine residues were mutated to alanine by site-directed mutagenesis, using the Quikchange II XL site-directed mutagenesis kit. 100 ml precultures were grown overnight at 37°C, 200 rpm in LB medium supplemented with 50 μ g/ml ampicillin. From these precultures, 20 ml were used to inoculate 2x 1 liters of LB cultures containing ampicillin. The flasks were incubated at 37°C shaking at 200 rpm until the OD₆₀₀ reached 0.8. At this point the cultures were incubated at 4°C for 15 min. For the induction of protein expression, 0.25 mM IPTG was added to the cultures, which were incubated overnight at 18°C, 200 rpm. The cultures were then transferred to tubes and centrifuged 20 min at 4'000 rpm, 4°C. The pellets were resuspended in a total of 30 ml lysis buffer (25 mM phosphate, 50 mM NaCl, 5 mM imidazole, protease inhibitor, pH 7.8-8), transferred to 2x 50 ml falcon tubes and the cell lysate was homogenized with a large needle. The tubes were flash frozen and kept at -80°C until the next step. The following protein purification steps were carried out from one cell lysate. Cells were sonicated at 30 % amplitude (15 s on, 45 s off, 10 times). The lysate was centrifuged at 15'000 g, 10 min

at 4°C. The supernatant was loaded onto the Ni-NTA beads pre-equilibrated with Ni-NTA wash buffer (25 mM phosphate, 50 mM NaCl, 20 mM imidazole, pH 7.8-8). The supernatant was incubated for 30 min at 4°C, the resin was drained, washed with 2x 5CV of Ni-NTA wash buffer and finally eluted with 3x 1.5CV Ni-NTA elution buffer (25 mM phosphate, 50 mM NaCl, 400 mM imidazole, pH 7.8-8). Samples of the supernatant, flow through, washes and elution were taken and analysed by SDS-PAGE. Elutions were pooled and purified by anion exchange on a 1 ml Hi Trap Q FF column pre-equilibrated with the AIEX start buffer (25 mM phosphate, 50 mM NaCl, pH 7.8-8). The sample was loaded with a 5 ml loop over 15 CV, then the column was washed over 3 CV, the salt concentration was then increased from 50 mM NaCl to 1 M NaCl over 20 CV and a final wash was done over 3 CV with high salt. 1 ml fractions were collected into a 96-well plate. Fractions were analysed by SDS-PAGE, those containing the protein were pooled. Thrombin was added to the protein solution and incubated at room temperature until the His Tag was cleaved off completely, which was verified by analytical RP-HPLC and ESI-MS. The protein solution was concentrated and purified by size exclusion chromatography with a S200 10/300 GL column pre-equilibrated with the gel filtration buffer (50 mM Tris, 150 mM NaCl, 1 mM DTT, pH 7.2). 250 µL fractions were collected into a 96-well plate. Fractions were analysed by SDS-PAGE, those containing the protein were pooled, concentrated, diluted to 30% glycerol, aliquoted, flash frozen and placed in the -80°C freezer.

Expression, purification and labeling of HP1 α , β and γ

A short tripeptide (Thz-G₂-C₃-CONH₂, Thz denotes thiazolidine) was synthesized by SPPS. 1 mg Atto532-iodoacetamide was used to label the tripeptide (5 eq. excess) in 200 mM phosphate pH 7.3, 5 M GdmCl. The reaction was followed by analytical-HPLC and MS, once the reaction was complete, it was quenched by addition of TCEP, purified by semi-preparative RP-HPLC, and lyophilized. Thiazolidine opening was achieved by treatment with 2 M methoxylamine at pH 5. The labeled tripeptide was finally purified by semipreparative RP-HPLC, lyophilized and kept at -20°C until further use.

For expression of the HP1 proteins, the genes for HP1 α , HP1 β and HP1 γ were fused to the *Npu*^N split-intein sequence at their C-termini, followed by a hexahistidine tag. HP1 α and HP1 β were expressed in *E. coli* BL21 DE3 cells, whereas HP1 γ was expressed in *E. coli* Rosetta DE3 cells. Expression was induced with 0.25 mM IPTG overnight at 18°C. Cells were harvested and lysed in lysis buffer (25 mM phosphate pH 7.8, 50 mM NaCl, 5 mM imidazole and 1x protease inhibitor/50 ml). The proteins were purified over Ni-affinity resin with wash buffer (25 mM phosphate pH 7.8, 50 mM NaCl, 20 mM imidazole) and elution buffer (25 mM phosphate

pH 7.8, 50 mM NaCl, 400 mM imidazole). Eluted fractions were pooled and loaded onto a 1 ml HiTrap Q FF column for anion exchange chromatography. A gradient was run from low (25 mM phosphate pH 7.8, 50 mM NaCl) to high salt buffer (25 mM phosphate pH 7.8, 1 M NaCl). 1 ml fractions were collected into a 96 well plate and analysed by SDS-PAGE. Those containing the protein were pooled and concentrated. A total of 500 µl of the expressed HP1-Npu^N fusion constructs at a concentration of 50–100 µM were each applied to a column of 125 µl SulfoLink resin slurry, containing an immobilized Npu^C peptide. After 5 min incubation, the column was drained, followed by washes with wash buffer (100 mM phosphate pH 7.2, 1 mM EDTA, 1 mM TCEP) containing high (500 mM NaCl), intermediate (300 mM NaCl) and low salt (150 mM NaCl). About 1 mM of tripeptide in labeling buffer (100 mM phosphate pH 7.8, 50 mM MPAA, 200 mM MESNA, 150 mM NaCl, 10 mM TCEP, 1 mM EDTA) was added to the column and incubated for 16 h at room temperature. The column was drained and the eluate was collected. The column was further washed using elution buffer (100 mM phosphate pH 7.2, 200 mM MESNA, 150 mM NaCl, 10 mM TCEP, 1 mM EDTA). Elution fractions were pooled and the protein was purified by size exclusion chromatography with a superdex S200 10/300 GL in gel filtration buffer (50 mM Tris pH 7.2, 150 mM NaCl, 1 mM DTT). Fractions containing purified labeled HP1 were pooled and concentrated, glycerol was added to 30 %, frozen aliquots were stored at -80°C. A final characterization of the purified and labeled HP1 proteins was done by analytical RP-HPLC and ESI-MS.

Phosphorylation of HP1α

2.5 µg of recombinant HP1α was mixed with 100 U of casein kinase II (CK2), 100 µM adenosine triphosphate (ATP) spiked with 10 µCi [γ -³²P]-ATP in kinase reaction buffer (20 mM Tris-HCl, 10 mM MgCl₂, 0.1 mM EDTA, 2 mM DTT, 0.01 % Brij35, pH 7.5) in a total volume of 20 µl. The reaction was incubated at 37°C, 3 h. To stop the reaction, 5 µl loading buffer was added and the reaction mixture was analyzed by 12 % SDS-PAGE followed by autoradiography detection. To determine the number of phosphorylation sites in each reaction, the gel was dried and the bands corresponding the protein were cut out and their radioactivity was measured by calibrated scintillation counting. For smTIRF measurements ATP was removed by dialysis.

Cas9/dCas9 labeling

In a first step CoA was labelled; 8 mM CoA was mixed with 16 mM Alexa568 maleimide in 100 mM sodium phosphate buffer, pH 7. The reaction was incubated at RT for 1 hour, purified

by semipreparative HPLC, lyophilized and kept at -20°C until further use. 5 μ M Cas9/dCas9 with a ybbR tag on the C-terminal was incubated at RT with 1 μ M Sfp phosphopantetheinyl transferase and 10 mM CoA-A568 in 10 mM MgCl₂ and 50 mM HEPES, pH 7.3. A sample after 2 hours was run on an SDS-PAGE gel alongside a sample taken before addition of Sfp. The protein was then purified by size exclusion chromatography on a superdex S200 10/300 column in 20 mM HEPES, pH 7.5, 250 mM KCl, 1 mM DTT. 250 μ l fractions were collected in a 96 well plate. Fractions were analysed by SDS-PAGE and those containing the labeled proteins were pooled, concentrated, aliquoted, flash frozen and kept in the -80°C freezer until further use.

6.5. In vitro assays

EMSA

Three different concentrations of each HP1 protein (0, 3.5 and 7 μ M) were incubated with 0.2 pmol of 193-bp DNA containing the 601 sequence and a Cy5 label in EMSA buffer (20 mM Tris-HCl, 50 mM NaCl, 1 mM DTT, 0.1 mg/ml BSA) in a total volume of 10 μ l. The reaction mixtures were incubated 15 min at 37°C and terminated by adding 3 μ l 25 % sucrose. The samples were then separated on a non-denaturing 5 % polyacrylamide gel in 0.5x TBE running buffer.

Microscale thermophoresis

Measurements were carried out on a MonoLith NT.115 (Nanotemper). H3K9me3(1–14) peptide was diluted into HEPES buffer (50 mM HEPES pH 7.5, 150 mM NaCl, 0.05 % Tween, 1 mM DTT) and serial dilutions were prepared from 1 to 100 μ M with a final volume of 10 μ l. 250 nM of labeled protein was then added to each peptide dilution to a final volume of 20 μ l. The mixtures were then centrifuged 1 min, 15'000 rpm and loaded onto premium-coated capillaries. A cap scan was performed at 20 % detection LED to check that each capillary contained the same protein concentration. Thermophoresis was measured at 40 or 60 % infrared heating-laser power. Data were normalized to the start and end point, averaged and fitted with a quadratic binding equation.

Cas9 cleavage assay

Cas9 and guide RNA were incubated 15 min at RT in cleavage buffer (20 mM Tris HCl, pH 7.5, 100 mM KCl, 5 mM MgCl₂, 5 % glycerol, 1 mM DTT). DNA was added to the reaction to the

following concentrations; 200 nM Cas9, 500 nM RNA and 10 nM DNA or nucleosomes. The reaction was incubated at 37°C. 10 µl samples were taken and quenched by adding 1 µl 0.5 M EDTA and placed in the -20°C freezer until all the samples were taken. Samples were thawed and 1 µl Proteinase K (20 mg/ml) was added to digest DNA-bound Cas9. Samples were incubated 20 min at RT. Samples were mixed with loading buffer (90 % formamide, 10 % glycerol) and resolved on a 12.5 % polyacrylamide 7 M urea gel.

6.6. Single molecule microscopy

Surface Passivation

Glass coverslips (40 × 24 mm) and microscopy slides (76 × 26 mm) containing four drilled holes on each side were cleaned by sonication in 10 % alconox, acetone and ethanol with washing in miliQ H₂O between each step. The slides/coverslips were incubated at least 1 h in a mixture of concentrated sulfuric acid to 30 % hydrogen peroxide (3:1). The coverslips and slides were thoroughly washed with miliQ H₂O, sonicated in acetone for 15 min and then submerged in acetone containing 2 % (3-aminopropyl)triethoxysilane (APTES) for silanization. The slides and coverslips were dried with a nitrogen flow and strips of double-sided tape were sandwiched between a coverslip and a slide to create four channels. Silanized coverslips were placed in a vacuumed container and kept at -20°C until further use.

Before a single molecule experiment, the glass coverslips were passivated with a solution of 100 mg/ml mPEG(5000)-succinimidyl carbonate containing 1 % biotin-mPEG-succinimidyl carbonate for 2-3 h.

Single molecule TIRFM experiment for HP1 binding measurements

Once passivated, the channels were washed with water and buffer T50 (10 mM Tris, 50 mM KCl). For chromatin immobilization, 0.2 mg/ml neutravidin solution was incubated for 5 min, followed by extensive washes with T50 buffer. Then, 500 pM chromatin arrays/nucleosomes in T50 buffer were injected into the neutravidin treated flow chamber for 5 min, followed by a wash with T50 and imaging buffer (50 mM HEPES, 130 mM KCl, 10 % glycerol, 2 mM 6-hydroxy-2,5,7,8-tetramethylchromane-2-carboxylic acid (Trolox), 0.005 % Tween-20, 3.2 % glucose, glucose oxidase/catalase enzymatic oxygen removal system). Chromatin coverage was observed with the TIRF microscope (Nikon Ti-E) by fluorescent emission in the far-red channel upon excitation by a 640 nm laser line. Dynamic experiments were initiated by influx of 1–5 nM Atto532-labeled HP1 in imaging buffer. All smTIRF experiments were performed at

room temperature (22°C). HP1 dynamics were observed with an EMCCD camera (Andor iXon) in the yellow/orange channel using a 530 nm laser line for excitation at 20 W/cm². Ten thousand frames at 20 Hz rate were acquired over a 25 × 50 μm area at a resolution of 160 nm/pixel. Every 200 frames, an image of the chromatin positions in the far-red channel was recorded for drift correction.

Data analysis for HP1 binding measurements

For each chromatin fiber, an individual trace was extracted using a custom-made semi-automated Matlab (Mathworks) script^{85,98}. This was carried out by doing a baseline correction and a drift correction from the chromatin images taken every 200 frames. A peak-finding algorithm (using the far-red images) was employed to detect individual chromatin array positions. Fluorescence intensity traces for each chromatin position were obtained by integrating over a circle of 2-pixel radius. Individual HP1 fluorescence peaks were included based on point-spread-function (PSF) and distance cut-offs. To ensure that only single-molecules are analyzed, peaks exhibiting step-wise bleaching kinetics were excluded from the analysis. Kinetics were extracted from fluorescence traces using a semi-automated thresholding algorithm. Cumulative histograms were constructed from dark and bright intervals and fitted to mono or bi-exponential functions.

Single molecule TIRFM experiment for multiplexing measurements

1) Decoder optimization measurements. Once passivated, the channels were washed with water and buffer T50 (10 mM Tris, 50 mM KCl). For DNA template immobilization, 0.2 mg/ml neutravidin solution was incubated for 5 min, followed by extensive washes with T50 buffer. Then, 100 pM template DNA in T50 buffer was injected into the neutravidin treated flow chamber for 5 min, followed by a wash with T50 and imaging buffer (10 mM Tris, pH 7.5, 1 M NaCl, 0.05 %Tween, 3.2 % glucose, 10 % glycerol, 5 mg/ml BSA, 1 mM Trolox, glucose oxidase/catalase enzymatic oxygen removal system). Chromatin coverage was observed with the TIRF microscope (Nikon Ti-E) by fluorescent emission in the far-red channel upon excitation by a 640 nm laser line. Dynamic experiments were initiated by influx of either 10 nM decoders labeled with Atto532 or 10 nM decoders labeled Alexa488 in imaging buffer. All smTIRF experiments were performed at room temperature (22°C). Hybridization dynamics were observed with an EMCCD camera (Andor iXon) in the green channel or yellow/orange channel using a 530 nm laser line or 488 nm laser line for excitation. Five thousand frames at 5 Hz rate were acquired over a 25 × 50 μm area at a resolution of 160 nm/pixel. Every

200 frames, an image of the chromatin positions in the far-red channel was recorded for drift correction.

Data analysis: For each DNA template, an individual trace was extracted using a custom-made semi-automated Matlab (Mathworks) script^{85,98}. This was carried out by a baseline correction and a drift correction from the DNA images taken every 200 frames. A peak-finding algorithm (using the far-red images) was employed to detect individual template positions. Fluorescence intensity traces for each DNA position were obtained by integrating over a circle of 2-pixel radius. Individual decoder fluorescence peaks were included based on point-spread-function (PSF) and distance cut-offs. To ensure that only single-molecules are analysed, peaks exhibiting step-wise bleaching kinetics were excluded from the analysis. Kinetics were extracted from fluorescence traces using a semi-automated thresholding algorithm. Cumulative histograms were constructed from dark and bright intervals and fitted to mono exponential functions.

2) Two-layer decoding.

Once passivated, the channels were washed with water and buffer T50 (10 mM Tris, 50 mM KCl). For DNA template immobilization, 0.2 mg/ml neutravidin solution was incubated for 5 min, followed by extensive washes with T50 buffer. An automated injection was used to inject the samples into the channel. The automated microfluidic system is controlled with the Elveflow Smart Interface software. A nitrogen air flow from a tank is passed through plastic tubing (Pneumatic Tygon flexible tubing 7/32 OD 3/32 ID) and a particle/humidity filter to the OB1 Mk3 pressure controller with one output channel. The flow controller is coupled to a flow sensor, providing a feed-back loop to monitor the flow rate. The air flow is then split to the reservoirs containing the samples. The flow from the reservoirs are passed through (Tygon tubing 1/16''OD x 0.02'' ID) and is controlled by valves connected to the MUX wire (microfluidic valve controller). The tubes merge together at an 8-way splitter and the samples are passed through the flow sensor to a 3-way valve to either go to the microscopy slide or to the waste. 100 pM template DNA mixed with the USER enzyme in 1x Cutsmart buffer was injected into the neutravidin treated flow chamber and incubated for 10 min, followed by a wash with T50 and imaging buffer (10 mM Tris, pH 7.5, 1 M NaCl, 0.05 %Tween, 3.2 % glucose, 10 % glycerol, 5 mg/ml BSA, 1 mM Trolox, glucose oxidase/catalase enzymatic oxygen removal system). Chromatin coverage was observed with the TIRF microscope (Nikon Ti-E) by fluorescent emission in the far-red channel upon excitation by a 640 nm laser line. Dynamic experiments were initiated by influx 10 nM decoders labeled with Atto532 and/or 10 nM

decoders labeled Alexa488 in imaging buffer. All smTIRF experiments were performed at room temperature (22°C). Hybridization dynamics were observed with an EMCCD camera (Andor iXon) by switching every 200 ms between 530 nm laser line or 488 nm laser line for excitation. Decoding was imaged over 7'500 frames at 5 Hz rate over a $25 \times 50 \mu\text{m}$ area at a resolution of 160 nm/pixel. Every 500 frames, an image of the chromatin positions in the far-red channel was recorded for drift correction.

Data analysis: Movies for 488 nm and 532 nm were divided in ImageJ and analysed separately. For each DNA template, an individual trace was analysed using a custom-made semi-automated Matlab (Mathworks) script^{85,98}. This was carried out by a baseline correction and a drift correction from the DNA images taken every 250 frames. A peak-finding algorithm (using the far-red images) was employed to detect individual DNA template positions. Fluorescence intensity traces for each DNA position were obtained by integrating over a circle of 2-pixel radius. Individual templates were accepted or rejected depending on the point-spread function of the fluorescent binding events and the total intensity over the whole time trace.

6.7. Live cell and FRAP measurements

NIH 3T3 cell culture

NIH/3T3 mouse fibroblasts were cultured in 75 cm² tissue culture flasks in DMEM/F-12 supplemented with 10 % Newborn calf serum at 37°C in a water-saturated air and 5 % CO₂ atmosphere. Cells were transfected with three different plasmids; HP1 α -mEos3.2, mEos3.2-HP1 α (AAAA) or mEos3.2-HP1 α (hinge mutant). For transfection, cells were seeded onto 25 mm round coverslips in 6-well plates. At 70–90 % level of confluency the cells were transfected 4 h with 4 μg of plasmid DNA per well using Lipofectamine. The cells were imaged the following day.

Live cell measurement

Microscopy was performed using an inverted LSM 700 confocal microscope (Zeiss) and a plan-apochromat 63 x, 1.4 N.A. oil immersion objective. Cells were incubated with Hoechst staining, 5 min at 37°C. Hoechst stain was washed out and the cells were imaged in PBS. 405 nm and 488 nm excitation lasers were used to image Hoechst and mEos3.2 respectively. Images were acquired over 101.6 x 101.6 μm (2048 x 2048 pixels) with a 0.05 μm pixel size, 8-bit grey scale depth, line averaging of 4, pixel dwell time of 3.15 μs and the pinhole set to 1 Airy Units (AU).

Fluorescence recovery after photobleaching (FRAP) measurement

Microscopy was performed using the same microscope set up as for the live cell imaging. Fluorescence recovery after photobleaching (FRAP) bleaching and time-series images were acquired over 150×150 pixels with a pixel size of $0.1 \mu\text{m}$, 16-bit grayscale depth and a pixel dwell time of $1.58 \mu\text{s}$ with the pinhole set at $201 \mu\text{m}$. A circular spot of 14 pixels ($1.4 \mu\text{m}$) in diameter was used for bleaching. Five pre-bleach images were acquired before five iterations of a bleaching pulse at 100 % laser power used and movies were acquired for 42 s. Photobleaching during the time-series was corrected using the intensity in the bleach region relative to the entire acquisition region. The time-intensity acquisitions were normalized to the pre-bleach intensity and the first image after the bleach pulse. Results were averaged over 17–30 individual FRAP curves for unmodified HP1 α and mutant proteins.

6.8. Atomic Force microscopy

After reconstitution, chromatin fibers with or without H1.1 were dialyzed against 1 mM EDTA, pH 8 for 6 h. Nucleosomal arrays were then dialyzed against 1 mM EDTA, 0.1 % glutaraldehyde, pH 7.7 for 6 h and finally dialyzed overnight against 1 mM EDTA, pH 7.6. All dialysis steps were performed at 4°C . 2 μl of purified nucleosomal arrays was pipetted onto freshly cleaved mica and 5 μl water was added. The sample was left to settle for 5–10 min before the liquid was blown off with a nitrogen gas stream, leaving the dried chromatin arrays on the atomically flat mica. Atomic force microscope images were acquired in tapping mode in air with cantilevers at a nominal spring constant of 42 N/m and resonance frequency of 320 kHz. Typically, images were recorded at a resolution of 1024×512 pixel and at a line rate of 4 Hz. Data processing was done using standard SPM image processing software.

References

1. Kornberg, R. D. Structure of Chromatin. *Annu. Rev. Biochem.* **46**, 931–954 (1977).
2. Hewish, D. R. & Burgoyne, L. A. Chromatin sub-structure. The digestion of chromatin DNA at regularly spaced sites by a nuclear deoxyribonuclease. *Biochem. Biophys. Res. Commun.* **52**, 504–510 (1973).
3. Olins, A. L. & Olins, D. E. Spheroid Chromatin Units (v Bodies). *Science* **183**, 330–332 (1974).
4. Woodcock, C. L., Safer, J. P. & Stanchfield, J. E. Structural repeating units in chromatin. I. Evidence for their general occurrence. *Exp. Cell Res.* **97**, 101–110 (1976).
5. Luger, K., Mäder, A. W., Richmond, R. K., Sargent, D. F. & Richmond, T. J. Crystal structure of the nucleosome core particle at 2.8 Å resolution. *Nature* **389**, 10 (1997).
6. Chua, E. Y. D., Vasudevan, D., Davey, G. E., Wu, B. & Davey, C. A. The mechanics behind DNA sequence-dependent properties of the nucleosome. *Nucleic Acids Res.* **40**, 6338–6352 (2012).
7. McGinty, R. K. & Tan, S. Nucleosome Structure and Function. *Chem. Rev.* **115**, 2255–2273 (2015).
8. Arents, G., Burlingame, R. W., Wang, B. C., Love, W. E. & Moudrianakis, E. N. The nucleosomal core histone octamer at 3.1 Å resolution: a tripartite protein assembly and a left-handed superhelix. *Proc. Natl. Acad. Sci.* **88**, 10148–10152 (1991).
9. Arents, G. & Moudrianakis, E. N. The histone fold: a ubiquitous architectural motif utilized in DNA compaction and protein dimerization. *Proc. Natl. Acad. Sci.* **92**, 11170–11174 (1995).
10. Henikoff, S. & Smith, M. M. Histone Variants and Epigenetics. *Cold Spring Harb. Perspect. Biol.* **7**, (2015).

References

11. Widom, J. A relationship between the helical twist of DNA and the ordered positioning of nucleosomes in all eukaryotic cells. *Proc. Natl. Acad. Sci.* **89**, 1095–1099 (1992).
12. Luger, K., Dechassa, M. L. & Tremethick, D. J. New insights into nucleosome and chromatin structure: an ordered state or a disordered affair? *Nat. Rev. Mol. Cell Biol.* **13**, 436–447 (2012).
13. Sinha, D. & Shogren-Knaak, M. A. Role of Direct Interactions between the Histone H4 Tail and the H2A Core in Long Range Nucleosome Contacts. *J. Biol. Chem.* **285**, 16572–16581 (2010).
14. Kan, P.-Y., Caterino, T. L. & Hayes, J. J. The H4 Tail Domain Participates in Intra- and Internucleosome Interactions with Protein and DNA during Folding and Oligomerization of Nucleosome Arrays. *Mol. Cell. Biol.* **29**, 538–546 (2009).
15. Hansen, J. C. Conformational Dynamics of the Chromatin Fiber in Solution: Determinants, Mechanisms, and Functions. *Annu. Rev. Biophys. Biomol. Struct.* **31**, 361–392 (2002).
16. Hansen, J. C., Ausio, J., Stanik, V. H. & Van Holde, K. E. Homogeneous reconstituted oligonucleosomes, evidence for salt-dependent folding in the absence of histone H1. *Biochemistry (Mosc.)* **28**, 9129–9136 (1989).
17. Robinson, P. J. J., Fairall, L., Huynh, V. A. T. & Rhodes, D. EM measurements define the dimensions of the ‘30-nm’ chromatin fiber: Evidence for a compact, interdigitated structure. *Proc. Natl. Acad. Sci.* **103**, 6506–6511 (2006).
18. Dorigo, B. Nucleosome Arrays Reveal the Two-Start Organization of the Chromatin Fiber. *Science* **306**, 1571–1573 (2004).
19. Schalch, T., Duda, S., Sargent, D. F. & Richmond, T. J. X-ray structure of a tetranucleosome and its implications for the chromatin fibre. *Nature* **436**, 138–141 (2005).

20. Song, F. *et al.* Cryo-EM Study of the Chromatin Fiber Reveals a Double Helix Twisted by Tetranucleosomal Units. *Science* **344**, 376–380 (2014).
21. Allan, J., Hartman, P. G., Crane-Robinson, C. & Aviles, F. X. The structure of histone H1 and its location in chromatin. *Nature* **288**, 675–679 (1980).
22. Grigoryev, S. A., Arya, G., Correll, S., Woodcock, C. L. & Schlick, T. Evidence for heteromorphic chromatin fibers from analysis of nucleosome interactions. *Proc. Natl. Acad. Sci.* **106**, 13317–13322 (2009).
23. Ou, H. D. *et al.* ChromEMT: Visualizing 3D chromatin structure and compaction in interphase and mitotic cells. *Science* **357**, eaag0025 (2017).
24. Kilic, S. *et al.* Single-molecule FRET reveals multiscale chromatin dynamics modulated by HP1 α . *Nat. Commun.* **9**, (2018).
25. Poirier, M. G., Oh, E., Tims, H. S. & Widom, J. Dynamics and function of compact nucleosome arrays. *Nat. Struct. Mol. Biol.* **16**, 938–944 (2009).
26. Bonev, B. & Cavalli, G. Organization and function of the 3D genome. *Nat. Rev. Genet.* **17**, 661–678 (2016).
27. Hnisz, D., Day, D. S. & Young, R. A. Insulated Neighborhoods: Structural and Functional Units of Mammalian Gene Control. *Cell* **167**, 1188–1200 (2016).
28. Barrington, C., Pezic, D. & Hadjur, S. Chromosome structure dynamics during the cell cycle: a structure to fit every phase. *EMBO J.* **36**, 2661–2663 (2017).
29. Nagano, T. *et al.* Cell-cycle dynamics of chromosomal organization at single-cell resolution. *Nature* **547**, 61–67 (2017).
30. Hnisz, D. *et al.* Activation of proto-oncogenes by disruption of chromosome neighborhoods. *Science* **351**, 1454–1458 (2016).
31. Kaiser, V. B. & Semple, C. A. When TADs go bad: chromatin structure and nuclear organisation in human disease. *F1000Research* **6**, 314 (2017).

32. Nadal, S., Raj, R., Mohammed, S. & Davis, B. G. Synthetic post-translational modification of histones. *Curr. Opin. Chem. Biol.* **45**, 35–47 (2018).
33. Strahl, B. D. & Allis, C. D. The language of covalent histone modifications. **403**, 5 (2000).
34. Huang, H., Lin, S., Garcia, B. A. & Zhao, Y. Quantitative Proteomic Analysis of Histone Modifications. *Chem. Rev.* **115**, 2376–2418 (2015).
35. Jenuwein, T. & Allis, C. D. Translating the Histone Code. *Science* **293**, 1074–1080 (2001).
36. Chi, P., Allis, C. D. & Wang, G. G. Covalent histone modifications — miswritten, misinterpreted and mis-erased in human cancers. *Nat. Rev. Cancer* **10**, 457–469 (2010).
37. Fierz, B. & Muir, T. W. Chromatin as an expansive canvas for chemical biology. *Nat. Chem. Biol.* **8**, 417–427 (2012).
38. Kouzarides, T. Chromatin Modifications and Their Function. *Cell* **128**, 693–705 (2007).
39. Ruthenburg, A. J., Li, H., Patel, D. J. & David Allis, C. Multivalent engagement of chromatin modifications by linked binding modules. *Nat. Rev. Mol. Cell Biol.* **8**, 983–994 (2007).
40. Shogren-Knaak, M. Histone H4-K16 Acetylation Controls Chromatin Structure and Protein Interactions. *Science* **311**, 844–847 (2006).
41. Neumann, H. *et al.* A Method for Genetically Installing Site-Specific Acetylation in Recombinant Histones Defines the Effects of H3 K56 Acetylation. *Mol. Cell* **36**, 153–163 (2009).
42. North, J. A. *et al.* Phosphorylation of histone H3(T118) alters nucleosome dynamics and remodeling. *Nucleic Acids Res.* **39**, 6465–6474 (2011).
43. Fierz, B. *et al.* Histone H2B ubiquitylation disrupts local and higher-order chromatin compaction. *Nat. Chem. Biol.* **7**, 113–119 (2011).

44. Kilic, S., Boichenko, I., Lechner, C. C. & Fierz, B. A bi-terminal protein ligation strategy to probe chromatin structure during DNA damage. *Chem. Sci.* **9**, 3704–3709 (2018).
45. Bowman, G. D. & Poirier, M. G. Post-Translational Modifications of Histones That Influence Nucleosome Dynamics. *Chem. Rev.* **115**, 2274–2295 (2015).
46. Taverna, S. D., Li, H., Ruthenburg, A. J., Allis, C. D. & Patel, D. J. How chromatin-binding modules interpret histone modifications: lessons from professional pocket pickers. *Nat. Struct. Mol. Biol.* **14**, 1025–1040 (2007).
47. Mammen, M., Choi, S.-K. & Whitesides, G. M. Polyvalent Interactions in Biological Systems: Implications for Design and Use of Multivalent Ligands and Inhibitors. *Angew. Chem. Int. Ed.* **37**, 2754–2794 (1998).
48. Jacobson, R. H., Ladurner, A. G., King, D. S. & Tjian, R. Structure and Function of a Human TAFII250 Double Bromodomain Module. *Science* **288**, 1422–1425 (2000).
49. Dhalluin, C. *et al.* Structure and ligand of a histone acetyltransferase bromodomain. **399**, 6 (1999).
50. Ruthenburg, A. J. *et al.* Recognition of a Mononucleosomal Histone Modification Pattern by BPTF via Multivalent Interactions. *Cell* **145**, 692–706 (2011).
51. Huisinga, K. L., Brower-Toland, B. & Elgin, S. C. R. The contradictory definitions of heterochromatin: transcription and silencing. *Chromosoma* **115**, 110–122 (2006).
52. Bernstein, B. E. *et al.* A Bivalent Chromatin Structure Marks Key Developmental Genes in Embryonic Stem Cells. *Cell* **125**, 315–326 (2006).
53. Canzio, D., Larson, A. & Narlikar, G. J. Mechanisms of functional promiscuity by HP1 proteins. *Trends Cell Biol.* **24**, 377–386 (2014).
54. Eissenberg, J. C. & Elgin, S. C. R. HP1a: a structural chromosomal protein regulating transcription. *Trends Genet.* **30**, 103–110 (2014).

55. Singh, P. B. *et al.* A sequence motif found in a *Drosophila* heterochromatin protein is conserved in animals and plants. *Nucleic Acids Res.* **19**, 789–794 (1991).
56. Maison, C. & Almouzni, G. HP1 and the dynamics of heterochromatin maintenance. *Nat. Rev. Mol. Cell Biol.* **5**, 296–305 (2004).
57. Nishibuchi, G. & Nakayama, J. -i. Biochemical and structural properties of heterochromatin protein 1: understanding its role in chromatin assembly. *J. Biochem. (Tokyo)* **156**, 11–20 (2014).
58. Minc, E., Courvalin, J.-C. & Buendia, B. HP1 γ associates with euchromatin and heterochromatin in mammalian nuclei and chromosomes. *Cytogenet. Genome Res.* **90**, 279–284 (2000).
59. Aucott, R. *et al.* HP1- β is required for development of the cerebral neocortex and neuromuscular junctions. *J. Cell Biol.* **183**, 597–606 (2008).
60. Brown, J. P. *et al.* RHesPea1rchy function is required for male germ cell survival and spermatogenesis. 9 (2010).
61. Bannister, A. J. *et al.* Selective recognition of methylated lysine 9 on histone H3 by the HP1 chromo domain. **410**, 5 (2001).
62. Lachner, M., O’Carroll, D., Rea, S., Mechtler, K. & Jenuwein, T. Methylation of histone H3 lysine 9 creates a binding site for HP1 proteins. *Nature* **410**, 116–120 (2001).
63. Nielsen, A. L., Oulad-Abdelghani, M., Ortiz, J. A., Remboutsika, E. & Chambon, P. Heterochromatin Formation in Mammalian Cells: Interaction between Histones and HP1 Proteins. 11 (2001).
64. Brasher, S. V. The structure of mouse HP1 suggests a unique mode of single peptide recognition by the shadow chromo domain dimer. *EMBO J.* **19**, 1587–1597 (2000).
65. Lechner, M. S., Schultz, D. C., Negorev, D., Maul, G. G. & Rauscher, F. J. The mammalian heterochromatin protein 1 binds diverse nuclear proteins through a common

- motif that targets the chromoshadow domain. *Biochem. Biophys. Res. Commun.* **331**, 929–937 (2005).
66. Thiru, A. *et al.* Structural basis of HP1/PXVXL motif peptide interactions and HP1 localisation to heterochromatin. *EMBO J.* **23**, 489–499 (2004).
 67. Canzio, D. *et al.* Chromodomain-Mediated Oligomerization of HP1 Suggests a Nucleosome-Bridging Mechanism for Heterochromatin Assembly. *Mol. Cell* **41**, 67–81 (2011).
 68. Hiragami-Hamada, K. *et al.* Dynamic and flexible H3K9me3 bridging via HP1 β dimerization establishes a plastic state of condensed chromatin. *Nat. Commun.* **7**, 11310 (2016).
 69. Azzaz, A. M. *et al.* Human Heterochromatin Protein 1 α Promotes Nucleosome Associations That Drive Chromatin Condensation. *J. Biol. Chem.* **289**, 6850–6861 (2014).
 70. Woodcock, C. L. & Ghosh, R. P. Chromatin Higher-order Structure and Dynamics. *Cold Spring Harb. Perspect. Biol.* **2**, a000596–a000596 (2010).
 71. Muchardt, C. *et al.* Coordinated methyl and RNA binding is required for heterochromatin localization of mammalian HP1. *EMBO Rep.* **3**, 975–981 (2002).
 72. LeRoy, G. *et al.* Heterochromatin Protein 1 Is Extensively Decorated with Histone Code-like Post-translational Modifications*□S. 11
 73. Maison, C. *et al.* SUMOylation promotes de novo targeting of HP1 α to pericentric heterochromatin. *Nat. Genet.* **43**, 220–227 (2011).
 74. Hiragami-Hamada, K. *et al.* N-Terminal Phosphorylation of HP1 Promotes Its Chromatin Binding. *Mol. Cell. Biol.* **31**, 1186–1200 (2011).

75. Lomberk, G., Bensi, D., Fernandez-Zapico, M. E. & Urrutia, R. Evidence for the existence of an HP1-mediated subcode within the histone code. *Nat. Cell Biol.* **8**, 407–415 (2006).
76. Cheutin, T. Maintenance of Stable Heterochromatin Domains by Dynamic HP1 Binding. *Science* **299**, 721–725 (2003).
77. Müller, K. P. *et al.* Multiscale Analysis of Dynamics and Interactions of Heterochromatin Protein 1 by Fluorescence Fluctuation Microscopy. *Biophys. J.* **97**, 2876–2885 (2009).
78. Festenstein, R. Modulation of Heterochromatin Protein 1 Dynamics in Primary Mammalian Cells. *Science* **299**, 719–721 (2003).
79. Fischle, W. *et al.* Regulation of HP1–chromatin binding by histone H3 methylation and phosphorylation. *Nature* **438**, 1116–1122 (2005).
80. Spicer, C. D. & Davis, B. G. Selective chemical protein modification. *Nat. Commun.* **5**, 4740 (2014).
81. Simon, M. D. *et al.* The Site-Specific Installation of Methyl-Lysine Analogs into Recombinant Histones. *Cell* **128**, 1003–1012 (2007).
82. Gloss, L. M. & Kirsch, J. F. Use of site-directed mutagenesis and alternative substrates to assign the prototropic groups important to catalysis by *Escherichia coli* aspartate aminotransferase. *Biochemistry (Mosc.)* **34**, 3999–4007 (1995).
83. Chatterjee, C., McGinty, R. K., Fierz, B. & Muir, T. W. Disulfide-directed histone ubiquitylation reveals plasticity in hDot1L activation. *Nat. Chem. Biol.* **6**, 267–269 (2010).
84. Li, F. *et al.* A Direct Method for Site-Specific Protein Acetylation. *Angew. Chem. Int. Ed.* **50**, 9611–9614 (2011).

References

85. Bryan, L. C. *et al.* Single-molecule kinetic analysis of HP1-chromatin binding reveals a dynamic network of histone modification and DNA interactions. *Nucleic Acids Res.* **45**, 10504–10517 (2017).
86. Wright, T. H. & Davis, B. G. Post-translational mutagenesis for installation of natural and unnatural amino acid side chains into recombinant proteins. *Nat. Protoc.* **12**, 2243–2250 (2017).
87. Wright, T. H. *et al.* Posttranslational mutagenesis: A chemical strategy for exploring protein side-chain diversity. *Science* **354**, aag1465–aag1465 (2016).
88. Lambalot, R. H. *et al.* A new enzyme superfamily — the phosphopantetheinyl transferases. *Chem. Biol.* **3**, 923–936 (1996).
89. Yin, J. *et al.* Genetically encoded short peptide tag for versatile protein labeling by Sfp phosphopantetheinyl transferase. *Proc. Natl. Acad. Sci.* **102**, 15815–15820 (2005).
90. Yin, J., Lin, A. J., Golan, D. E. & Walsh, C. T. Site-specific protein labeling by Sfp phosphopantetheinyl transferase. *Nat. Protoc.* **1**, 280–285 (2006).
91. Yin, J., Liu, F., Li, X. & Walsh, C. T. Labeling Proteins with Small Molecules by Site-Specific Posttranslational Modification. *J. Am. Chem. Soc.* **126**, 7754–7755 (2004).
92. Yin, J. *et al.* Single-Cell FRET Imaging of Transferrin Receptor Trafficking Dynamics by Sfp-Catalyzed, Site-Specific Protein Labeling. *Chem. Biol.* **12**, 999–1006 (2005).
93. Dawson, P. E. & Kent, S. B. H. Synthesis of Native Proteins by Chemical Ligation. *Annu. Rev. Biochem.* **69**, 923–960 (2000).
94. Merrifield, B. Solid phase synthesis. *Science* **232**, 341–347 (1986).
95. Amblard, M., Fehrentz, J.-A., Martinez, J. & Subra, G. Methods and protocols of modern solid phase peptide synthesis. *Mol. Biotechnol.* **33**, 16 (2006).
96. Dawson, P. E., Muir, T. W., Clark-Lewis, I. & Kent, S. B. Synthesis of proteins by native chemical ligation. *Science* **266**, 776–779 (1994).

97. Dawson, P. E., Churchill, M. J., Ghadiri, M. R. & Kent, S. B. H. Modulation of Reactivity in Native Chemical Ligation through the Use of Thiol Additives. *J. Am. Chem. Soc.* **119**, 4325–4329 (1997).
98. Kilic, S., Bachmann, A. L., Bryan, L. C. & Fierz, B. Multivalency governs HP1 α association dynamics with the silent chromatin state. *Nat. Commun.* **6**, (2015).
99. Mende, F. & Seitz, O. 9-Fluorenylmethoxycarbonyl-Based Solid-Phase Synthesis of Peptide α -Thioesters. *Angew. Chem. Int. Ed.* **50**, 1232–1240 (2011).
100. Fang, G.-M. *et al.* Protein Chemical Synthesis by Ligation of Peptide Hydrazides. *Angew. Chem. Int. Ed.* **50**, 7645–7649 (2011).
101. Wang, Z., Rejtar, T., Zhou, Z. S. & Karger, B. L. Desulfurization of Cysteine-Containing Peptides Resulting from Sample Preparation for Protein Characterization by MS. *Rapid Commun. Mass Spectrom. RCM* **24**, 267–275 (2010).
102. Wan, Q. & Danishefsky, S. J. Free-Radical-Based, Specific Desulfurization of Cysteine: A Powerful Advance in the Synthesis of Polypeptides and Glycopolypeptides. *Angew. Chem. Int. Ed.* **46**, 9248–9252
103. Muir, T. W., Sondhi, D. & Cole, P. A. Expressed protein ligation: A general method for protein engineering. *Proc. Natl. Acad. Sci. U. S. A.* **95**, 6705–6710 (1998).
104. Perler, F. B. Protein Splicing of Inteins and Hedgehog Autoproteolysis: Structure, Function, and Evolution. *Cell* **92**, 1–4 (1998).
105. Perler, F. Compilation and analysis of intein sequences. *Nucleic Acids Res.* **25**, 1087–1093 (1997).
106. Xu, M. Q. & Perler, F. B. The mechanism of protein splicing and its modulation by mutation. *EMBO J.* **15**, 5146–5153 (1996).
107. Shah, N. H. & Muir, T. W. Inteins: nature’s gift to protein chemists. *Chem Sci* **5**, 446–461 (2014).

108. Southworth, M. W. Control of protein splicing by intein fragment reassembly. *EMBO J.* **17**, 918–926 (1998).
109. Vila-Perelló, M. *et al.* Streamlined Expressed Protein Ligation Using Split Inteins. *J. Am. Chem. Soc.* **135**, 286–292 (2013).
110. Wals, K. & Ovaa, H. Unnatural amino acid incorporation in *E. coli*: current and future applications in the design of therapeutic proteins. *Front. Chem.* **2**, (2014).
111. Wang, L., Brock, A., Herberich, B. & Schultz, P. G. Expanding the Genetic Code of *Escherichia coli*. *Science* **292**, 498–500 (2001).
112. Zlatanova, J. & van Holde, K. Single-Molecule Biology: What Is It and How Does It Work? *Mol. Cell* **24**, 317–329 (2006).
113. ASHKIN, A. Optical trapping and manipulation of neutral particles using lasers. *Proc Natl Acad Sci USA* **8** (1997).
114. Ishikawa-Ankerhold, H. C., Ankerhold, R. & Drummen, G. P. C. Advanced Fluorescence Microscopy Techniques—FRAP, FLIP, FLAP, FRET and FLIM. *Molecules* **17**, 4047–4132 (2012).
115. Lichtman, J. W. & Conchello, J.-A. Fluorescence microscopy. *Nat. Methods* **2**, 910–919 (2005).
116. Berezin, M. Y. & Achilefu, S. Fluorescence Lifetime Measurements and Biological Imaging. *Chem. Rev.* **110**, 2641–2684 (2010).
117. Trache, A. & Meininger, G. A. Total Internal Reflection Fluorescence (TIRF) Microscopy. *Curr. Protoc. Microbiol.* **10**, 2A.2.1-2A.2.22 (2017).
118. Zheng, Q. *et al.* Ultra-stable organic fluorophores for single-molecule research. *Chem Soc Rev* **43**, 1044–1056 (2014).

119. Aitken, C. E., Marshall, R. A. & Puglisi, J. D. An Oxygen Scavenging System for Improvement of Dye Stability in Single-Molecule Fluorescence Experiments. *Biophys. J.* **94**, 1826–1835 (2008).
120. Cordes, T., Vogelsang, J. & Tinnefeld, P. On the Mechanism of Trolox as Antiblinking and Antibleaching Reagent. *J. Am. Chem. Soc.* **131**, 5018–5019 (2009).
121. Shimomura, O., Johnson, F. H. & Saiga, Y. Extraction, Purification and Properties of Aequorin, a Bioluminescent Protein from the Luminous Hydromedusan, Aequorea. Available at: <https://onlinelibrary.wiley.com/doi/pdf/10.1002/jcp.1030590302>. (Accessed: 26th April 2018)
122. Prasher, D. C., Eckenrode, V. K., Ward, W. W., Prendergast, F. G. & Cormier, M. J. Primary structure of the Aequorea victoria green-fluorescent protein. *Gene* **111**, 229–233 (1992).
123. Mollwitz, B. *et al.* Directed Evolution of the Suicide Protein O^6 -Alkylguanine-DNA Alkyltransferase for Increased Reactivity Results in an Alkylated Protein with Exceptional Stability. *Biochemistry (Mosc.)* **51**, 986–994 (2012).
124. Stennett, E. M. S., Ciuba, M. A. & Levitus, M. Photophysical processes in single molecule organic fluorescent probes. *Chem Soc Rev* **43**, 1057–1075 (2014).
125. Paddock, S. W. Principles and Practices of Laser Scanning Confocal Microscopy. *Mol. Biotechnol.* **16**, 127–150 (2000).
126. Combs, C. A. Fluorescence Microscopy: A Concise Guide to Current Imaging Methods. in *Current Protocols in Neuroscience* (eds. Crawley, J. N. *et al.*) (John Wiley & Sons, Inc., 2010). doi:10.1002/0471142301.ns0201s50
127. Martin-Fernandez, M. L., Tynan, C. J. & Webb, S. E. D. A ‘pocket guide’ to total internal reflection fluorescence. Available at: <https://onlinelibrary.wiley.com/doi/epdf/10.1111/jmi.12070>. (Accessed: 3rd May 2018)

128. Leake, M. C. *Single-Molecule Cellular Biophysics*. (Cambridge University Press, 2013).
doi:10.1017/CBO9780511794421
129. Lowary, P. . & Widom, J. New DNA sequence rules for high affinity binding to histone octamer and sequence-directed nucleosome positioning. *J. Mol. Biol.* **276**, 19–42 (1998).
130. Dorigo, B., Schalch, T., Bystricky, K. & Richmond, T. J. Chromatin Fiber Folding: Requirement for the Histone H4 N-terminal Tail. *J. Mol. Biol.* **327**, 85–96 (2003).
131. Schreiber, G., Haran, G. & Zhou, H.-X. Fundamental Aspects of Protein–Protein Association Kinetics. *Chem. Rev.* **109**, 839–860 (2009).
132. Canzio, D. *et al.* A conformational switch in HP1 releases auto-inhibition to drive heterochromatin assembly. *Nature* **496**, 377–381 (2013).
133. Ha, T. Single-Molecule Approaches Embrace Molecular Cohorts. *Cell* **154**, 723–726 (2013).
134. Sing, C. E., Olvera de la Cruz, M. & Marko, J. F. Multiple-binding-site mechanism explains concentration-dependent unbinding rates of DNA-binding proteins. *Nucleic Acids Res.* **42**, 3783–3791 (2014).
135. Graham, J. S., Johnson, R. C. & Marko, J. F. Concentration-dependent exchange accelerates turnover of proteins bound to double-stranded DNA. *Nucleic Acids Res.* **39**, 2249–2259 (2011).
136. Loparo, J. J., Kulczyk, A. W., Richardson, C. C. & van Oijen, A. M. Simultaneous single-molecule measurements of phage T7 replisome composition and function reveal the mechanism of polymerase exchange. *Proc. Natl. Acad. Sci.* **108**, 3584–3589 (2011).
137. Mendez, D. L. *et al.* The HP1a Disordered C Terminus and Chromo Shadow Domain Cooperate to Select Target Peptide Partners. *ChemBioChem* **12**, 1084–1096 (2011).

138. Kang, J. *et al.* Mitotic centromeric targeting of HP1 and its binding to Sgo1 are dispensable for sister-chromatid cohesion in human cells. *Mol. Biol. Cell* **22**, 1181–1190 (2011).
139. Yamagishi, Y., Sakuno, T., Shimura, M. & Watanabe, Y. Heterochromatin links to centromeric protection by recruiting shugoshin. *Nature* **455**, 251–255 (2008).
140. Zhu, P. & Li, G. Structural insights of nucleosome and the 30-nm chromatin fiber. *Curr. Opin. Struct. Biol.* **36**, 106–115 (2016).
141. Nishibuchi, G. *et al.* N-terminal phosphorylation of HP1 α increases its nucleosome-binding specificity. *Nucleic Acids Res.* **42**, 12498–12511 (2014).
142. Allahverdi, A. *et al.* The effects of histone H4 tail acetylations on cation-induced chromatin folding and self-association. *Nucleic Acids Res.* **39**, 1680–1691 (2011).
143. Routh, A., Sandin, S. & Rhodes, D. Nucleosome repeat length and linker histone stoichiometry determine chromatin fiber structure. *Proc. Natl. Acad. Sci.* **105**, 8872–8877 (2008).
144. Last, J. A., Russell, P., Nealey, P. F. & Murphy, C. J. The Applications of Atomic Force Microscopy to Vision Science. *Invest. Ophthalmol. Vis. Sci.* **51**, 6083–6094 (2010).
145. Vahabi, S., Nazemi Salman, B. & Javanmard, A. Atomic Force Microscopy Application in Biological Research: A Review Study. *Iran. J. Med. Sci.* **38**, 76–83 (2013).
146. Yue, H., Fang, H., Wei, S., Hayes, J. J. & Lee, T.-H. Single-Molecule Studies of the Linker Histone H1 Binding to DNA and the Nucleosome. *Biochemistry (Mosc.)* **55**, 2069–2077 (2016).
147. Mishima, Y. *et al.* Nucleosome compaction facilitates HP1 γ binding to methylated H3K9. *Nucleic Acids Res.* **43**, 10200–10212 (2015).

148. Woodcock, C. L., Skoultschi, A. I. & Fan, Y. Role of linker histone in chromatin structure and function: H1 stoichiometry and nucleosome repeat length. *Chromosome Res.* **14**, 17–25 (2006).
149. Stützer, A. *et al.* Modulations of DNA Contacts by Linker Histones and Post-translational Modifications Determine the Mobility and Modifiability of Nucleosomal H3 Tails. *Mol. Cell* **61**, 247–259 (2016).
150. Bednar, J. *et al.* Structure and Dynamics of a 197 bp Nucleosome in Complex with Linker Histone H1. *Mol. Cell* **66**, 384–397.e8 (2017).
151. Seidel, S. A. I. *et al.* Microscale thermophoresis quantifies biomolecular interactions under previously challenging conditions. *Methods* **59**, 301–315 (2013).
152. Shimojo, H. *et al.* Extended string-like binding of the phosphorylated HP1 α N-terminal tail to the lysine 9-methylated histone H3 tail. *Sci. Rep.* **6**, (2016).
153. Larson, A. G. *et al.* Liquid droplet formation by HP1 α suggests a role for phase separation in heterochromatin. *Nature* **547**, 236–240 (2017).
154. Strom, A. R. *et al.* Phase separation drives heterochromatin domain formation. *Nature* **547**, 241–245 (2017).
155. Deb, K., Pratap, A., Agarwal, S. & Meyarivan, T. A fast and elitist multiobjective genetic algorithm: NSGA-II. *IEEE Trans. Evol. Comput.* **6**, 182–197 (2002).
156. Sun, J., Garibaldi, J. M. & Hodgman, C. Parameter Estimation Using Metaheuristics in Systems Biology: A Comprehensive Review. *IEEE/ACM Trans. Comput. Biol. Bioinform.* **9**, 185–202 (2012).
157. Gillespie, D. T. Exact stochastic simulation of coupled chemical reactions. *J. Phys. Chem.* **81**, 2340–2361 (1977).
158. Pianosi, F., Sarrazin, F. & Wagener, T. A Matlab toolbox for Global Sensitivity Analysis. *Environ. Model. Softw.* **70**, 80–85 (2015).

159. Hergeth, S. P. & Schneider, R. The H1 linker histones: multifunctional proteins beyond the nucleosomal core particle. *EMBO Rep.* **16**, 1439–1453 (2015).
160. Meshorer, E. *et al.* Hyperdynamic Plasticity of Chromatin Proteins in Pluripotent Embryonic Stem Cells. *Dev. Cell* **10**, 105–116 (2006).
161. Wang, Y., Guo, L., Golding, I., Cox, E. C. & Ong, N. P. Quantitative Transcription Factor Binding Kinetics at the Single-Molecule Level. *Biophys. J.* **96**, 609–620 (2009).
162. Ayoub, N., Jeyasekharan, A. D., Bernal, J. A. & Venkitaraman, A. R. HP1- β mobilization promotes chromatin changes that initiate the DNA damage response. *Nature* **453**, 682–686 (2008).
163. Grzenda, A. *et al.* Functional impact of Aurora A-mediated phosphorylation of HP1 γ at serine 83 during cell cycle progression. *Epigenetics Chromatin* **6**, 21 (2013).
164. Minc, E., Allory, Y., Worman, H. J., Courvalin, J.-C. & Buendia, B. Localization and phosphorylation of HP1 proteins during the cell cycle in mammalian cells. *Chromosoma* **108**, 220–234 (1999).
165. Müller, M. M., Fierz, B., Bittova, L., Liszczak, G. & Muir, T. W. A two-state activation mechanism controls the histone methyltransferase Suv39h1. *Nat. Chem. Biol.* **12**, 188–193 (2016).
166. Francis, N. J. Chromatin Compaction by a Polycomb Group Protein Complex. *Science* **306**, 1574–1577 (2004).
167. Zhen, C. Y. *et al.* Live-cell single-molecule tracking reveals co-recognition of H3K27me3 and DNA targets polycomb Cbx7-PRC1 to chromatin. *eLife* **5**, e17667 (2016).
168. Son, J., Shen, S. S., Margueron, R. & Reinberg, D. Nucleosome-binding activities within JARID2 and EZH1 regulate the function of PRC2 on chromatin. *Genes Dev.* **27**, 2663–2677 (2013).

169. Choi, J. *et al.* DNA binding by PHF1 prolongs PRC2 residence time on chromatin and thereby promotes H3K27 methylation. *Nat. Struct. Mol. Biol.* **24**, 1039–1047 (2017).
170. Miller, T. C. R. *et al.* A bromodomain–DNA interaction facilitates acetylation-dependent bivalent nucleosome recognition by the BET protein BRDT. *Nat. Commun.* **7**, 13855 (2016).
171. Sharonov, A. & Hochstrasser, R. M. Wide-field subdiffraction imaging by accumulated binding of diffusing probes. *Proc. Natl. Acad. Sci. U. S. A.* **103**, 18911–18916 (2006).
172. Jungmann, R. *et al.* Single-Molecule Kinetics and Super-Resolution Microscopy by Fluorescence Imaging of Transient Binding on DNA Origami. *Nano Lett.* **10**, 4756–4761 (2010).
173. Florian, S. *et al.* Universal Super-Resolution Multiplexing by DNA Exchange. *Angew. Chem. Int. Ed.* **56**, 4052–4055 (2017).
174. Kropachev, K. Y., Zharkov, D. O. & Grollman, A. P. Catalytic Mechanism of *Escherichia coli* Endonuclease VIII: Roles of the Intercalation Loop and the Zinc Finger[†]. *Biochemistry (Mosc.)* **45**, 12039–12049 (2006).
175. Wiedenheft, B., Sternberg, S. H. & Doudna, J. A. RNA-guided genetic silencing systems in bacteria and archaea. *Nature* **482**, 331–338 (2012).
176. Doudna, J. A. & Charpentier, E. The new frontier of genome engineering with CRISPR-Cas9. *Science* **346**, 1258096–1258096 (2014).
177. Hinz, J. M., Laughery, M. F. & Wyrick, J. J. Nucleosomes Selectively Inhibit Cas9 Off-target Activity at a Site Located at the Nucleosome Edge. *J. Biol. Chem.* **291**, 24851–24856 (2016).
178. Horlbeck, M. A. *et al.* Nucleosomes impede Cas9 access to DNA in vivo and in vitro. *eLife* **5**, e12677 (2016).

179. Jinek, M. *et al.* A Programmable Dual-RNA-Guided DNA Endonuclease in Adaptive Bacterial Immunity. *Science* **337**, 816–821 (2012).
180. Sternberg, S. H., Redding, S., Jinek, M., Greene, E. C. & Doudna, J. A. DNA interrogation by the CRISPR RNA-guided endonuclease Cas9. *Nature* **507**, 62–67 (2014).
181. Davey, C. A., Sargent, D. F., Luger, K., Maeder, A. W. & Richmond, T. J. Solvent Mediated Interactions in the Structure of the Nucleosome Core Particle at 1.9Å Resolution. *J. Mol. Biol.* **319**, 1097–1113 (2002).
182. Bonisch, C. & Hake, S. B. Histone H2A variants in nucleosomes and chromatin: more or less stable? *Nucleic Acids Res.* **40**, 10719–10741 (2012).
183. Zilberman, D., Coleman-Derr, D., Ballinger, T. & Henikoff, S. Histone H2A.Z and DNA methylation are mutually antagonistic chromatin marks. *Nature* **456**, 125–129 (2008).
184. Anders, C. & Jinek, M. In vitro Enzymology of Cas9. *Methods Enzymol.* **546**, 1–20 (2014).

Curriculum Vitae

Louise Catherine Bryan

Address: Chemin des Pétoleyres 25, 1110 Morges, Switzerland
Phone number: +41 (0)78 742 89 48
E-mail: louise.bryan@alumni.epfl.ch
Date of birth: 15.05.1990
Nationality: British and French

EDUCATION

- 2014 - Present Doctoral assistant, LCBM, EPFL. Thesis supervisor: Prof. B. Fierz, EPFL
Deciphering the chromatin binding mechanisms of human HP1 variants at the single molecule level.
- 2012 - 2014 Master of Science in Molecular and Biological Chemistry, EPFL
Master thesis, LPPT, EPFL - *Sortase-mediated modification of phage-displayed peptides.*
Master project: LTP, EPFL - *Physicochemical characterization of nebulized superparamagnetic iron oxide nanoparticles.*
- 2008 - 2012 Bachelor of Science in Chemistry and Chemical Engineering, EPFL

PUBLICATIONS

- S. Kilic, S. Felekyan, O. Doroshenko, I. Boichenko, M. Dimura, H. Vardanyan, **L. C. Bryan**, G. Arya, C. Seidel, B. Fierz. Single-molecule FRET reveals multiscale chromatin dynamics modulated by HP1 α . Nat. Commun. (2018)
- L. C. Bryan**, et al. Single-molecule kinetic analysis of HP1-chromatin binding reveals a dynamic network of histone modification and DNA interactions. Nucleic acids research (2017)
- S. Kilic, A. Bachmann, **L. C. Bryan**, B. Fierz. Multivalency governs HP1 α association dynamics with the silent chromatin state. Nature communications (2015)
- H. Graczyk, **L. C. Bryan** et al. Physicochemical characterization of nebulized superparamagnetic iron oxide nanoparticles (SPIONs). Journal of aerosol medicine and pulmonary drug delivery (2015)